Advancing the Assessment of Muscle and Cerebral Hemodynamics using Near-InfraRed Spectroscopy

A dissertation submitted by

Cristianne Marie Fernandez

in partial fulfillment

of the requirements for the degree of

Doctor of Philosophy
in Biomedical Engineering

Tufts University

August 2023

Advisor:

Sergio Fantini, PhD

Committee Members:

Srivalleesha Mallidi, PhD

Robert Jacob, PhD

Darren Roblyer, PhD

Abstract

Non-invasive optical measurements of deep tissue (e.g., muscle, brain) have large applicability in the clinical setting. One overarching issue in Near-InfraRed Spectroscopy (NIRS) measurements are the contributions from baseline and dynamic optical properties of superficial tissue (skin, adipose layer, skull, scalp). In the case of skeletal muscle, the overlying adipose tissue affects measured NIRS signals and should be considered. Frequency-Domain (FD)-NIRS and a special multi-distance arrangement of sources and detectors in the Single-Distance (SD) and Dual-Slope (DS) configurations were used to study the effect of the optical properties in the two layers and their dynamics on recovered signals. Specifically, experimental data were taken during a Venous Occlusion (VO) and Arterial Occlusion (AO) on 4 subjects. Theoretical data were then generated using diffusion theory for a two-layered medium with set values of the reduced scattering coefficient (μ_s') and absorption coefficient (μ_a) of the two layers, and the thickness of the top layer. Experimental data were then compared to simulations and showed consistency with a top layer more scattering than the bottom layer and with absorption changes in the top layer that are comparable to those in the bottom layer for the VO, and less than those in the bottom layer for AO. Overall, this study shows the feasibility of discriminating baseline and dynamic optical properties of two-layered tissues using FD-NIRS data collected at multiple SDs and in DS configurations.

When studying the brain, NIRS signals are a mixture of scalp, skull, and brain hemodynamics which leads to a need for methods that preferentially measure the brain. Here, we apply FD and DS optical imaging during a Coherent Hemodynamics Spectroscopy (CHS)

protocol to demonstrate the preferential sensitivity to cerebral hemodynamics of DS and FD-NIRS measurements as compared to traditional Single-Distance Intensity (SDI) measurements. Specifically, the results show that DS phase measurements recorded hemodynamics that are mostly associated with blood-flow oscillations (as expected in the brain), while SDI measurements recorded hemodynamics that are mostly associated with blood-volume oscillations (as expected in the scalp). The use of CHS and imaging has large clinical application and opens the door to mapping of cerebral Auto-Regulation (AR).

Mapping of AR parameters as discussed above can be done by inducing oscillations in Arterial Blood Pressure (ABP). However this is not always feasible, and as such, spontaneous oscillations in ABP were investigated in a large data set of 78 subjects. In the low-frequency range sensitive to cerebral AR (0.01 Hz to 0.1 Hz), oscillations in ABP at 0.1 Hz featured significant coherence for the longest time fraction ($\sim$10 % to 30 %). At this frequency, the amplitude ratio and phase difference between cerebral hemodynamics (namely Oxy and De-oxy hemoglobin) and ABP showed a greater variance across subjects than over cortical locations and no significant difference between driving tasks and baseline. Measuring low-frequency cerebral hemodynamics coherent with systemic ABP holds promise for the non-invasive assessment of cerebral perfusion and AR at the cerebral microvascular level. Lastly, CHS was applied in the NeuroCritical Care Unit (NCCU) to assess the cerebral AR of 3 patients, which showed the feasibility of this technique in a clinical setting.

Acknowledgments

I would first like to thank my advisor Sergio Fantini. I am grateful to have an advisor that was always available to speak to his students, makes time for weekly group meetings, and is always patient when I need help understanding a particular concept. Thank you for your detailed feedback on my writing and for pushing me to finish my work on skeletal muscle. I will forever be grateful for the skills I have learned from you. I would also like to thank Angelo Sassaroli, who has always been there to answer all of my questions, even if they may be simple. I appreciate your willingness to discuss any problems I am stuck on and for always helping me find the best way to tackle the problem. I will also always remember the so-called dad jokes that you come into the office to tell us.

The Diffuse Optical Imaging of Tissue (DOIT) lab has been my home for the past 5 years, and I have had the opportunity to work with outstanding graduate students. Giles Blaney has become one of my closest friends over the years. Thank you for your support and willingness to answer my numerous texts and phone calls concerning research questions at all hours of the day. Outside of the lab, you have helped me discover hiking, camping, and canoeing, which have become some of my favorite hobbies. Without you, I would not have the outdoor skills I have today. I will always treasure my memories with you fishing in a canoe while Skipper attempts to eat all the fishing lures, playing numerous board games, and all the adventures/vacations we have shared. Next, I thank Thao Pham for all your support and friendship over the years we have overlapped. To the new graduate students, Jodee Frias and Fatemeh Tavakoli, it has been a pleasure getting to know you, and I know

I have left my work in good hands. Jodee, thank you for always smiling in the office and, most importantly, for always allowing me to come and hang out with your cats.

I would like to thank my family for their unwavering support. To my parents, thank you for always supporting me in my quest to be a "forever student". You both have always helped me with anything that I need and I deeply appreciate it. To my older sister Jessica, thank you for constantly pushing me, being a role model of how to work hard, and letting me stay with you whenever I need to. To Robert, thank you for always supporting me and treating me like family. To Kevin, thank you for always being willing to listen to my practice talks (especially those from when I was in undergrad) and for all of the great memories we shared when you visited me. Lastly, I would like to thank my grandparents, the late Roberto and Norma Fernandez on my Dad's side and Salvador and the late June Miralles on my mom's side for always ensuring I was taken care of.

I owe a big thanks to all of the amazing friends I have made throughout my 5 years at Tufts. My cohort were some of the first friends I made in Boston, and I will forever be grateful for their friendship and support. Specifically, I would like to thank my roommate, member of my cohort, and close friend Nilay Vora for always being there to hear about my day in the lab (both the good and the bad), go on walks, take Skipper on adventures with me, and, especially, thank you for all the times we went to get Boba randomly. Sydney Conner, who is also in my cohort and has been my roommate, has always been willing to hear about my day; thank you for all the good memories. I would also like to thank my friends Skye Edwards and Marly Coe for your continual support and all of our insightful conversations across many topics. Clarita Palad-Rowell has been one of my closest non-Tufts friend, thank you for all of your support through the years and for letting me hangout with Mac. A very special thank you to Brooke, who has supported me to no end in the last few months. You are the kindest and sweetest person I know. Thank you for everything you do.

My undergrad experiences with research led me to pursue a graduate degree, and I would like to thank my advisor Dr. Godavarty. She always pushed me, supported me when

needed, and recommended that I apply to Sergio's lab. I learned many valuable skills while working under Dr. Godavarty and had the honor of writing a thesis about my work. I would also like to thank my roommate and lab member Rebecca Kwasinski who introduced me to Biomedical Engineering as a field and helped me get the opportunity to work in Dr. Godavarty's lab. Lastly, I would like to thank three of my closest friends from undergrad, Brianna Sanchez, Samantha Menendez, and Christopher Estrella, for their support and many long nights together studying that have helped me get to where I am today.

Lastly, I would like to thank my dog, Skipper, for always being there when I need "cuddles" and for forcing me to take breaks. The constant ringing of your bells to go outside or your high-pitched bark when you want a toy is always the perfect sign that I should stop working and take a break. You have helped me immensely for the last 3 years.

Contents

List of Figures

List of Tables

List of Acronyms and Symbols

$COH(\widetilde{D}, \widetilde{ABP})$ Coherence between the Deoxy-hemoglobin and Arterial blood pressure phasors. 62, 100

$COH(\widetilde{O}, \widetilde{ABP})$ Coherence between the Oxy-hemoglobin and Arterial blood pressure phasors. 62, 100

COH Coherence. 62, 64

I Intensity. xix, 5–8, 15, 17, 22–28, 30, 31, 34–36, 38–46, 48, 49, 51, 53, 57, 61, 63, 64, 75, 82, 98, 114, 115

L_{top} top layer thickness. 19

R Reflectance. 6, 22

ΔD Deoxy hemoglobin and myoglobin concentration change. 11, 38, 41, 47, 118

ΔD Deoxy-hemoglobin concentration change. xvi, 11, 41, 56, 62, 65, 71, 76, 82–85, 87, 91, 92, 99–101, 105, 111

ΔO Oxy hemoglobin and myoglobin concentration change. 11, 38, 41, 47, 118

ΔO Oxy-hemoglobin concentration change. xvi, 11, 41, 56, 62, 65, 71, 76, 82–87, 91, 93, 99–101, 111

ΔT Total hemoglobin and myoglobin concentration change. 118

ΔT Total-hemoglobin concentration change. 11, 41, 64, 117

λ optical wavelength. 5, 23, 26, 35, 57, 64

$\boldsymbol{\mathcal{S}}$ matrix of sensitivity to an absorption change. 63, 64, 116

$\mathcal{S}$ Sensitivity to an absorption change. xv, 6, 7, 9, 17, 26–28, 64

ω angular modulation frequency. 6, 14, 18, 19, 22, 24

ϕ phase. xix, xxii, 3, 5–8, 15, 17, 22–28, 30, 31, 34–36, 38–51, 53, 56, 57, 61–64, 93, 98, 114, 115

ρ source-detector distance. 5–8, 20, 22–25, 27, 28, 30, 35, 36, 43, 49, 51, 56, 59, 61, 100, 101

$\widetilde{D}/\widetilde{ABP}$ phasor ratio vector between Deoxy-hemoglobin and Arterial blood pressure. xvi, 62–64, 76, 85–92, 99–103

$\widetilde{D}/\widetilde{O}$ phasor ratio vector between Deoxy-hemoglobin and Oxy-hemoglobin. xvi, 14, 64, 66–75, 85, 87–92

$\widetilde{O}/\widetilde{ABP}$ phasor ratio vector between Oxy-hemoglobin and Arterial blood pressure. xvi, 62–64, 76, 85–92, 99–102

$\widetilde{T}/\widetilde{ABP}$ phasor ratio vector between Total-hemoglobin and Arterial blood pressure. xvi, 64, 66–75

$\widetilde{\mu_a}/\widetilde{ABP}$ phasor ratio vector between the absorption coefficient and Arterial blood pressure. 63, 64

$\widetilde{\mu_a}/\widetilde{ABP}$ phasor ratio vector between the absorption coefficient and Arterial blood pressure. 63

$\vec{r}$ position vector. 18, 19, 23–28

$\widetilde{ABP}$ Arterial blood pressure phasor. 62, 68, 85, 92, 99, 100, 103

$\widetilde{D}$ Deoxy-hemoglobin phasor. 14, 62, 66, 68–70, 85, 92, 99, 100, 103

$\widetilde{O}$ Oxy-hemoglobin phasor. 14, 62, 66, 68–70, 85, 92, 99, 100, 103

$\widetilde{R}$ complex Reflectance. 17–20, 22–24, 27, 34, 61, 115

$\widetilde{T}$ Total-hemoglobin phasor. 14, 68

$\widetilde{\Phi}$ complex fluence rate. 17, 18, 27

$\widetilde{\mu}_{eff}$ complex effective attenuation coefficient. 18, 19, 23, 61

f_{mod} modulation frequency. 57

f frequency. 62, 64, 99, 109, 111

n index of refraction. 21

t time. 62, 99

$\Delta\mu_a$ absorption coefficient change. xv, 17, 23–26, 34, 35, 37–53, 61, 114–116

ϵ extinction coefficient. xv, 26, 27, 38, 41

$\langle L \rangle_I$ generalized optical path-length for intensity. xix, 24, 27, 35, 36, 47, 49, 51

$\langle L \rangle_\phi$ generalized optical path-length for phase. xix, 24, 27, 35, 36, 47, 49, 51

$\langle L \rangle$ total optical path-length. xv, xix, 24, 25, 27, 28, 35, 36, 48–51, 115, 116

$\langle \ell \rangle$ partial optical path-length. 27, 28, 115

$\langle \widetilde{L} \rangle$ general complex total optical path-length. 23, 24, 26, 27

$\langle \widetilde{\ell} \rangle$ general complex partial optical path-length. 26, 27

μ_a absorption coefficient. iii, xv, 5, 8, 9, 17–23, 34–36, 38, 41–47, 50–52, 58, 61, 82, 98, 114–116

μ_s' reduced scattering coefficient. iii, xv, 5, 9, 17–23, 34–36, 41–52, 58, 61, 82, 98, 114–116

ABP Arterial Blood Pressure. iv, xv, xvi, 4, 13, 15, 16, 56–58, 61, 62, 65–67, 75, 79–87, 90–103, 105, 108–111

AO Arterial Occlusion. iii, xv, xvii, xix, 10, 11, 30–32, 34, 36–40, 43, 47–49, 52, 116–118

AR Auto-Regulation. iv, x, 12, 13, 16, 93, 94, 107, 108, 110, 111

ATT Adipose Tissue Thickness. 29, 31, 32, 36

AVM ArterioVenous Malformation. 97

BF Blood Flow. xi, 10, 12–14, 16, 30, 34, 38, 41, 47, 48, 52, 57, 66–69, 71, 73–76, 107, 114–118

BL Block. 90, 92

BV Blood Volume. 13, 14, 16, 57, 66, 68, 69, 71, 73–76, 118

CBF Cerebral Blood Flow. x, 1, 12, 13, 95, 96, 104, 111

CHS Coherent Hemodynamics Spectroscopy. iii, iv, x, 4, 13–16, 56, 57, 66, 74, 75, 77, 79, 91, 94, 95, 104, 108, 111

CPP Cerebral Perfusion Pressure. 12, 13, 97, 104

CSF Cerebral Spinal Fluid. 12

CW Continuous-Wave. 2–6, 17, 19, 22, 24, 29, 30, 50, 56, 81, 83, 87, 116

CWT Continuous Wavelet Transform. 62, 99

D Deoxy hemoglobin and myoglobin. 10, 38, 47

D Deoxy-hemoglobin. xv, 5, 10, 11, 13–15, 26, 27, 31, 93, 110

DOI Diffuse Optical Imaging. 3, 15, 16, 55–57, 77

DOIT Diffuse Optical Imaging of Tissue. v

DPF Differential Path-length Factor. 24, 35, 43, 48–50, 63, 82, 98, 115

DS Dual-Slope. iii, iv, xvi, 2, 4, 7–9, 15, 23, 25, 26, 28, 30–33, 35, 38, 39, 42, 45–47, 49, 53–57, 59–61, 63, 64, 66, 69, 76, 77, 93, 105, 107, 113–116

DSϕ Dual Slope phase. xv, xvi, 7, 9, 25, 28, 35, 37, 38, 40, 42, 43, 45–48, 65–76, 113

DSI Dual-Slope Intensity. xv, xvi, 7, 9, 25, 28, 35, 37, 38, 40, 42, 43, 45–48, 65–68, 70, 71, 73, 74, 118

DSF Differential Slope Factor. 25, 35, 36, 43, 48–50, 63, 98

F Female. 31, 97

FD Frequency-Domain. iii, iv, xv, 3–7, 13, 14, 17, 19, 22, 29–34, 47, 53, 56–58, 61, 96, 98, 103, 105, 107, 113, 115

fMRI functional Magnetic Resonance Imaging. 55, 112

fNIRS functional Near-InfraRed Spectroscopy. 55, 112, 113

ICP IntraCranial Pressure. 12, 13, 97, 104

IRB Institutional Review Board. 31, 59, 81, 96

IVH IntraVentricular Hemorrhage. 97

Iz *Inion*. 60

L Lipid. xv, 26, 27

LED Light-Emitting Diode. 81

LFO Low Frequency Oscillation. 79, 91

M Male. 31, 97

MAP Mean Arterial Pressure. 13, 97, 104

MD Multi-Distance. 22, 23, 98

MP Moore-Penrose inverse. 62–64

NCCU NeuroCritical Care Unit. iv, xvi, xix, 16, 95–97, 99–103, 105, 108, 109, 111

NIRS Near-InfraRed Spectroscopy. i, iii, iv, ix, xi, xv, 1, 2, 4–10, 12, 13, 15, 17, 19, 22, 29–34, 47, 48, 50, 52, 53, 57, 58, 61, 79–83, 87, 91–94, 96, 98, 102–105, 107, 108, 110, 112–117

Nz *Nasion*. 60

O Oxy hemoglobin and myoglobin. 10, 38, 47

O Oxy-hemoglobin. xv, 5, 10, 11, 13–15, 26, 27, 31, 93, 110

OC Oxygen Consumption. xi, 9–12, 30, 31, 34, 38, 41, 47, 48, 52, 107, 114–116

PD Photo-Diode. 81

SC Self-Calibrating. 22, 23, 26, 35, 56, 61, 116

SD Single-Distance. iii, xvi, 6–9, 15, 23–25, 27, 28, 30, 32, 33, 35, 38–40, 42, 45–47, 51, 53, 56, 57, 59, 61, 63, 64, 66, 73, 75, 77, 81, 84, 86, 88, 98, 114–116

SDϕ Single Distance phase. xv, xvi, 9, 24, 27, 30, 37, 38, 40, 48, 65–71, 73, 74, 76, 100–103

SDI Single-Distance Intensity. iv, xv, xvi, 6, 7, 9, 24, 27, 30, 37, 38, 40, 43, 48, 57, 65–76, 93, 100–103, 113

SS Single-Slope. 4, 7–9, 23, 25, 28, 30, 98

SSϕ Sinlge Slope phase. xv, 7, 9, 25, 28

SSI Single-Slope Intensity. xv, 7, 9, 25, 28, 100–103

T Total hemoglobin and myoglobin. 12, 38, 47

T Total-hemoglobin. 12

TCD Transcranial Doppler ultrasound. 57, 80, 96, 110

TD Time-Domain. 3, 5, 29, 48, 56, 107, 115

UHMW Ultra High Molecular Weight polyethylene. 59

VO Venous Occlusion. iii, xv, xvii, xix, 11, 12, 30–32, 34, 36–41, 43, 47, 48, 116–118

W Water. xv, 26, 27

Equipment, Materials, & Software

automatic cuff inflation system E-20 Rapid Cuff Inflation System, D.E. Hokanson, Inc [Bellevue, WA USA]. 32, 33, 97

beat-to-beat finger plethysmography system NIPD100D BIOPAC Systems [Goleta, CA USA]. 58, 81, 98, 99

digital manometer Series 626 Pressure Transmitter Dwyer Instruments Inc [Michigan City, IN USA]. 32, 33, 58, 97

Imagent ISS Imagent V2 [Champaign, IL USA]. 32, 33, 57

MATLAB MathWorks MATrix LABoratory [Natick, MA USA]. 62, 84

medium fidelity partial-cab driving simulator RTI [Ann Arbor, MI USA]. 81

NIRScout NIRx Medical Technology [Berlin, Germany]. 81

OxiplexTS ISS OxiplexTS [Champaign, IL USA]. 98

pneumatic arm cuff SC12D, D.E. Hokanson, Inc [Bellevue, WA USA]. 32, 33

ultrasound system SonoSite S-Nerve FUJIFILM SonoSite Inc [Bothell, WA USA]. 60

Chapter 1

Introduction

1.1 Motivation

The human body contains approximately 5 L of circulating blood [1]. Red blood cells transport oxygen from the lungs to the organs of the body to support metabolism. Peripheral vascular disease affects more than 200 million people worldwide [2] and approximately 10 % of the population in the United States [3]. Additionally, cerebral vascular diseases are the most common life-threatening neurological diseases in the United States, with stroke being the 5^{th} leading cause of death in the United States [4]. These statistics highlight the importance of monitoring both muscular (i.e., peripheral) and cerebral hemodynamics. Non-invasive, continuous monitoring of Cerebral Blood Flow (CBF) at the bedside can be extremely useful in preventing secondary brain injury [5]. Our goal has been to develop tools to better the assessment of both skeletal muscle and cerebral hemodynamics. Non-invasive monitoring utilizing our novel Near-InfraRed Spectroscopy (NIRS) techniques presented here can enhance clinical translatability and allow for the study of disease, injury, or physiology.

1.2 Overarching Themes

Over the past 30 years, NIRS has become an increasingly popular tool for assessing skeletal muscle and cerebral hemodynamics. There has been success in utilizing NIRS for dynamic measurements of brain activation during cognitive [6–8], motor [6, 9–11], and visual stimulus [6, 8, 12, 13] tasks, as well as metrics for the assessment of cerebral autoregulation [14–19]. The use of NIRS in skeletal muscle at rest [20–22] and during dynamic exercise [23–26] has also been applied for exercise physiology and clinical medicine. While there has been success in these applications there are still a number of open questions regarding the sensitivity of these measurements to deeper tissue (i.e., the brain and skeletal muscle) as well as their clinical feasibility and translation.

The effect of superficial tissue, such as the subcutaneous adipose tissue, skin, and skull, on the optical signal has continued to be an open question and critical challenge in the field. Numerous methods have been developed to limit the impact of superficial tissues. One such approach is the collection of data from short ($<$10 mm)and long ($>$20 mm) source-detector distances with the hypothesis that the short distance measures mainly contributions from superficial tissue. This approach has been used in conjunction with data processing methods such as adaptive filtering [27], Independent Component Analysis (ICA) [6], regression procedure [28], or least square algorithms [29]. Many of these methodologies have been targeted towards Continuous-Wave (CW) data and include measurements that are specifically sensitive to superficial hemodynamics [6, 27–29]. An alternative method that has been introduced to suppress sensitivity to superficial tissue is the Dual-Slope (DS) [30, 31], which uses relatively long source-detector distances ($\geq$ 25 mm). The hypothesis is that data collected at different long source-detector distances will feature comparable contributions from superficial tissue and different contributions from deeper tissue. Taking measurements at short distances can be intrinsically difficult due to a higher potential for light leakage and limited by instrumental dynamic range when paired with long distances, making longer source-detector distances more promising. This DS technique has been applied primarily to

Frequency-Domain (FD) data [30–32], and also has been proposed in Time-Domain (TD) [33]. There has been a recent push for utilizing FD [32] and TD [34] techniques to exploit the enhanced depth sensitivity of the phase (ϕ) of photon-density-waves and of the higher moments of the photon time-of-flight distribution, as well as their ability to provide absolute measurements of tissue optical properties.

Robust measurements of absolute optical properties at baseline can prove difficult due to instrumental limitations and the reliance on specific assumptions. Measurements of absolute hemoglobin concentrations and optical properties is possible with both TD and FD methods. CW methods have been developed to measure total hemoglobin and tissue saturation but must make assumptions about scattering [32, 35, 36] and cannot retrieve absolute optical properties. Measurements of absolute properties and hemoglobin concentrations are appealing as they allow for longitudinal studies, comparisons across subjects, and the determination of normative values across populations [32]. Measures of baseline optical properties is incredibly important in Diffuse Optical Imaging (DOI), which relies on these baseline properties for the sensitivity matrix utilized in image reconstruction. While absolute baseline measurements can be a valuable tool, research across the field has focused on dynamic changes, such as during brain activation [6, 27–29] or vascular occlusions [20, 37]. Calculation of relative dynamic changes rely on a critical assumptions of the baseline optical properties, which if not known are typically assumed. Assumption of baseline properties is typically done when utilizing CW measurements, as calculation of these parameters is not possible. These assumptions limit the accuracy of this technique, and highlights the importance of absolute baseline property quantification.

Non-invasive methods sensitive to muscle and brain have an extensive application clinically [38–40], but there has been several challenges with clinical translation. These challenges have included difficulty in protocol implementation from a healthy to diseased population, the reliability and robustness of measurements, and a lack of clinical instrumentation that allows for absolute quantification. Translation from a healthy to a diseased population comes

with various practical factors, including patient cooperation and patient comfort. Focusing on patient comfort, we have found difficulty in the comfort level of the optical probe, as well as problems with protocols involving physical perturbations of the subjects, such as cyclic thigh cuff protocols for inducing Arterial Blood Pressure (ABP) oscillations for Coherent Hemodynamics Spectroscopy (CHS) protocols [19, 31, 41, 42]. For this reason, this work explores the feasibility of using spontaneous oscillations in ABP and CHS, which may be more clinically applicable. Along with these practical factors, obtaining reliable and robust measurements that can be reproduced over various subjects is challenging. One factor is the use of CW methods due to its simple implementation having a significant cost benefit clinically [36]. On the other hand, the use of FD - NIRS has the possibility of achieving non-invasive optical measurements more sensitive to the brain and muscle along with the recovery of absolute optical properties and hemoglobin concentrations [32], increasing its robustness and reliability for clinical translation. The DS technique can be advantageous in increasing the robustness as it is largely insensitivity to instrumental drifts and optical coupling effects [31, 43].

This work aims to tackle this problem of superficial sensitivity by utilizing FD - NIRS with DS and Single-Slope (SS) configurations that feature a sensitivity selective to deeper tissue [30, 31, 44], as well as explore methods to increase clinical translatability. Measurements more representative of skeletal muscle and cerebral hemodynamics allow for a more explicit interpretation of their dynamics without the potential for information from superficial confounds to contaminate the results.

1.3 Near-InfraRed Spectroscopy (NIRS)

NIRS is a non-invasive optical method that utilizes wavelengths in the range of 600 nm to 1000 nm which can obtain local measurements of absorption and scattering properties in biological tissue [32, 34, 45]. NIRS systems have potential for substantial clinical transla-

tion due to their non-invasive nature, high sampling rate, and lightweight instrumentation [32, 40]. The ability to measure the absorption coefficient (μ_a) gives information on the chemical composition of the measured tissue, while the reduced scattering coefficient (μ_s') gives structural information. Typical values for the μ_a and μ_s' on the human head at an optical wavelength (λ) of 830 nm are 0.01 mm^{-1} and 0.66 mm^{-1}, respectively [46]. The μ_a at a minimum of 2 λs can be translated into Oxy-hemoglobin (O) and Deoxy-hemoglobin (D) concentrations which are physiologically relevant chromophores for various applications. Absolute O and D recovered from the same data above were approximately 30 µM and 22 µM, respectively, and can translated into a tissue oxygen saturation of 58 %. All of which are clinically relevant parameters that can be used to monitor cerebral health.

1.3.1 Measurement Methods

The temporal domains of NIRS are CW, FD, and TD. CW-NIRS has the simplest implementation since it utilizes unmodulated light that is injected into the tissue. Intensity (I) is then measured at some source-detector distance (ρ) away after the photons have traversed through the tissue. FD, on the other hand, uses sinusoidally modulated light on the order of 100 MHz to obtain measures of the amplitude (which we refer to as I) and the phase (ϕ) of the photon density waves after the photons have traversed through the tissue. Figure 1.1 shows an example of FD-NIRS applied to the human head and shows the decrease in I and shift in ϕ that is measured compared to the source I and ϕ. Lastly, TD-NIRS utilizes pulsed source light on the order of 10 ps in width and measures time-of-flight distribution after it has traveled through the tissue [34]. In FD [32] or TD [34] techniques, the ϕ or higher moments of the photon time-of-flight distribution, respectively, intrinsically provide measurements that are more specific to deeper tissue [31, 33, 47]. This work does not utilize the use of TD-NIRS but focuses on the use of FD (Chapter 3, Chapter 4, and Chapter 6) and CW (Chapter 5).

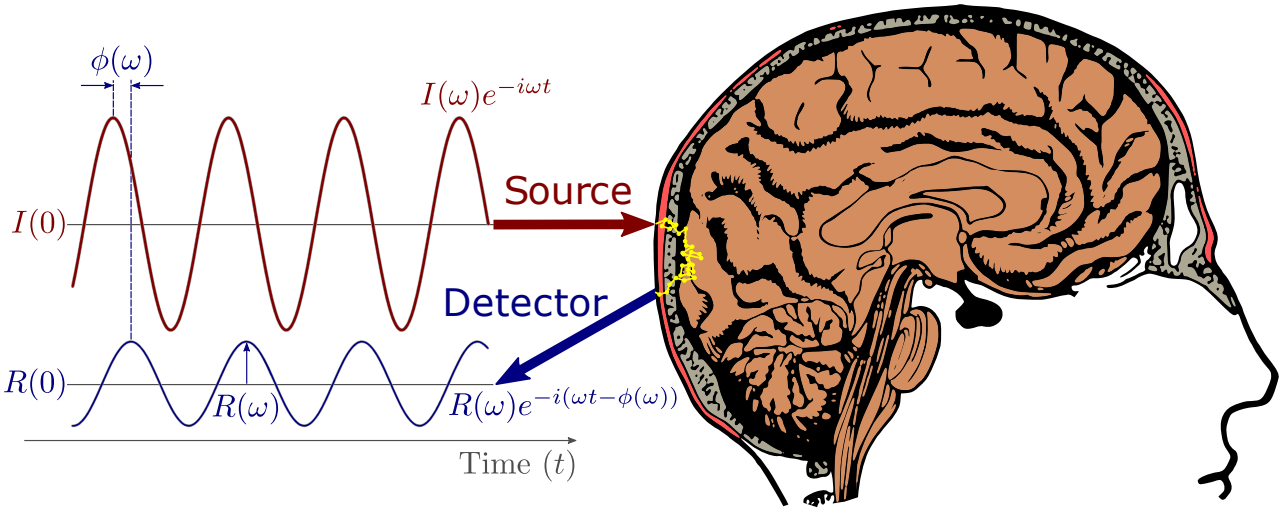

Figure 1.1: Example of Frequency-Domain (FD)-Near-InfraRed Spectroscopy (NIRS) applied to the human head. Sinusoidally modulated light is injected into the tissue via a source fiber. The light then traverses through the tissue to an optical detector. The optical detector measures the amplitude (which we refer to as $I(\omega)$) and the phase (ϕ) of the photon density waves after the photons have traversed through the tissue. The case of Continuous-Wave (CW)-NIRS is shown where un-modulated light ($I(0)$) is injected into the tissue and the reflectance ($R(0)$) is detected.

1.3.2 The Need for Selective Sensitivity to Deep Tissue

Measurements of both the brain and skeletal muscle are contaminated by signals from superficial tissue that are not of interest. In the case of the brain, the contamination is from the scalp and skull, while for skeletal muscle, it is the adipose tissue and skin. Considering these layers, it is important to use measurement methods preferentially sensitive to deep tissues. Advances have been made to develop preferentially sensitive methods to deeper hemodynamics and limit the effect of hemodynamics from superficial tissue [30, 48].

Currently, the most commonly used technique is Single-Distance (SD) measurements, which recovers the temporal changes in the optical data (I or ϕ in FD) between one optical source and one detector (typically 20 mm to 40 mm apart). Figure 1.2(a) shows the Sensitivity to an absorption change ($\mathcal{S}$) (as defined in section 2.4) for Single-Distance Intensity (SDI) where one can see the traditional banana shape [44, 49]. SDI measurements have the largest $\mathcal{S}$ to the surface as compared to measurements with ϕ (Figure 1.2(b)). Increasing ρ between

the source and detector increases $\mathcal{S}$ to deeper tissue, but is limited by noise especially when using ϕ measurements which are intrinsically have more noise. Methods such as including a short and long SDI measurements along with data processing methods such as independent component analysis [6], adaptive filtering [27], regression procedures [28], or a least-square algorithm [29] have been proposed to decouple superficial and deep hemodynamics. In this work we used ϕ information from FD or different source-detector arrangements to increase sensitivity to deeper layers [31].

Multiple SD measurements allow for measurements of the slope of optical data versus ρ. These methods are termed SSs and are based on the slopes of the linearized I ($\ln(\rho^2 I)$) or ϕ versus ρ. Figure 1.2(c-d) shows the $\mathcal{S}$ for Single-Slope Intensity (SSI) and Sinlge Slope phase (SSϕ) utilizing ρs of 25 mm and 35 mm. SSI and SSϕ have been shown to be weakly sensitive to superficial homogeneous layers [48] but have the drawback of a negative $\mathcal{S}$. A negative $\mathcal{S}$ indicates that the recovered change will be the opposite sign as the true change, while a positive $\mathcal{S}$ recovers a change with the same sign. This means that the negative superficial $\mathcal{S}$ of SSs would cause a positive local absorption change to be recovered as a negative change [31].

An improvement on the SS is the DS method which is the average of two symmetric SSs. The two SSs must follow a set of requirements to fulfill the DS, which are that the detector of the shorter SD in SS_1 must be the long of the SS_2, the difference between the two SDs in both SSs must be the same, and it must be made of two SSs [30]. Looking at the $\mathcal{S}$ in Figure 1.2, it is clear that the DS has a more localized $\mathcal{S}$ as compared to SD, and Dual Slope phase (DSϕ) has the deepest maximal $\mathcal{S}$ [31]. A more preferentially deep $\mathcal{S}$ for DS makes it advantageous in limiting the effect of superficial hemodynamics on NIRS measurements. While the $\mathcal{S}$ to deeper changes can be similar to Dual-Slope Intensity (DSI) (depending on the optical properties), DS is advantageous as it cancels out changes in optical coupling (described in subsection 2.3.3) and drifts.

Superficial tissues such as the skin, adipose tissue, and skull can not be avoided in non-

invasive measurements utilizing NIRS and must be considered. One advantage of the slope method is the insensitivity to absorption changes in a thin superficial layer. Increased absorption in a superficial layer (such as from melanin) would cause a decrease in the measured light I, affecting each SD measurement. This change in I at both SDs shifts the intercept term but not the slope of the linearized I versus ρ or the slope of ϕ versus ρ. Previous work has shown the insensitivity of slope methods to layers less than approximately 4 mm thick [48, 50], as the exact thickness will be dependent on the optical properties and ρs utilized. Work presented in Blaney *et al* (2021) [50] showed an effect of 10^{-6} mm^{-1} on the recovered μ_a when adding a 0.1 mm thick layer of melanin on the DS measurements with Monte Carlo simulations, while Franceschini *et al* (1998) [48] showed that the slope method was insensitive to layer thicknesses up to 4 mm utilizing two-layer phantoms with varying optical properties. These results show the relative insensitivity to a superficial thin layer, such as the superficial epidermis layer, for slope methods (SS and DS) for absolute measurements and measurements of dynamics changes, which is important in the case of varying skin pigmentation across subjects. This varying pigmentation would have no effect on SS and DS measurements while affecting SD, given that the superficial epidermis layer thickness of the forearm being on average 0.091 mm and on average 0.095 mm on the forehead [51].

1.4 Skeletal Muscle Hemodynamics

Skeletal muscle comprises 40 % of the total body weight on average [52] and receives 25 % of the cardiac output at rest [53, 54]. The main function of skeletal muscle is converting chemical energy into mechanical energy that allows for the generation of force and power, maintaining posture and producing movement [52]. The generation of energy to meet metabolic demands is fueled by oxygen, which is transported to active muscle fibers via a network of capillaries. Vascular inflow begins with primary arteries that run parallel to the muscle fiber direction, which divide into branching vessels that run perpendicular to the muscle fibers and eventually

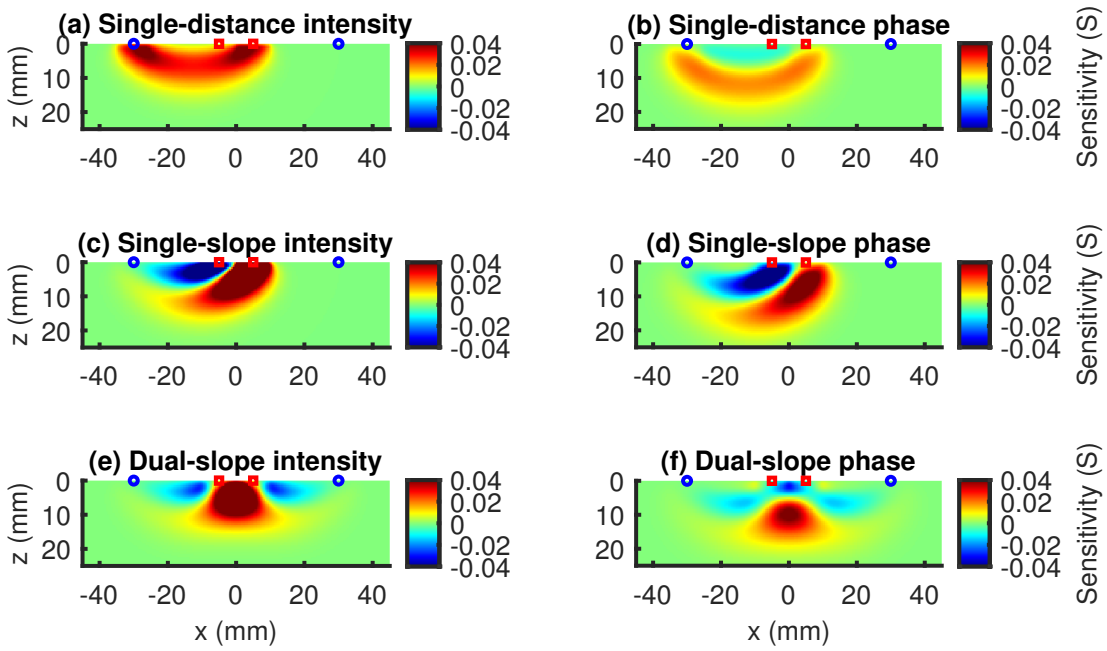

Figure 1.2: Maps of the Sensitivity to an absorption change ($\mathcal{S}$) for (a) Single-Distance Intensity (SDI), (b) Single Distance phase (SDϕ), (c) Single-Slope Intensity (SSI), (d) Sinlge Slope phase (SSϕ), (e) Dual-Slope Intensity (DSI) and (f) Dual Slope phase (DSϕ) for a reduced scattering coefficient (μ_s') of 1 mm^{-1} and absorption coefficient (μ_a) of 0.01 mm^{-1}. A source-detector separation of 35 mm was used for SD and the combination of 25 mm and 35 mm for SS and DS. For all presented maps, a perturbation size of 10 mm x 10 mm x 2 mm was used.

branch into a capillary system that runs parallel to fiber direction [53, 55]. Oxygen transport to muscles is facilitated by blood vessels through diffusion, where hemoglobin (Hb) is used to transport oxygen in the blood, and myoglobin (Mb) stores it within the muscle [55]. After delivering oxygen, blood is then transported through capillaries to post-capillaries venules to the veins.

Muscle has a low metabolic demand during the resting state, and thus Oxygen Consumption (OC) is low in the range of 0.1 mL 100g^{-1} min^{-1} with NIRS [22, 56] and a mean muscle OC $\sim$0.17 µmol 100mL^{-1} min^{-1} with blood sampling [57]. An increase in metabolic demand (such as exercise) causes an increase in skeletal muscle OC [55, 58] to upwards of 80 % from 25 % [59]. Measurements with NIRS during exercise have seen an increase in OC to around 0.6 mL 100g^{-1} min^{-1}. This increase is compensated for with increased tissue

microcirculation Blood Flow (BF) [59]. Baseline BF varies in range of $1\,\mathrm{mL}\,100\mathrm{mL}^{-1}\,\mathrm{min}^{-1}$ to $2\,\mathrm{mL}\,100\mathrm{mL}^{-1}\,\mathrm{min}^{-1}$ [20] with an increase to approximately $9\,\mathrm{mL}\,100\mathrm{mL}^{-1}\,\mathrm{min}^{-1}$ with exercise [21]. BF or OC measurements, along with the combination of the two, have been utilized to assess skeletal muscle health for diseases such as peripheral vascular disease [37, 60–63] and heart failure [64, 65], as well as in aging [66, 67] and during exercise [68].

Measurements of skeletal muscle hemodynamics with NIRS are a combination of the contributions from both Hb and Mb [69]. Mb has a similar spectral shape to that of hemoglobin ($\sim$4 nm redshift), but with a molar extinction coefficient $\sim$1/4 that of Hb due to 1 heme group per molecule compared to Hb, which has 4. The contribution of Mb to NIRS signals has been studied with a wide range of reported contributions ranging from less than 10 % [70] to upwards of 80 % [69, 71]. For this reason, when referring to O and D (both absolute baseline and dynamic) in skeletal muscle we consider them to be the sum of Hb and Mb. Dynamic changes due to vascular occlusions at rest are likely due to changes in Hb and not Mb [72], with the contributions from Mb being less than 20 % during exercise [68].

1.4.1 Measurements of Oxygen Consumption (OC) and Blood Flow (BF)

Measurement of skeletal muscle OC has been done invasively using blood sampling [24, 57, 73, 74], as well as non-invasively using phosphorus magnetic resonance spectroscopy [25] and NIRS [20, 22, 24]. A common measurement method for OC utilizes an Arterial Occlusion (AO), which involves inflating a pneumatic cuff to above systolic pressure ($\sim$ 200 mmHg), to block blood inflow and outflow from the arteries and veins. Due to the blocking of both arteries and veins, there is a constant blood volume within the limb, and all hemodynamic changes are due to oxygen consumption. Under these conditions, Oxy hemoglobin and myoglobin (O) decreases at the same rate as D increases due to the metabolic conversion of O to Deoxy hemoglobin and myoglobin (D) (shown in Figure 1.3(b)). The oxygen consumption

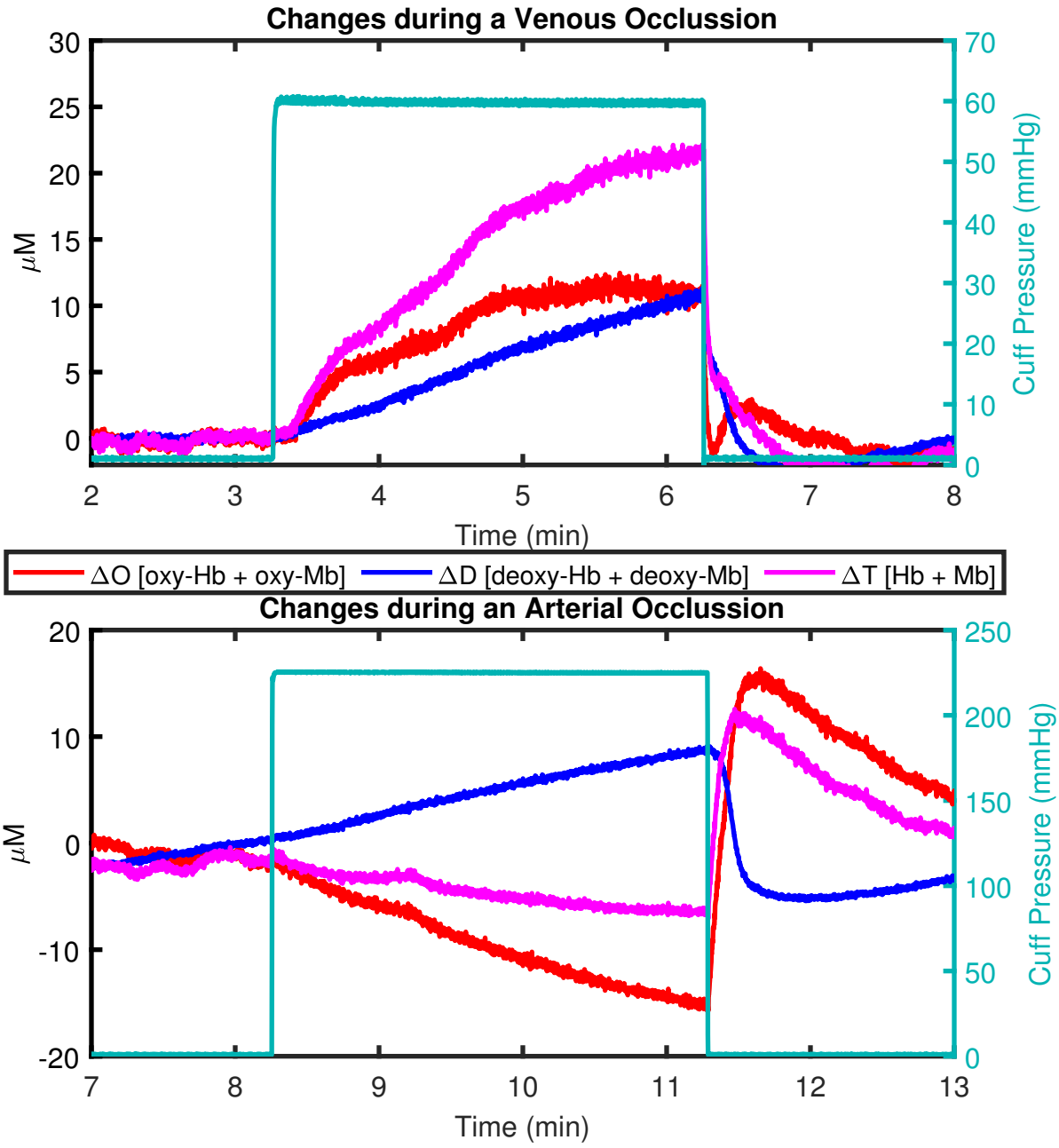

Figure 1.3: Example time trace of the Oxy hemoglobin and myoglobin concentration change (ΔO), Deoxy hemoglobin and myoglobin concentration change (ΔD), and ΔT (sum of ΔO and ΔD) during a (a) Venous Occlusion (VO) and an (b) Arterial Occlusion (AO) on the human calf. Hb refers to hemoglobin and Mb refers to myoglobin.

can then be calculated as

$$\mathrm{OC} = 4\frac{\mathrm{d}}{\mathrm{dt}}\left(\frac{D-O}{2}\right) \tag{1.1}$$

where 4 refers to the number of binding sites of oxygen on hemoglobin.

Non-invasive measurements of BF utilize a Venous Occlusion (VO) which involves inflation of a pneumatic cuff to ∼50 mmHg, to block venous outflow but allow arterial inflow to continue. After cuff inflation, the initial increase in total blood volume per time is proportional to the BF. This technique is commonly used in venous occlusion plethysmography [75], which measures the total blood volume change in the limb. BF utilizing Total-hemoglobin (T) as measured with NIRS can be calculated as

$$\mathrm{BF} = \frac{1}{\mathrm{ctHb}} \frac{\mathrm{d}}{\mathrm{dt}} (T) \tag{1.2}$$

where ctHb is the concentration of hemoglobin in blood. An example of the increase in Total hemoglobin and myoglobin (T) measured with NIRS is shown in Figure 1.3(a). BF has also been measured Doppler ultrasound [76], nuclear magnetic resonance imaging [77], and utilizing Xenon133 clearing rates [57].

1.5 Cerebral Hemodynamics

1.5.1 Cerebral Blood Flow (CBF) and Auto-Regulation (AR)

The brain uses 20 % of available oxygen for its functions such as the regulation of CBF and OC [78]. CBF is defined as the blood flow in the brain and is supplied b the internal carotid and vertebral arteries [78] which rise from the neck. A typical CBF is 50 mL/100 g min) [79].

The brain is enclosed in a rigid non-compressible skull, and as such, the total intracranial contents volume (blood, brain, and Cerebral Spinal Fluid (CSF)) should remain constant in the case of no injury [80, 81]. A volume increase in the intracranial contents causes an increase in IntraCranial Pressure (ICP) if cerebral compliance cannot account for the increase. A typical ICP reading in healthy human adults is less than 10 mmHg, and values outside this range can cause damage to the brain [80]. Changes in ICP affects the Cerebral

Perfusion Pressure (CPP) via the equation:

$$\text{CPP} = \text{MAP - ICP} \tag{1.3}$$

where Mean Arterial Pressure (MAP) is the average pressure through one cardiac cycle [82]. From Equation 1.3 it is noticeable that an increase in ICP decreases CPP given a constant change in MAP, which in turn will affects CBF [79].

Auto-Regulation (AR) is the ability of the brain to maintain a relatively constant CBF given changes in CPP. In the event of a brain injury, AR can become impaired, causing a larger risk of hypoperfusion or hyperperfusion. Static AR was defined by Lassen (1985) [83] as the ability of the brain to maintain a constant absolute CBF despite changes in the absolute MAP. Within the MAP range of 50 mmHg to 150 mmHg, CBF remains relativity constant at 50 mL/100 g min. Increases in MAP cause an increase in CBF, while a decrease in MAP causes a decrease in CBF. Dynamic AR is the response to rapid changes in MAP [79, 84] (such as with induced oscillations as in Chapter 4 and Chapter 6). A rapid drop in MAP (as in with a thigh cuff release) causes a drop in CBF that recovers before MAP in the case of a functioning AR [85–87]. When there is absent AR, MAP and CBF recover together. This analysis is also commonly done in the FD where CBF oscillations lead ABP oscillations [16, 88–90].

1.5.2 Coherent Hemodynamics Spectroscopy (CHS)

CHS is a method based on dynamic measurements of cerebral hemodynamics (O and D) that are coherent with a driving physiological process, for example, oscillations in ABP [91]. Implementation of CHS has been used during induced oscillations in ABP (Chapter 4 , Chapter 6) and spontaneous oscillations (Chapter 5) in this work, as well as several other publications by this group [19, 31, 41, 42, 91–94]. Measured NIRS cerebral hemodynamics are a combination of BF and Blood Volume (BV) oscillations (as well as oxygen

consumption) changes occurring in superficial tissue (i.e., scalp) and deep tissue (i.e., brain). These oscillations in O and D can be described in the FD as phasors (Oxy-hemoglobin phasor ($\widetilde{O}$) and Deoxy-hemoglobin phasor ($\widetilde{D}$)) at a frequency angular modulation frequency (ω). The relationship between the amplitude and phase difference of $\widetilde{O}$ and $\widetilde{D}$ can give insight into BF and BV oscillations.

The measured phasors of $\widetilde{O}$ and $\widetilde{D}$ can be broken down into the combinations of BF and BV by

$$\begin{aligned} \widetilde{O}_{BF} &= -\widetilde{D}_{BF} \\ \widetilde{T} = \widetilde{O} + \widetilde{D} &= \widetilde{O}_{BV} + \widetilde{D}_{BV} \\ \widetilde{O} &= \widetilde{O}_{BF} + \widetilde{O}_{BV} \\ \widetilde{D} &= \widetilde{D}_{BF} + \widetilde{D}_{BV} \end{aligned} \tag{1.4}$$

where the Total-hemoglobin phasor ($\widetilde{T}$) is used as a surrogate for BV. The phasor ratio vector between Deoxy-hemoglobin and Oxy-hemoglobin ($\widetilde{D}/\widetilde{O}$) represents the interplay between BV and BF oscillations as described by CHS [95]. When the vector has an angle of π rad and a magnitude of 1, the $\widetilde{D}$ and $\widetilde{O}$ are in opposition of phase and have the same amplitude; thus, the measured hemodynamics are dominated by BF. This relationship is shown above by $\widetilde{O}_{BF} = -\widetilde{D}_{BF}$. On the other hand, when $\widetilde{D}/\widetilde{O}$ has an angle of 0 rad, the phasors are in-phase, and the measured hemodynamics are dominated by BV, with the relative amplitude of $\widetilde{O}_{BV}$ and $\widetilde{D}_{BV}$ determined by tissue oxygen saturation in the volume-oscillating vascular compartment. These relationships are shown in Figure 1.4 where (a) shows a pure BF oscillation, (b) shows a pure BV oscillation, and (c) is the combination of the two. A saturation of 75 % was assumed for the oscillating compartment in Figure 1.4 and a frequency of 0.1 Hz.

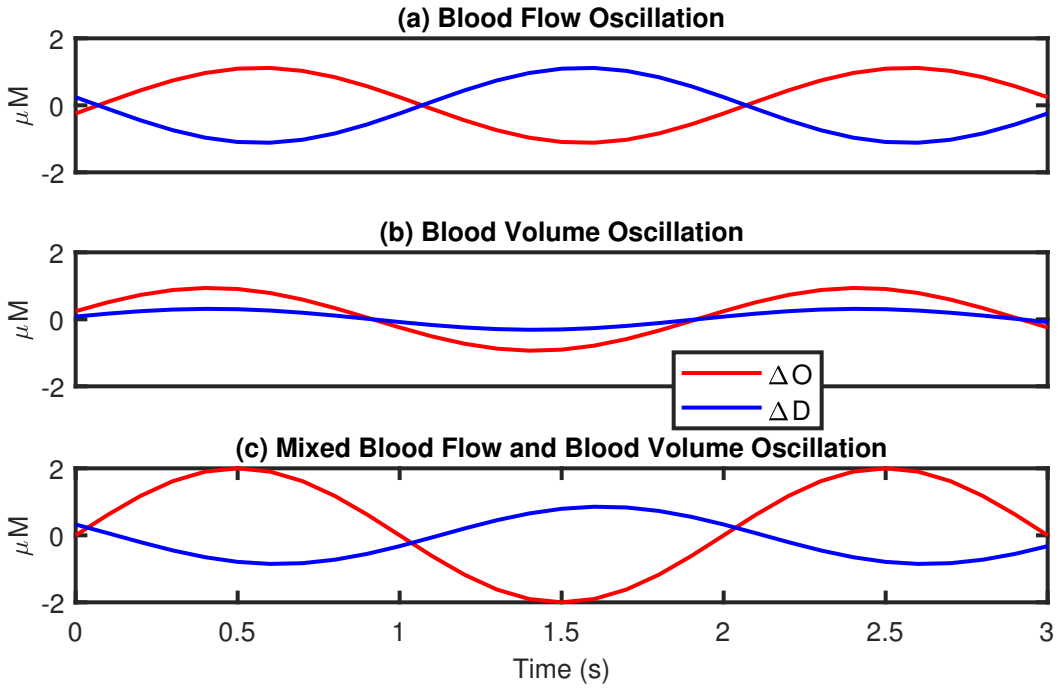

Figure 1.4: Oscillations in Oxy-hemoglobin (O) and Deoxy-hemoglobin (D) that are (a) out of phase and have an amplitude ratio of 1, (b) in phase, and (c) a sum of the oscillations presented in (a) and (b).

1.6 Dissertation Overview

The work in this dissertation aims to improve the assessment of NIRS measurements on skeletal and cerebral hemodynamics by utilizing different measurement methods and exploring the use of spontaneous oscillations in ABP. Chapter 3 explores the feasibility of discriminating superficial and deeper tissue hemodynamics by performing non-invasive optical measurements with rich temporal and spatial information content. This work shows that the data types (I and ϕ) and geometrical arrangements of data collection (SD, DS) result in a set of measurements with a strong dependence on the baseline optical properties and absorption changes in 2-layered media. These relationships can become the basis for discriminating between hemodynamics in the 2-layers.

Additional chapters investigate cerebral hemodynamics utilizing CHS in three different methods. Chapter 4 utilizes DOI with both DS and SD to understand the contributions of

BF and BV. This work is the first implementation of DOI and CHS and shows the potential for spatial mapping of AR. The work then moves to evaluating the potential of spontaneous coherent hemodynamics evaluate cerebral perfusion health, and efficiency of cerebral AR, and ultimately shows the CHS may be based on spontaneous rather than induced ABP. This has important practical implications as subjects would not be required to undergo physiological maneuvers or perturbations. Lastly, results from a pilot clinical study of patients in the NeuroCritical Care Unit (NCCU) (Chapter 6) during a CHS protocol to assess AR is shown and demonstrates the clinical translatability of this technology and processing methods.

Chapter 2

Overarching Methods

This chapter will introduce the methods used throughout this work to analyze Near-InfraRed Spectroscopy (NIRS) signals for Frequency-Domain (FD) and Continuous-Wave (CW). A large portion of the work here focuses on the use of FD-NIRS with the results from Chapter 5 utilizing CW-NIRS. In this work, measurements of the Intensity (I) are utilized for FD and CW, while phase (ϕ) is from FD. Firstly, the forward models utilized in this work are introduced, namely the complex Reflectance ($\widetilde{R}$) and complex fluence rate ($\widetilde{\Phi}$) in a semi-infinite homogeneous medium with extrapolated boundary conditions and then the $\widetilde{R}$ in a layered medium. Next, the recovery of the absorption coefficient (μ_a) and reduced scattering coefficient (μ_s') will be discussed before moving to the calculation of the absorption coefficient change ($\Delta\mu_a$) with different data types. Lastly, I will discuss the calculation of the Sensitivity to an absorption change ($\mathcal{S}$), which utilizes methods described in the sections above. Information in this chapter is the backbone of the methods utilized throughout this work and should be referenced if more detail is needed on how signals are analyzed.

2.1 Forward Models

2.1.1 Diffuse Reflectance and Fluence Rate in a Semi-Infinite Homogeneous Medium

Here we will be utilizing the equation for the complex Reflectance ($\widetilde{R}$) and complex fluence rate ($\widetilde{\Phi}$) in a semi-infinite homogeneous medium with the extrapolated boundary condition [30, 96]. All solutions are calculated for a point-like source ($\vec{r} = (0, 0, \frac{1}{\mu_s'})$) for any point in the diffusive medium ($\vec{r}_k = (x_k, y_k, z_k)$)). The extrapolated boundary is located at z_b,

$$z_b = -\frac{2A}{3\left(\mu_s' + \mu_a\right)} \tag{2.1}$$

where A is parameter that takes into account the refractive index between the diffusive and outer mediums and D is the diffusion factor defined as:

$$D = \frac{1}{3\mu_s'}. \tag{2.2}$$

This leads to the virtual source $\vec{r}_s'$ being located at (0,0,$2z_b - z_0$), where z_0 is $\frac{1}{\mu_s'}$. From here we can define r_1 and r_2 as:

$$\begin{aligned} r_1 &= |\vec{r}_s - \vec{r}_j| \\ r_2 &= |\vec{r}_s' - \vec{r}_j| \end{aligned} \tag{2.3}$$

Using the above definitions the $\widetilde{\Phi}$ can be expressed as

$$\widetilde{\Phi}(\vec{r}_s, \vec{r}_d, \omega) = \frac{1}{4\pi D}\left[\frac{e^{-\widetilde{\mu}_{eff} r_1}}{r_1^2} - \frac{e^{-\widetilde{\mu}_{eff} r_2}}{r_2^2}\right] \tag{2.4}$$

where and $\widetilde{\mu}_{eff}$ is the complex effective attenuation coefficient.

$$\widetilde{\mu}_{eff} = \sqrt{\frac{\mu_a}{D} - i\frac{\omega}{vD}} \tag{2.5}$$

The complex Reflectance ($\widetilde{R}$) defined as the net optical flux exiting the tissue per unit source power can be written as

$$\widetilde{R}(\vec{r}_s, \vec{r}_d, \omega) = \frac{1}{4\pi}\left[z_0 \left(\frac{1}{r_1} + \widetilde{\mu}_{eff}\right)\frac{e^{-\widetilde{\mu}_{eff}r_1}}{r_1^2} + (z_0 - 2z_b)\left(\frac{1}{r_2} + \widetilde{\mu}_{eff}\right)\frac{e^{-\widetilde{\mu}_{eff}r_2}}{r_2^2}\right] \tag{2.6}$$

These solutions consider the FD but setting ω to 0 the equations reduce to the DC expression (for CW-NIRS in this work).

2.1.2 Diffuse Reflectance in a Layered Medium

The solution of the diffusion equation in a two-layered cylindrical medium [97] is utilized in the this work to obtain $\widetilde{R}$. The top layer of the cylindrical medium is set as L_{top} and the second layer extends infinitely in depth, with both layers having a μ_s' and μ_a. All solutions are calculated for a point-like source ($\vec{r}_s = (0, 0, \frac{1}{\mu'_{stop}})$) for any point in the diffusive medium ($r_k = (x_k, y_k, z_k)$)). The approximate extrapolated boundary height is defined as

$$z_b(\mu'_{stop}) = 2AD_{top} \tag{2.7}$$

where A is the index of refraction mismatch and D is the diffusion constant (defined in Equation 2.2) using $\mu'_{s,top}$. Next, a set of coefficients are defined as a function of the k^{th} zero of the 0^{th}-order first kind Bessel function. First, the optical attenuation parameter ($\widetilde{a}_k$):

$$\widetilde{a}_k\left(\mu_{a,top/bot}, \mu'_{s,top/bot}\right) = \sqrt{\frac{\mu_{a,top/bot}}{\mathcal{D}_{top/bot}} + \left(\frac{j_{0,k}}{B}\right)^2 + \frac{\omega}{v\mathcal{D}_{top/bot}}i} \tag{2.8}$$

where, the subscript of μ_a tells whether the variable belongs to the top (*top*) or bottom (*bot*) layer, $j_{0,k}$ is the k^{th} zero of the 0^{th} order Bessel function of the first kind, B is the radius of the two-layer cylinder (for which the source is in the center; B is typically assumed to be 150 mm). Then, the source-detector distance (ρ) parameter (Q_k) is written as

$$Q_k(\rho) = \frac{J_0\left(\frac{\rho j_{0,k}}{B}\right)}{J_1(j_{0,k})^2} \tag{2.9}$$

Now the reflectance for the case when the isotropic source is in the first layer ($\widetilde{R}_1$) can be expressed:

$$\begin{aligned}
&\widetilde{R}_1\left(\rho, \mu_{a,top}, \mu'_{s,top}, z_{top}, \mu_{a,bot}, \mu'_{s,bot}\right) = \\
&\frac{1}{\pi B^2}\sum_{k=1}^{\infty}\Bigg\{\Bigg[\\
&\frac{e^{-\widetilde{a}_{top,k}z_0} + e^{-\widetilde{a}_{top,k}(z_0+2z_b)}}{2} \\
&+\frac{\cosh\left(\widetilde{a}_{top,k}z_0\right)\times\sinh\left(\widetilde{a}_{top,k}(z_0+2z_b)\right)}{e^{\widetilde{a}_{top,k}(z_{top}+z_b)}} \\
&\times\left(\mathcal{D}_{top}\widetilde{a}_{top,k} - \mathcal{D}_{bot}\widetilde{a}_{bot,k}\right) \\
&/\Bigg(\mathcal{D}_{top}\widetilde{a}_{top,k}\cosh\left(\widetilde{a}_{top,k}(z_{top}+z_b)\right) \\
&+\mathcal{D}_{bot}\widetilde{a}_{bot,k}\sinh\left(\widetilde{a}_{top,k}(z_{top}+z_b)\right)\Bigg) \\
&\Bigg]Q_k\Bigg\}
\end{aligned} \tag{2.10}$$

where, z_{top} is the thickness of the top layer. For computation, infinite sums were typically done over 10^3 terms.

To express the reflectance when the isotropic source is in the second layer ($\widetilde{R}_2$) additional coefficients are defined to simplify the expression:

$$\widetilde{\alpha}_{1,k}\left(\mu_{a,top}, \mu'_{s,top}\right) = e^{-\widetilde{a}_{top,k}z_b} \tag{2.11}$$

$$\widetilde{\alpha}_{2,k}\left(\mu_{a,top},\mu'_{s,top},z_{top}\right)=n^2e^{\widetilde{a}_{top,k}z_{top}} \tag{2.12}$$

$$\widetilde{\alpha}_{3,k}\left(\mu_{a,top},\mu'_{s,top},z_{top}\right)= \widetilde{a}_{top,k}\mathcal{D}_{top}e^{\widetilde{a}_{top,k}z_{top}} \tag{2.13}$$

$$\widetilde{\beta}_{1,k}\left(\mu_{a,top},\mu'_{s,top}\right)=e^{\widetilde{a}_{top,k}z_b} \tag{2.14}$$

$$\widetilde{\beta}_{2,k}\left(\mu_{a,top},\mu'_{s,top},z_{top}\right)=n^2e^{-\widetilde{a}_{top,k}z_{top}} \tag{2.15}$$

$$\widetilde{\beta}_{3,k}\left(\mu_{a,top},\mu'_{s,top},z_{top}\right)= -\widetilde{a}_{top,k}\mathcal{D}_{top}e^{-\widetilde{a}_{top,k}z_{top}} \tag{2.16}$$

$$\widetilde{\gamma}_{2,k}\left(z_{top},\mu_{a,bot},\mu'_{s,bot}\right)=-n^2e^{-\widetilde{a}_{bot,k}z_{top}} \tag{2.17}$$

$$\widetilde{\gamma}_{3,k}\left(z_{top},\mu_{a,bot},\mu'_{s,bot}\right)= \widetilde{a}_{bot,k}\mathcal{D}_{bot}e^{-\widetilde{a}_{bot,k}z_{top}} \tag{2.18}$$

$$\widetilde{\zeta}_{2,k}\left(\mu'_{s,top},z_{top},\mu_{a,bot},\mu'_{s,bot}\right)= -\frac{n^2e^{-\widetilde{a}_{bot,k}(z_{top}-z_0)}}{2\widetilde{a}_{bot,k}\mathcal{D}_{bot}} \tag{2.19}$$

$$\widetilde{\zeta}_{3,k}\left(\mu'_{s,top},z_{top},\mu_{a,bot},\mu'_{s,bot}\right)= -\frac{e^{\widetilde{a}_{bot,k}(z_{top}-z_0)}}{2} \tag{2.20}$$

Then combinations of these coefficients are defined.

$$\begin{aligned}\widetilde{\Xi}_k\left(\mu_{a,top},\mu'_{s,top},z_{top},\mu_{a,bot},\mu'_{s,bot}\right)= \\ \widetilde{\alpha}_{1,k}\widetilde{\beta}_{2,k}\widetilde{\gamma}_{3,k}-\widetilde{\alpha}_{1,k}\widetilde{\beta}_{3,k}\widetilde{\gamma}_{2,k} \\ -\widetilde{\alpha}_{2,k}\widetilde{\beta}_{1,k}\widetilde{\gamma}_{3,k}+\widetilde{\alpha}_{3,k}\widetilde{\beta}_{1,k}\widetilde{\gamma}_{2,k}\end{aligned} \tag{2.21}$$

$$\widetilde{\Upsilon}_k\left(\mu_{a,top},\mu'_{s,top},z_{top},\mu_{a,bot},\mu'_{s,bot}\right)= -\frac{\widetilde{\beta}_{1,k}(\widetilde{\gamma}_{2,k}\widetilde{\zeta}_{3,k}-\widetilde{\gamma}_{3,k}\widetilde{\zeta}_{2,k})}{\widetilde{\Xi}_k} \tag{2.22}$$

$$\widetilde{\Psi}_k\left(\mu_{a,top},\mu'_{s,top},z_{top},\mu_{a,bot},\mu'_{s,bot}\right) = \frac{\widetilde{\alpha}_{1,k}(\widetilde{\gamma}_{2,k}\widetilde{\zeta}_{3,k}-\widetilde{\gamma}_{3,k}\widetilde{\zeta}_{2,k})}{\widetilde{\Xi}_k} \tag{2.23}$$

Given all these coefficients the reflectance when the isotropic source is in the second layer ($\widetilde{R}_2$) can now be expressed:

$$\widetilde{R}_2\left(\rho,\mu_{a,top},\mu'_{s,top},z_{top},\mu_{a,bot},\mu'_{s,bot}\right) = \frac{1}{\pi B^2}\sum_{k=1}^{\infty}\left\{\left[\mathcal{D}_{top}\widetilde{a}_{top,k}(\widetilde{\Upsilon}_k-\widetilde{\Psi}_k)\right]Q_k\right\} \tag{2.24}$$

where, as before, the sum was typically done over 10^3 terms.

Finally, the piece-wise expression for $\widetilde{R}$ from a two-layer medium may be expressed:

$$\widetilde{R}\left(\rho,\mu_{a,top},\mu'_{s,top},z_{top},\mu_{a,bot},\mu'_{s,bot}\right) = \begin{cases}\widetilde{R}_1 & z_0 < z_{top}\\ \widetilde{R}_2 & z_0 \geq z_{top}\end{cases} \tag{2.25}$$

Reflectance (R) for CW may be obtained by setting angular modulation frequency (ω) to zero.

2.2 Recovery of Absolute Optical Properties

Measurements of absolute optical properties, namely μ_a and μ'_s, in a semi-infinite homogeneous medium using an extrapolated boundary condition are possible using both I and ϕ from FD-NIRS. Here we will represent measured I and ϕ in the form of the $\widetilde{R}$. There are two source-detector arrangements used in this work to calculate μ_a and μ'_s, which are Multi-Distance (MD) and Self-Calibrating (SC). Both of these methods use the slopes of the linearized I ($ln(\rho^2 I)$) and ϕ versus ρ with the MD method typically utilizing more then 2 ρs. The distances included in these measurements are typically in the range of 5 mm to

40 mm depending on the dynamic range of the instrumentation. The MD approach requires a calibration on an tissue-mimicking optical phantom with known optical properties to subtract the coupling terms from the sources. This method assumed that the optical coupling between the probe and phantom is the same as the tissue and phantom. The SC method on the other hand does not require calibration [43].

Absolute μ_a and μ_s' for both the MD and SC method utilized an iterative method based on a semi-infinite homogeneous medium and extrapolated boundary condition (subsection 2.1.1). Briefly, this method uses the $\widetilde{R}$ versus ρ, and an initial guess of the complex effective attenuation coefficient ($\widetilde{\mu}_{eff}$) using assumptions of linearity and finds μ_a and μ_s' by iteratively solving the analytical equation for $\widetilde{R}$ in a semi-infinite homogeneous medium. More detail on this method can be found in Blaney *et al* (2021) [98].

2.3 Relative Measurements of Hemoglobin Concentrations

Changes in the I or ϕ for Single-Distance (SD), Single-Slope (SS), or Dual-Slope (DS) methods can be translated into $\Delta\mu_a$. Below are the equations and method used to achieve this.

2.3.1 Generalized Optical Pathlength

Calculation of the general complex total optical path-length ($\langle\widetilde{L}\rangle$) is the first step in the calculation of $\Delta\mu_a$ for all data types. $\langle\widetilde{L}\rangle$ depends on ρ, μ_s', and μ_a, leading to it being calculated for each subject, ρ, and optical wavelength (λ) in this work unless specified. The equation for $\langle\widetilde{L}\rangle$ in a semi-infinite medium with extrapolated boundary conditions is expressed as:

$$\langle\widetilde{L}\rangle(\vec{r}_s,\vec{r}_d) = \frac{1}{8\pi D\widetilde{R}}\left[\frac{z_0}{r_1}e^{-\widetilde{\mu}_{eff}r_1} + \frac{z_0-2z_b}{r_2}e^{-\widetilde{\mu}_{eff}r_2}\right] \tag{2.26}$$

where $\widetilde{R}$, D, $\vec{r}_s$, $\vec{r}_d$, z_0, z_b, r_1, and r_2 are previously defined in subsection 2.1.1. For use with either I or ϕ the either the either the real ($\Re$) or imaginary ($\Im$) portion of $\langle\widetilde{L}\rangle$:

$$\begin{aligned}\langle L\rangle_I &= \Re(\langle\widetilde{L}\rangle)\\ \langle L\rangle_\phi &= \Im(\langle\widetilde{L}\rangle)\end{aligned} \tag{2.27}$$

where $\Re$ is the real part and $\Im$ is the imaginary part of the complex number. For the case of measurements from CW, the total optical path-length ($\langle L\rangle$) can be determined by setting ω to 0. In this case, the $\langle L\rangle$ has a clear meaning of the average length of the path a photon travels from the source to the detector.

2.3.2 Single Distance

Measurements of the I or ϕ between one optical source and one detector is called SD. Changes in I or ϕ measured in the SD configuration can then translated into $\Delta\mu_a$. Considering a baseline period of I_0 and ϕ_0 the $\Delta\mu_a$ can be calculated as:

$$\Delta\mu_{aSDI} = \frac{\ln(SDI_0/SDI)}{\rho DPF_I} = -\frac{\Delta SDI/SDI_0}{\langle L\rangle_I} \tag{2.28}$$

$$\Delta\mu_{aSD\phi} = -\frac{\Delta SD\phi}{\langle L\rangle_\phi} \tag{2.29}$$

where ρ is the source detector distance and DPF is the Differential path length factor. The Differential Path-length Factor (DPF) can be defined as:

$$DPF_I = \frac{\langle L\rangle_I}{\rho}; \tag{2.30}$$

$$DPF_\phi = \frac{\langle L\rangle_\phi}{\rho}. \tag{2.31}$$

2.3.3 Slope Methods

The use of multiple SD measurements allow for the use of the slope of optical data versus ρ and is called SS. SSs and are based on the slopes of the linearized I ($\ln(\rho^2 I)$) or ϕ versus ρ and can be used to calculate $\Delta\mu_a$ using the following equations:

$$\begin{aligned} \Delta\mu_{a_{SSI}} &= -\frac{\Delta SSI}{DSF_I} \\ \Delta\mu_{a_{SS\phi}} &= -\frac{\Delta SS\phi}{DSF_\phi} \end{aligned} \tag{2.32}$$

where Single-Slope Intensity (SSI) is the slope of the linearized I ($\ln(\rho^2 I)$) versus ρ, Sinlge Slope phase (SSϕ) is the slope of ϕ versus ρ, and DSF is the Differential Slope Factor for I and ϕ. The Differential Slope Factor (DSF) for I and ϕ is defined as:

$$\begin{aligned} DSF_I &= \frac{\sum_{i=1}^{n} (\rho_i - \bar{\rho}) \langle L \rangle_I [\vec{r}_{src}, \vec{r}_{det,i}]}{\sum_{i=1}^{N_I} (\rho_i - \bar{\rho})^2} \\ DSF_\phi &= \frac{\sum_{i=1}^{n} (\rho_i - \bar{\rho}) \langle L \rangle_\phi [\vec{r}_{src}, \vec{r}_{det,i}]}{\sum_{i=1}^{N_I} (\rho_i - \bar{\rho})^2} \end{aligned} \tag{2.33}$$

The DS is the averaging two SS sets (i.e., SS_1 and SS_2) and as such the equation for calculated $\Delta\mu_a$ for either Dual-Slope Intensity (DSI) or Dual Slope phase (DSϕ) is defined as:

$$\begin{aligned} \Delta\mu_{a_{DSI}} &= \frac{\Delta SSI_1 + \Delta SSI_2}{DSF_{I,SS_1} + DSF_{I,SS_2}} \\ \Delta\mu_{a_{DS\phi}} &= \frac{\Delta SS\phi_1 + \Delta SS\phi_2}{DSF_{\phi,SS_1} + DSF_{\phi,SS_2}}. \end{aligned} \tag{2.34}$$

Note that if the ρs in both SS sets are the same, the DSF for both SS sets will be the same, with the simplified version being reported in [31]. The two SSs that are utilized in the DS must meet the requirements of [44, 99]:

- The difference between ρ_1 and ρ_2 for SS_1 and SS_1 must be the same.
- The short ρ for SS_1 must be the long for SS_2.

The DS arrangement is the same as the SC [43] for achieving calibration free absolute optical properties, as such it has the same artifact removal. The artifacts that can be removed include the cancellation of detector gain changes, source power changes, and optode coupling efficiency which are due to multiplicative changes in I and additive changes in ϕ.

2.3.4 Translation Into Changes in Hemoglobin Concentrations

Measured $\Delta\mu_a$ at a wavelengths λ_i with data types described above can be translated into c chromorphore concentrations. This can be done using utilizing the following equation:

$$\Delta\mu_a(\lambda_j) = \sum_{j=1}^{n_c} C_j \epsilon_j \tag{2.35}$$

where ϵ_j is the extinction, C_j is j_{th} the chromophore concentration, and n_c is the number of absorbers. Figure 2.1 shows the extinction coefficient (ϵ) spectra for the chromphores Oxy-hemoglobin (O), Deoxy-hemoglobin (D), Water (W) and Lipid (L). The two dominant absorbers within this λ window are O and D. This work focuses on the the use of O and D at two λs, specifically 690 nm and 830 nm.

2.4 Sensitivity to a Local Absorption Perturbation

The Sensitivity to an absorption change ($\mathcal{S}$) can be defined as:

$$\mathcal{S}_i\left(\vec{r}_j\right) = \frac{\left[\Delta\mu_{a,recovered}\right]_i}{\Delta\mu_{a,true}\left(\vec{r}_j\right)} \tag{2.36}$$

which shows the $\mathcal{S}$ of measurement i which measures an apparent absorption change of $\left[\Delta\mu_{a,recovered}\right]_i$ when there is an actual absorption change of $\Delta\mu_{a,true}$ at position $\vec{r}_j$. This $\mathcal{S}$ is defined for one position and when summed across the whole medium is 1. This allows for the understanding of what the $\Delta\mu_{a_{measured}}$ at a certain voxel will be given its $\mathcal{S}$ and $\Delta\mu_{a_{true}}$. Calculation of the $\mathcal{S}$ is done using the $\langle\widetilde{L}\rangle$ (defined in Section 2.3.1) and the general complex

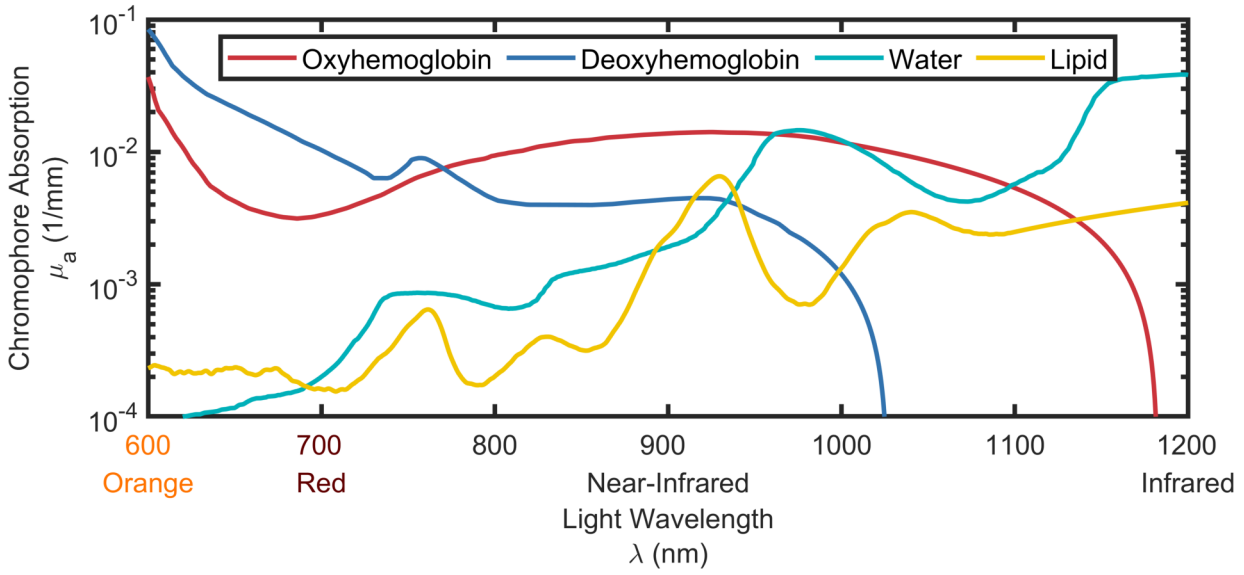

Figure 2.1: Extinction coefficient (ϵ) for Oxy-hemoglobin (O), Deoxy-hemoglobin (D), Water (W), and Lipid (L).

partial optical path-length ($\langle\widetilde{\ell}\rangle$). The $\langle\widetilde{\ell}\rangle$ is the path of through a localized region within the diffuse medium with a Volume (V) and can be defined as:

$$\langle\widetilde{\ell}\rangle = \frac{\widetilde{\Phi}\left[\vec{r}_{src}, \vec{r}_{pert}\right]\widetilde{R}\left[\vec{r}_{pert}, \vec{r}_{det}\right]}{\widetilde{R}\left[\vec{r}_{src}, \vec{r}_{det}\right]}V \tag{2.37}$$

where the isotropic source is at the location of and the position for the detector is at a source detector distance (ρ) away and is the position of the localized perturbation. As with $\langle\widetilde{L}\rangle$ (subsection 2.3.1), the $\langle\widetilde{\ell}\rangle$ can be defined for I and ϕ by:

$$\begin{aligned}\langle L\rangle_I &= \Re(\langle\widetilde{\ell}\rangle)\\ \langle L\rangle_\phi &= \Im(\langle\widetilde{\ell}\rangle).\end{aligned} \tag{2.38}$$

Considering SD first, the $\mathcal{S}$ can be expressed for I and ϕ as:

$$\begin{aligned}\mathcal{S}_{SDI} &= \frac{\langle\ell\rangle_I}{\langle L\rangle_I}\\ \mathcal{S}_{SD\phi} &= \frac{\langle\ell\rangle_\phi}{\langle L\rangle_\phi}\end{aligned} \tag{2.39}$$

where partial optical path-length ($\langle \ell \rangle$) is written in Equation 2.37 and $\langle L \rangle$ in Equation 2.26.

Next, we can define the $\mathcal{S}$ for SS [31] where the SSs are made from N_{SD} SD sets with a single source at position vector ($\vec{r}$) of $\vec{r}_{src}$ and N_{SD} detectors indexed by i at $\vec{r}$s of $\vec{r}_{src,det}$ as:

$$\begin{aligned} \mathcal{S}_{SSI} &= \frac{\sum_{i=1}^{N_{SD}} (\rho_i - \bar{\rho}) \langle \ell \rangle_I [\vec{r}_{src}, \vec{r}_{det,i}]}{\sum_{i=1}^{N_{SD}} (\rho_i - \bar{\rho}) \langle L \rangle_I [\vec{r}_{src}, \vec{r}_{det,i}]} \\ \mathcal{S}_{SS\phi} &= \frac{\sum_{i=1}^{N_{SD}} (\rho_i - \bar{\rho}) \langle \ell \rangle_\phi [\vec{r}_{src}, \vec{r}_{det,i}]}{\sum_{i=1}^{N_{SD}} (\rho_i - \bar{\rho}) \langle L \rangle_\phi [\vec{r}_{src}, \vec{r}_{det,i}]} \end{aligned} \tag{2.40}$$

Lastly, the $\mathcal{S}$ for the DS that is comprised of two symmetric SSs (SS_1 and SS_2) can be defined as:

$$\begin{aligned} \mathcal{S}_{DSI} &= \frac{\mathcal{S}_{SSI,1} + \mathcal{S}_{SSI,1}}{2} \\ \mathcal{S}_{DS\phi} &= \frac{\mathcal{S}_{SS\phi,1} + \mathcal{S}_{SS\phi,1}}{2} \end{aligned} \tag{2.41}$$

It is important to note that in a laterally homogeneous medium, the $\mathcal{S}$ for DS and SS are same.

Chapter 3

Assessing Skeletal Muscle Hemodynamics

3.1 Introduction

Near-InfraRed Spectroscopy (NIRS) has been applied to measurements of the perfusion and oxygenation of skeletal muscle [68, 100]. Contribution from superficial tissue has been apparent in skeletal muscle measurements with NIRS. This chapter aims to differentiate these superficial and deep hemodynamics to allow for a measurement more representative of skeletal muscle.

NIRS studies have employed Continuous-Wave (CW) [20, 72, 101, 102], Time-Domain (TD) [103], and Frequency-Domain (FD) [104, 105] systems, which are based on constant, pulsed, and intensity-modulated illumination, respectively (as described in subsection 1.3.1). Non-invasive NIRS measurements of skeletal muscle must take into account potentially confounding contributions to the optical signals from superficial tissue, namely skin and adipose tissue [100]. It was observed that non-invasive NIRS measurements on skeletal muscle need to be corrected for Adipose Tissue Thickness (ATT) to yield values that are representative of muscle tissue [20, 35, 106]. To achieve this aim, TD-NIRS data was used either to generate

correction curves derived from the ratio of the partial optical path-length in muscle to the total optical path-length [103], or to yield separate measurements for the top layer (adipose tissue) and bottom layer (muscle) by modeling the tissue as a two-layered medium [107]. CW-NIRS for skeletal muscle measurements has been commonly implemented by placing a single illumination point (source) and a single optical collection point (detector) on the tissue surface. This arrangement is commonly called called Single-Distance (SD). In this approach, the measured quantity is the optical Intensity (I) as well as its changes associated with muscle hemodynamics (ΔI) [20, 35]. These Single-Distance Intensity (SDI) measurements are known to have a greater sensitivity to superficial tissue compared to Single Distance phase (SDϕ) measurements obtained with FD-NIRS [31, 92]. Here, ϕ is the phase of the photon-density waves that result from modulated illumination.

One method that has been applied to the brain [19, 31, 92], and skeletal muscle [108] is the Dual-Slope (DS). The DS approach has shown preferential sensitivity to deeper hemodynamics for both I and phase (ϕ) as compared to traditional SDI measurements, thus offering promise in limiting the contribution of adipose tissue to NIRS measurements. DS measurements are the average of two paired Single-Slopes (SSs) that represent the slopes as functions of I and ϕ (to a first approximation, $\ln(\rho^2 I)$ and ϕ) versus source-detector distance (ρ).

Two commonly used protocols to assess skeletal muscle Blood Flow (BF) and Oxygen Consumption (OC) involve the use of a Venous Occlusion (VO) and an Arterial Occlusion (AO), respectively. These protocol cause hemodynamic and oxygenation changes in limb tissues (skeletal muscle, skin, adipose tissue, etc.) that are distal to the pneumatic cuff used to perform the vascular occlusion. VOs are achieved by inflating a pneumatic cuff that is wrapped around the limb to a pressure of 40 mmHg to 60 mmHg, which is above venous pressure, effectively causing the accumulation of blood. Such protocols have been used to measure muscle BF from the initial rate of accumulation of blood following the onset of the occlusion [72, 75, 100]. Previous work has shown that BF in adipose tissue is greater than in

skeletal muscle at rest[57], and was confirmed utilizing NIRS measurements performed on a population of 78 subjects with ATT ranging from 1.5 mm to 9 mm [20]. AOs operate in the same mannerism, with the inflation pressure instead adjusted to ∼200 mmHg, which is above the systolic pressure, effectively blocking both the blood inflow and outflow to the measured tissue [109]. These measurements are used to measure the OC, due to the absence of blood redistribution within the muscle and the oxygen desaturation of hemoglobin that occurs, this occlusion causes equal rates of the decrease of Oxy-hemoglobin (O) and increase of Deoxy-hemoglobin (D). Adipose tissue has been shown to have a lower oxygen consumption than skeletal muscle at rest [20, 57, 110]. The different hemodynamic behavior of adipose tissue and muscle tissue during a VO and AO render these protocols useful tools to investigate the relative sensitivity of NIRS measurements to adipose and muscle tissues.

This chapter uses the DS method with both I and ϕ measurements during either an AO or VO on four subjects. We then performed simulations in a two-layer medium that were guided by experimental results to examine the effect of different baseline tissue properties, different absorption changes in the two layers, and different top layer thicknesses.

3.2 Methods

3.2.1 Experimental Protocol and Instrumentation

A total of 4 subjects (3 Female (F), 1 Male (M); age range 22 yr to 29 yr) participated in a Tufts University Institutional Review Board (IRB) approved study for FD-NIRS measurements conducted on the human forearm. Two experimental protocols, one involving VO and one involving AO, are schematically illustrated in Figure 3.1(a). The VO protocol consisted of a 1 min baseline, followed by 1 min of venous occlusion achieved by inflating a pneumatic cuff wrapped around the upper arm to a pressure of 60 mmHg and a final 1 min recovery. The AO protocol consisted of a 1 min baseline followed by 3 min AO achieved by inflating a pneumatic cuff wrapped around the upper arm to a pressure of 220 mmHg and a final 3 min

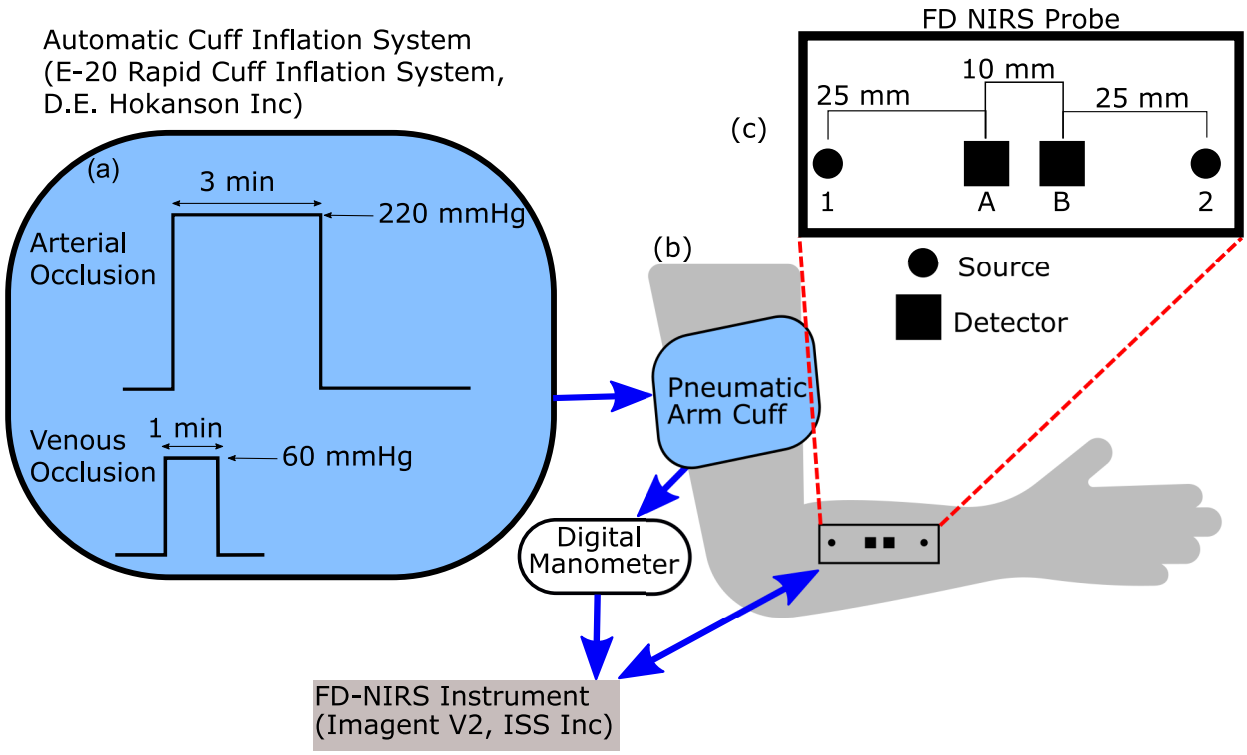

Figure 3.1: Experimental setup for Frequency-Domain (FD)-Near-InfraRed Spectroscopy (NIRS) measurements on the human forearm during a Arterial Occlusion (AO) or Venous Occlusion (VO). (a) Shows the timing of AO and VO achieved by inflation of a pneumatic arm cuff using an automatic cuff inflation system (E-20 Rapid Cuff Inflation System, D.E. Hokanson, Inc [Bellevue, WA USA] (automatic cuff inflation system)). (b) A pneumatic arm cuff (SC12D, D.E. Hokanson, Inc [Bellevue, WA USA]) was placed on the subject's upper arm. The cuff pressure was measured continuously using a Series 626 Pressure Transmitter Dwyer Instruments Inc [Michigan City, IN USA] (digital manometer) and recorded synchronously with the data collected by the FD-NIRS system (ISS Imagent V2 [Champaign, IL USA]). An optical probe connected to the FD-NIRS system was placed on the forearm above the brachioradialis muscle. (c) Schematic of the FD-NIRS optical probe with numbers used to label optical sources and letters refer to detectors. This arrangement allowed for two Single-Distance (SD) measurements at a source-detector separation of 25 mm (1A & 2B), two SD measurements at a source-detector separation of 35 mm (1B & 2A), and one Dual-Slope (DS) measurement based on data collected by all combinations of sources and detectors (1AB2).

recovery. Subjects 2 and 4 participated in both protocols, subject 1 only in the AO protocol and subject 3 only in the VO protocol, as listed in Table 3.1.

All subjects were placed in a seated position with the right forearm on a flat surface. Before starting the experiment, ATT was measured with a skin fold caliper at the measurement

location and is reported in Table 3.1. First, a pneumatic arm cuff (SC12D, D.E. Hokanson, Inc [Bellevue, WA USA]) was placed on the upper right arm (Figure 3.1(b)). The cuff pressure was controlled automatically using a automatic cuff inflation system (E-20 Rapid Cuff Inflation System, D.E. Hokanson, Inc [Bellevue, WA USA]) to inflate the cuff to the desired pressure. The cuff pressure was measured continuously using a digital manometer (Series 626 Pressure Transmitter Dwyer Instruments Inc [Michigan City, IN USA]) and the pressure data was recorded synchronously with the FD-NIRS data.

An optical probe for FD-NIRS measurements was placed on the forearm over the brachioradialis muscle and secured via black athletic bandaging to guarantee good contact with the skin. The optical probe contained two pairs of illumination optical fibers and two collection optical fiber bundles that were connected to the light sources and optical detectors, respectively, of a commercial ISS Imagent V2 [Champaign, IL USA] (modulation frequency: 140.625 MHz). Each pair of illumination fibers delivered light at two wavelengths through connection to laser diodes that emitted light at 690 nm and 830 nm. The light sources were time-multiplexed, so only one source was on at any time. The sampling rate for data collection ranged from $\sim$2 Hz to 10 Hz, where the cause of differing sampling rates was due to increased integration time for each source-detector pair to decrease phase noise. The two optical collection points in the optical probe are labeled A and B, whereas the two source locations (each featuring illumination at two wavelengths) are labeled 1 and 2 (Figure 3.1(c)). This arrangement allows for two SD measurements at a source-detector separation of 25 mm (1A and 2B), two SD measurements at a source-detector separation of 35 mm (1B and 2A), and one DS measurement (1AB2) that combines data collected by all source and detector combinations.

3.2.2 Theoretical Simulations

An analytical approach based on diffusion theory for a two-layer medium [97, 111] with an infinitely thick bottom layer was used to guide the interpretation of the experimental results

from both occlusion protocols. This model is expanded upon in subsection 2.1.2. For each simulation, we defined specific values of the absorption coefficient (μ_a) in the top and bottom layers ($\mu_{a,\text{top}}$ and $\mu_{a,\text{top}}$, respectively), the reduced scattering coefficient (μ'_s) in the top and bottom layers ($\mu'_{s,\text{top}}$ and $\mu'_{s,\text{bot}}$, respectively), and the top layer thickness (L_{top}). We then computed the complex Reflectance ($\widetilde{R}$), whose amplitude (I) and phase (ϕ) represent the FD-NIRS signal, for each source-detector pair of the probe geometry in Figure 3.1(c). This $\widetilde{R}$ was used to obtain the effective optical properties at baseline, as described in subsection 3.2.3. Absorption perturbations in the top and bottom layers ($\Delta\mu_{a,\text{top}}$ and $\Delta\mu_{a,\text{bot}}$, respectively) were then introduced, and the associated change in $\widetilde{R}$ ($\Delta\widetilde{R}$) was calculated. Finally, the absorption coefficient change ($\Delta\mu_a$) associated with $\Delta\widetilde{R}$ were obtained as described in subsection 3.2.3. Processing for experimental and simulated data followed the same processing flow to allow for fair comparison.

To study the effect of the different parameters of the two-layer medium (L_{top} and optical properties of the two layers) on the recovered $\Delta\mu_a$, top and bottom layer μ_a, μ'_s, and L_{top} were varied. In all simulations, three cases of $\Delta\mu_{a,\text{top}}$ and$\Delta\mu_{a,\text{bot}}$ were considered: 1) $\Delta\mu_{a,\text{top}} < \Delta\mu_{a,\text{bot}}$, 2) $\Delta\mu_{a,\text{top}} = \Delta\mu_{a,\text{bot}}$, and 3) $\Delta\mu_{a,\text{top}} > \Delta\mu_{a,\text{bot}}$. These cases were chosen to represent the different hemodynamic responses in the two layers during the two occlusions considered: lower OC in superficial adipose tissue vs. muscle tissue at rest (i.e., $|\Delta\mu_{a,\text{top}}| < |\Delta\mu_{a,\text{bot}}|$ during an AO) and greater BF in superficial adipose tissue vs. muscle tissue at rest (i.e., $\Delta\mu_{a,\text{top}} > \Delta\mu_{a,\text{bot}}$) during a VO). The optical properties of the two layers at baseline were chosen so that the effective optical properties (defined in subsection 3.2.3) were within the range of those measured experimentally (Table 3.1).

3.2.3 Determining Effective Optical Properties and Absorption Changes

Methods described here were applied to both experimental and simulated data $\widetilde{R}$ data. Effective optical properties, μ_a and μ'_s (for each wavelength in the case of experimental data), were calculated using a multi-distance iterative recovery method [98] based on a semi-

infinite homogeneous medium with extrapolated boundary conditions. The optical probe was used in the Self-Calibrating (SC) configuration [43], which allows one to collect Dual-Slope Intensity (DSI) and Dual Slope phase (DSϕ) to yield effective μ_a and μ_s'. For the experimental data described in subsection 3.2.1, effective μ_a and μ_s' at baseline were taken as the average over time from the start of the experiment to 1 s before the start of cuff inflation. Table 3.1 reports the effective μ_a and μ_s' for each subject, experimental protocol, and wavelength.

Changes in I or ϕ recorded over a time interval Δt at a single source-detector separation (called SD) ρ were translated into associated $\Delta\mu_a$ according to the expressions in section 2.3 utilizing the μ_a and μ_s' calculated at each optical wavelength (λ) and ρ (as reported in Table 3.1) to compute the total optical path-length ($\langle L\rangle$) for I and ϕ. The $\langle L\rangle$ is essentially the opposite of the partial derivative of the data type M (I or ϕ) with respect to the μ_a and was calculated using the calculated effective μ_a and μ_s' for each λ and ρ as reported in Table 3.1. Note that $\langle L\rangle_M/\rho$ is the conventional Differential Path-length Factor (DPF) (defined in section 2.3) in the case of I data, whereas it can be seen as a generalized DPF for the ϕ in the case of ϕ data. We averaged the two SD data collected by two different SD pairs at the same ρ, leading to a single value for each of $\langle L\rangle_I(\rho_1)$, $\langle L\rangle_I(\rho_2)$, $\langle L\rangle_\phi(\rho_1)$, and $\langle L\rangle_\phi(\rho_2)$, where $\rho_1 = 25\,\text{mm}$ and $\rho_2 = 35\,\text{mm}$. From these values of generalized path-lengths, we computed a Differential Slope Factor (DSF) for data type M (DSF_M) as follows (a simplified version of Equations reported in subsection 2.3.3):

$$\text{DSF}_M(\rho_1,\rho_2) = \frac{\langle L\rangle_M(\rho_2) - \langle L\rangle_M(\rho_1)}{\rho_2 - \rho_1}. \tag{3.1}$$

Changes in the DS for both I and ϕ where then computed utilizing the methods reported in subsection 2.3.3)

Table 3.1: Summary of the baseline measurements for each subject before the Arterial Occlusion (AO) and Venous Occlusion (VO) protocols. Adipose Tissue Thickness (ATT) for each subject is reported as the mean ± standard deviation over 3 skin fold caliper measurements. The mean ± standard deviation for the absorption coefficient (μ_a) and reduced scattering coefficient (μ_s') during the baseline period at the two wavelengths of 690 nm and 830 nm is reported for each subject, along with the total optical path-length ($\langle L \rangle$) for the Intensity (I) ($\langle L \rangle_I$) and phase (ϕ) ($\langle L \rangle_\phi$). $\langle L \rangle_I$ and $\langle L \rangle_\phi$ are reported for both wavelengths and source-detector distance (ρ): $\rho_1 = 25$ mm and $\rho_2 = 35$ mm

Prot			μ_a (mm^{-1})		μ_s'(mm^{-1})		$\langle L \rangle_I$(mm)				$\langle L \rangle_\phi$(mm)			
	Sub	ATT (mm)	690 nm	830 nm	690 nm	830 nm	690 nm	830 nm	690 nm	830 nm	690 nm	830 nm	690 nm	830 nm
							ρ_1	ρ_2	ρ_1	ρ_2	ρ_1	ρ_2	ρ_1	ρ_2
AO	1	2.0 ± 0.3	0.0172 ± 0.0007	0.0160 ± 0.0004	0.58 ± 0.01	0.56 ± 0.01	106	153	107	154	10.3	15.6	11.1	16.8
	2	3.4 ± 0.2	0.0161 ± 0.0002	0.0190 ± 0.0001	0.551 ± 0.003	0.477 ± 0.003	106	152	92.7	133	10.8	16.4	8.15	12.2
	4	6.0 ± 0.5	0.0198 ± 0.0001	0.01756 ± 0.00008	0.581 ± 0.003	0.596 ± 0.003	100	144	106	153	8.64	13.0	10.2	15.4
VO	2	3.4 ± 0.2	0.0150 ± 0.0001	0.0177 ± 0.0001	0.560 ± 0.003	0.514 0.003	109	158	98.6	142	12.0	18.2	9.26	13.9
	3	4.4 ± 0.2	0.0156 ± 0.0003	0.0185 ± 0.0003	0.547 ± 0.006	0.494 ± 0.006	107	154	95.1	136	11.3	17.1	8.57	12.9
	4	6.0 ± 0.5	0.0185 ± 0.0004	0.01839 ± 0.00009	0.571 ± 0.002	0.598 ± 0.003	102	147	105	151	9.30	14.0	9.61	14.5

Acronyms: Adipose Tissue Thickness (ATT), absorption coefficient (μ_a), reduced scattering coefficient (μ_s'), Arterial Occlusion (AO), Venous Occlusion (VO), Protocol (Prot), Subject (Sub), total optical path-length ($\langle L \rangle$), Intensity (I), phase (ϕ), source-detector distance (ρ)

3.3 Results

3.3.1 Measurements *in-vivo*

Effective Optical Properties

Effective optical properties of the forearm tissue were measured at baseline (described in 3.2.3) before performing either an AO or VO. These effective optical properties were used to calculate the generalized optical path-length for intensity ($\langle L \rangle_I$) and generalized optical path-length for phase ($\langle L \rangle_\phi$) at each wavelength (690 nm and 830 nm) and at each ρ (25 mm and $\rho_2 = 35$ mm) (see Table 3.1) by considering a semi-infinite homogeneous medium. $\langle L \rangle_I$ and $\langle L \rangle_\phi$ then yield a DSF_I and DSF_ϕ according to Equation 3.1. A comparison of the

baseline effective optical properties measured on subjects 2 and 4 before the AO and VO (subjects 2 and 4 participated in both protocols) shows differences to within about 6 %. These differences can be attributed to different hemodynamic conditions and measurement errors as they exceed the standard deviations over the baseline period reported in Table 3.1, which represent the measurement precision.

Absorption Changes Associated with Vascular Occlusions

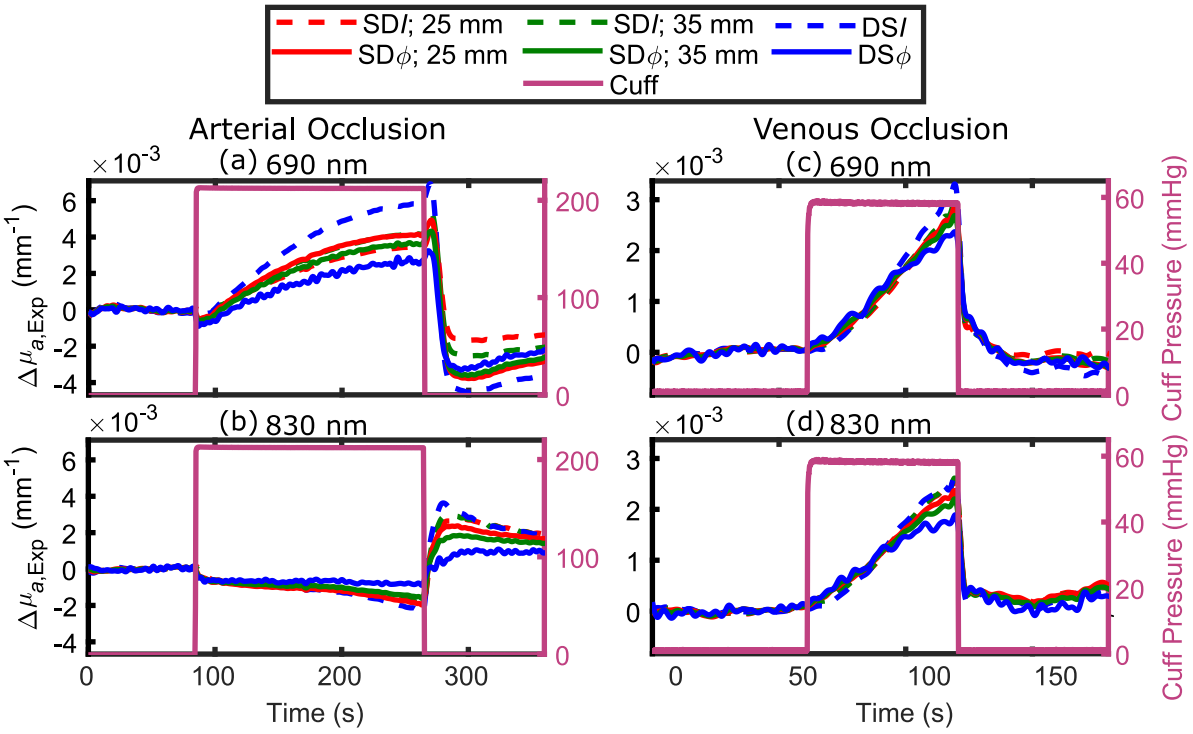

Figure 3.2: Representative time traces of experimentally measured absorption coefficient change ($\Delta\mu_a$) ($\Delta\mu_{a,\mathrm{Exp}}$) during an AO (panels (a) and (b): Subject 4) and VO (panels (c) and (d): Subject 2). For each occlusion type, data are shown at wavelengths of 690 nm (panels (a) and (c)) and 830 nm (panels (b) and (d)). Each subplot contains time traces of $\Delta\mu_{a,\mathrm{Exp}}$ calculated using data from Single-Distance Intensity (SDI) at 25 mm (dashed red) and 35 mm (dashed green), Single Distance phase (SDϕ) at 25 mm (solid red) and 35 mm (solid green), Dual-Slope Intensity (DSI) (dashed blue), and Dual Slope phase (DSϕ) (solid blue). Co-registered time traces of the measured arm cuff pressure are shown in pink and scaled according to the right axes. All measurements have been low-pass filtered to 0.2 Hz.

Figure 3.2 shows representative time traces of the experimental $\Delta\mu_a$ ($\Delta\mu_{a,\mathrm{Exp}}$) obtained

with SD and DS I and ϕ data during AO in subject 4 (Figure 3.2(a): 690 nm; Figure 3.2(b): 830 nm) and during a VO in subject 2 (Figure 3.2(c): 690 nm; Figure 3.2(d): 830 nm). All temporal traces of $\Delta\mu_{a,\mathrm{Exp}}$ have been low-pass filtered to 0.2 Hz to help visualization by removing fast fluctuations and oscillations at the heart rate. Note that greater noise is typically associated with ϕ data. The measured $\Delta\mu_{a,\mathrm{Exp}}$ at the two wavelengths reflect the changes in tissue concentrations of Oxy hemoglobin and myoglobin concentration change (ΔO) and Deoxy hemoglobin and myoglobin concentration change (ΔD) in the tissue during the occlusions. During an AO, BF is blocked in and out of the measured limb, causing an increase in Deoxy hemoglobin and myoglobin (D) ($\Delta D > 0$) and a decrease of the same magnitude in Oxy hemoglobin and myoglobin (O) ($\Delta O < 0$) due to OC in the tissue. At 690 nm ΔD has a greater extinction coefficient (ϵ) than ΔO and the opposite is true at 830 nm which translated into an increase in $\Delta\mu_a$ at 690 nm and a decrease in μ_a at 830 nm, as seen in Figure 3.2(a) and Figure 3.2(b). At the onset of the AO, a motion artifact that lasts approximately 1 s to 2 s is noticeable at both wavelengths for all data types. This artifact is also visible in DS data types, even though they should be largely insensitive to changes in the optical coupling between sources and detectors [31, 112]. A possible reason for this artifact to appear in DS data is that the optical coupling change may have occurred faster than the data sampling cycle through all sources and detectors. No motion artifact is visible at the onset of the VO (Figure 3.2(c) and Figure 3.2(d)), possibly as a result of the lower cuff inflation pressure in this case. During a VO, only the outflow of blood is blocked (at least initially) from the measured limb, so that there is blood pooling and an increase in the Total hemoglobin and myoglobin (T) in the tissue. Consequently, $\Delta\mu_a$ increases at both wavelengths, as seen in Figure 3.2(c) and Figure 3.2(d).

Differences in the maximum absorption changes obtained with the six data types (namely, SDI and SDϕ at 25 mm, SDI and SDϕ at 35 mm, and DSI and DSϕ) during and after the two vascular occlusion protocols can be seen in Figure 3.2. These differences indicate a different spatial sensitivity of the various data types to in-homogeneous hemodynamics in

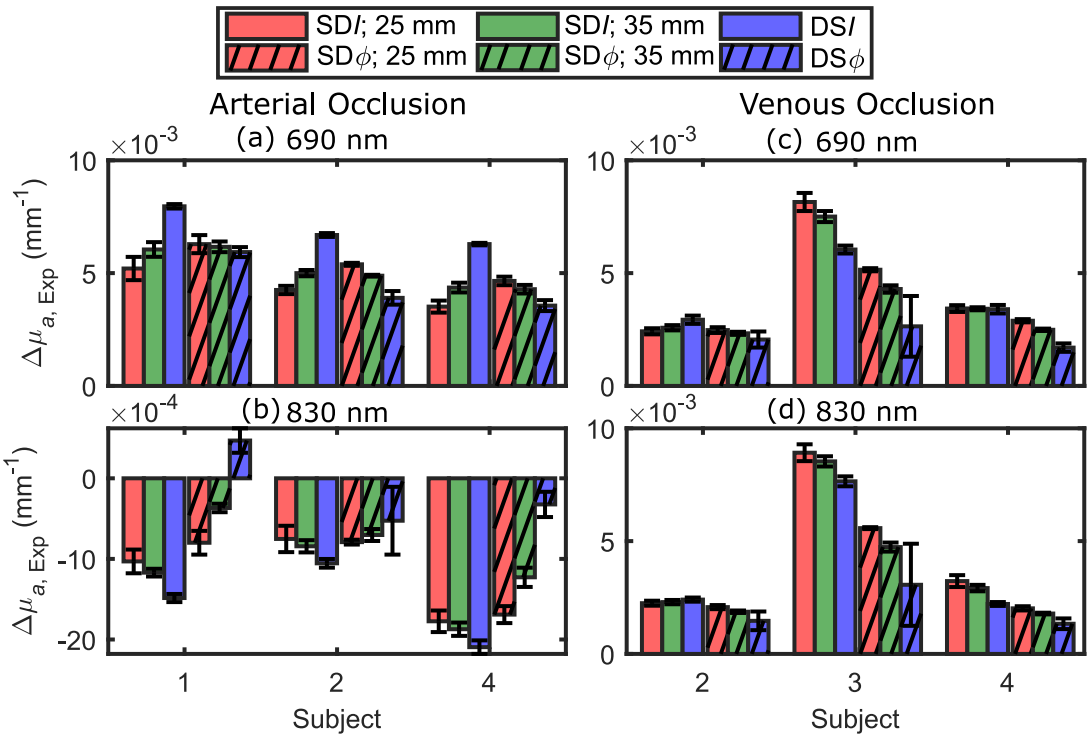

Figure 3.3: Bar plots depicting the maximum measured absorption coefficient change ($\Delta\mu_a$) ($\Delta\mu_{a,\mathrm{Exp}}$) across each subject for an Arterial Occlusion (AO) (a and b) and Venous Occlusion (VO) (c and d) protocols. Across all panels, measurements using phase (ϕ) have a hatched bar, measurements with I have are a solid color, measurements with Single-Distance (SD) at 25 mm are colored in red, measurements with Single-Distance (SD) at 35 mm are in green, and measurements with Dual-Slope (DS) are in blue.

the probed tissue. While Figure 3.2 reports data collected on two representative subjects, Figure 3.3 summarizes results for all subjects, protocols, and wavelengths. Figure 3.3 reports the maximum change in $\Delta\mu_{a,\mathrm{Exp}}$ resulting from the vascular occlusion, as measured by the difference between the average $\Delta\mu_{a,\mathrm{Exp}}$ over the last 10 s of the occlusion and the average $\Delta\mu_a$ at 1 s to 2 s after the onset of occlusion (to account for any absorption shifts from baseline due to artifact occurring at the start of cuff inflation). Error bars in Figure 3.3 represent the propagation of standard deviations of measurements over time (1 s to 2 s after onset of occlusion, last 10 s of occlusion).

While the experimental data have been analyzed under the simplifying assumption that the investigated tissue is spatially homogeneous (with baseline effective optical properties re-

ported in Table 3.1), the layered anatomical structure of the skin, adipose tissue, and skeletal muscle accounts for in-homogeneous baseline optical properties as well as in-homogeneous hemodynamic responses to a vascular occlusions. One may think that, regardless of the baseline optical properties, collecting SD optical data at longer source-detector distances would always increase the sensitivity to hemodynamic changes in deeper tissue layers. In the case of homogeneous semi-infinite media with layered absorption changes, this is usually the case, and we have also shown that the sensitivity to absorption changes in the bottom layer is greater for DSϕ than DSI data [31].

For all three subjects in the AO protocol (Figure 3.3(a) and Figure 3.3(b)) and for subject 2 in the VO protocol (Figure 3.3(c) and Figure 3.3(d)), the maximum absorption changes measured with I data seem to indicate a greater absorption change (in absolute value) deeper in the tissue. In fact, the measured absorption change progressively increases in absolute value when obtained from SDI at 25 mm, SDI at 35 mm, and DSI. However, the opposite is true for ϕ data, in which case the measured absorption change progressively decreases in absolute value when obtained from SDϕ at 25 mm, SDϕ at 35 mm, and DSϕ. This paradoxical result is assigned to non-homogeneous baseline optical properties in combination with non-homogeneous hemodynamic changes in the investigated tissue.

No paradoxical behavior is observed in subjects 3 and 4 in the VO protocol (Figure 3.3(c) and Figure 3.3(d)). The measured values of $\Delta\mu_{a,\mathrm{Exp}}$ with the different data types are consistent with a smaller increase in blood volume in deeper tissue (muscle) vs. superficial tissue (adipose tissue). The measured absorption change progressively decreases when it is obtained from SDI at 35 mm to SDI at 35 mm to DSϕ to SDϕ at 25 mm to SDϕ at 35 mm and lastly to DSϕ. To investigate whether in homogeneous optical properties at baseline and in-homogeneous hemodynamics during vascular occlusion in the superficial adipose tissue and in the deeper skeletal muscle tissue can account for the observed results, we have modeled the tissue as a two-layer medium as presented in subsection 3.3.2.

Oxygen Consumption (OC) and Blood Flow (BF) Obtained from Initial Absorption Change Rates During an Arterial or Venous Occlusion, Respectively

Absorption changes at 690 nm and 830 nm were translated into tissue ΔO and ΔD using their ϵ. Here we consider ΔO and ΔD as the sum of hemoglobin and myoglobin. Tissue OC was obtained from the initial temporal slope of $(\Delta D - \Delta O)/2$ after the start of arterial occlusion. For all subjects, the calculated OC was in the range of $0.95\,\mu\text{mol}\,\text{mL}^{-1}\,\text{min}^{-1}$ to $2.2\,\mu\text{mol}\,\text{mL}^{-1}\,\text{min}^{-1}$. Tissue BF as obtained from the initial temporal slope of Total-hemoglobin concentration change (ΔT) after the start of the VO. The range for calculated BF was $0.48\,\text{mL}\,100\text{mL}^{-1}\,\text{min}^{-1}$ to $4.7\,\text{mL}\,100\text{mL}^{-1}\,\text{min}^{-1}$.

3.3.2 Two-layer Simulation

The simulations based on diffusion theory for a two-layered medium intend to investigate the effect of baseline optical properties and absorption changes in the two layers on the effective absorption changes obtained with different data types.

Effect of Baseline Scattering in the Two-layers

Simulated $\Delta\mu_a$ ($\Delta\mu_{a,\text{Sim}}$) from data generated in a two-layers medium for different values of the top and bottom layer μ_s' ($\mu_{s,\text{top}}'$ and $\mu_{s,\text{bot}}'$, respectively) are shown in Figure 3.4. Specifically, we considered cases of greater μ_s' in the top layer, the same μ_s' in the two layers, and smaller μ_s' in the top layer, according to the x-axis of Figure 3.4. A homogeneous μ_a was considered (top μ_a ($\mu_{a,\text{top}}$) and bottom μ_a ($\mu_{a,\text{bot}}$) were both set to $0.015\,\text{mm}^{-1}$), and the top layer thickness (L_{top}) was set to 5 mm. Furthermore, we examined cases of smaller $\Delta\mu_a$ top layer (Figure 3.4(a)), the same a $\Delta\mu_a$ in the two layers (Figure 3.4(b)), and greater $\Delta\mu_a$ in the top layer (Figure 3.4(c)).

When $\Delta\mu_{a,\text{top}} < \Delta\mu_{a,\text{bot}}$ (Figure 3.4(a)), as $\mu_{s,\text{top}}'/\mu_{s,\text{bot}}'$ decreases to reach a value of 1 and then values less than 1, the effective $\Delta\mu_{a,\text{Sim}}$ obtained with ϕ data increases, whereas the effective ($\Delta\mu_{a,Sim}$ obtained with I data decreases. This shows an increasing sensitivity

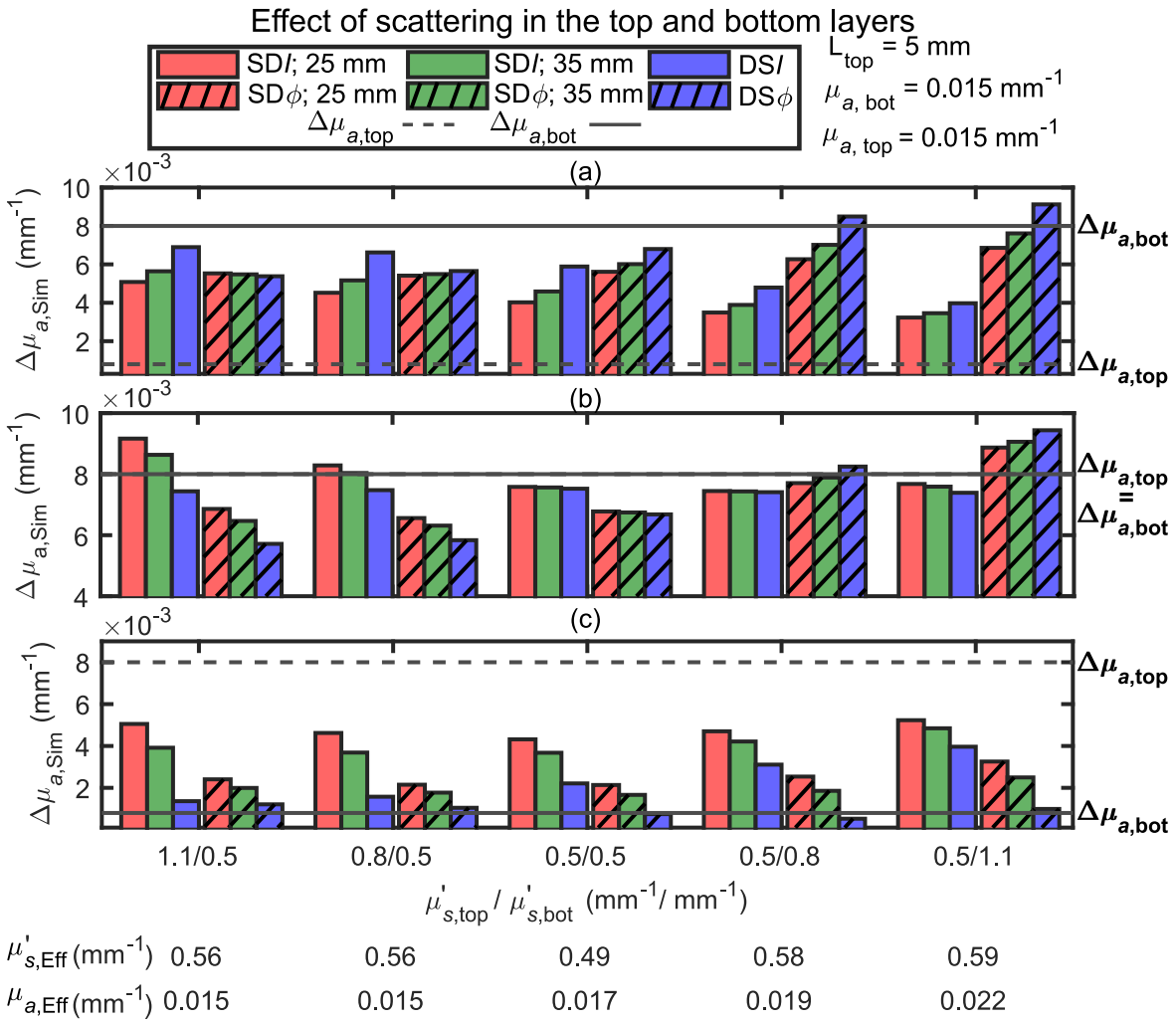

Figure 3.4: Simulated absorption coefficient change ($\Delta\mu_a$) ($\Delta\mu_{a,\mathrm{Sim}}$) obtained with different data types collected on two-layer medium with a different baseline reduced scattering coefficient (μ_s') in the top layer ($\mu_{s\mathrm{top}}'$) and bottom layer ($\mu_{s,\mathrm{bot}}'$). For all simulations, the top layer thickness (L_{top}) was 5 mm, and the absorption coefficient (μ_a) for the top layer ($\mu_{a,\mathrm{top}}$) and bottom layer ($\mu_{a,\mathrm{bot}}$) were both set to $0.015\,\mathrm{mm}^{-1}$. In all panels, measurements using phase (ϕ) data are represented by a hatched bar, measurements using Intensity (I) data by a solid bar, measurements using Single-Distance (SD) at 25 mm are colored in red, measurements using Single-Distance (SD) at 35 mm are in green, and measurements using Dual-Slope (DS) are in blue. The absorption coefficient change ($\Delta\mu_a$) for the top ($\Delta\mu_{a,\mathrm{top}}$) and bottom ($\Delta\mu_{a,\mathrm{bot}}$) layers were simulated for the cases if (a) $\Delta\mu_{a\mathrm{top}}<\Delta\mu_{a,\mathrm{bot}}$ ($\Delta\mu_{a,\mathrm{top}}$=$0.0008\,\mathrm{mm}^{-1}$ $\Delta\mu_{a,\mathrm{bot}}$ = $0.008\,\mathrm{mm}^{-1}$); (b) $\Delta\mu_{a,\mathrm{top}}$=$\Delta\mu_{a,\mathrm{bot}}$ ($\Delta\mu_{a,\mathrm{top}}$ = $\Delta\mu_{a,\mathrm{bot}}$ = $0.008\,\mathrm{mm}^{-1}$); (c) $\Delta\mu_{a,\mathrm{top}}>\Delta\mu_{a,\mathrm{bot}}$ = ($\Delta\mu_{a,\mathrm{top}}$=$0.008\,\mathrm{mm}^{-1}$, $\Delta\mu_{a,\mathrm{bot}}$=$0.0008\,\mathrm{mm}^{-1}$). These values of baseline optical properties and absorption changes were chosen to be consistent with the results of *in-vivo* measurements. The bottom of the horizontal axis label reports the effective homogeneous absorption coefficient (μ_a) ($\mu_{a,\mathrm{Eff}}$) and reduced scattering coefficient (μ_s') ($\mu_{s,\mathrm{Eff}}'$) obtained from the combination of DSI and DSϕ data.

of phase data to the absorption changes in the bottom layer, while intensity data has a decreasing sensitivity as the relationship between $\mu'_{s,\text{top}}$ and $\mu'_{s,\text{bot}}$ vary. When $\Delta\mu_{a,\text{top}} = \Delta\mu_{a,\text{bot}}$ (Figure 3.4(b)), if $\mu'_{s,\text{top}} > \mu'_{s,\text{bot}}$ SDI data overestimate the true $\Delta\mu_a$ while all other data types underestimate the true $\Delta\mu_a$. As the scattering mismatch between the two layers decreases, $\Delta\mu_{a,\text{Sim}}$ obtained with SDI approaches the true $\Delta\mu_a$ and in the homogeneous case, all $\Delta\mu_{a,\text{Sim}}$ are less than the true $\Delta\mu_a$ (as a result of a relatively large $\Delta\mu_a$ and the nonlinear dependence of the various data types on μ_a). As $\mu'_{s,\text{top}}$ becomes smaller than $\mu'_{s,\text{bot}}$, $\Delta\mu_{a,\text{Sim}}$ obtained with ϕ data becomes greater than $\Delta\mu_{a,\text{Sim}}$ obtained with I data. At the smallest value of $\mu'_{s,\text{top}}/\mu'_{s,\text{bot}}$, it is $\Delta\mu_{a,\text{Sim}}$ obtained with phase data that overestimates the true $\Delta\mu_a$. Lastly, when $\Delta\mu_{a,\text{top}} > \Delta\mu_{a,\text{bot}}$ (Figure 3.4(c)), varying the scattering mismatch between the two layers has no major impact, with the most notable effects being a consistently good agreement between $\Delta\mu_{a,\text{Sim}}$ obtained with DSϕ data and $\Delta\mu_{a,\text{bot}}$, and a worsening agreement between ($\Delta\mu_{a,\text{Sim}}$ obtained with DSI data and $\Delta\mu_{a,\text{bot}}$ as the ratio $\mu'_{s,\text{top}}/\mu'_{s,\text{bot}}$ decreases.

Of the cases considered in Figure 3.4, there is only one that reproduces the paradoxical behavior observed *in-vivo* during AO (in all three subjects) and VO (in subject 2): it is the case of $\mu'_{s,\text{top}} > \mu'_{s,\text{bot}}$ and $\Delta\mu_{a,\text{top}} < \Delta\mu_{a,\text{bot}}$ (Figure 3.4(a)). For the VO protocol in subjects 3 and 4, two possible scenarios from the two-layer simulations reproduced the *in-vivo* results. They are (1) $\mu'_{s,\text{top}} > \mu'_{s,\text{bot}}$ and $\Delta\mu_{a,\text{top}} \geq \Delta\mu_{a,\text{bot}}$, and (2) $\mu'_{s,\text{top}} < \mu'_{s,\text{bot}}$ and $\Delta\mu_{a,\text{top}} > \Delta\mu_{a,\text{bot}}$.

As a final comment on the results of Figure 3.4, we note that in the case of a homogeneous medium and a homogeneous absorption change (the set of bars in the center of Figure 3.4(b)), the underestimation of the true $\Delta\mu_a$ by $\Delta\mu_{a,\text{Sim}}$ is due to the non-linear dependence on μ_a of $\ln(\rho^2 I)$, ϕ, and their slope vs. ρ. To mimic the experimental results, in Figure 3.4(b) we have used a relatively large $\Delta\mu_a$ (about 50 % of the background μ_a), which is beyond the linear approximation intrinsic in the DPF and DSF approach. We have verified that by using a much smaller $\Delta\mu_a$ (less than 0.1 % of the background μ_a), $\Delta\mu_{a,\text{Sim}}$ is about equal to the true $\Delta\mu_a$ for all data types.

Effect of Baseline Absorption in the Two-layers

Simulated $\Delta\mu_a$ ($\Delta\mu_{a,\mathrm{Sim}}$) from data generated in a two-layered medium for different values of the top and bottom layer μ_a are shown in Figure 3.5. In this simulation, $\mu'_{s,\mathrm{top}}$=1.1 mm^{-1}, $\mu'_{s,\mathrm{bot}}$=0.5 mm^{-1}, and L_{top}=5 mm. These values of μ'_s in the two layers were chosen as they were most representative of the *in-vivo* results observed in both occlusions protocols, as discussed in relation to Figure 3.4. From Figure 3.5, it is seen that the values of $\mu_{a,\mathrm{top}}$ and $\mu_{a,\mathrm{bot}}$ do not significantly impact the qualitative relationship between the absorption changes obtained with the six data types. In the case $\Delta\mu_{a,\mathrm{top}}>\Delta\mu_{a,\mathrm{bot}}$ (Figure 3.4(c)), it is worth noting that the absorption change obtained with SDI tends to approach the true $\Delta\mu_{a,\mathrm{bot}}$ as $\mu_{a,\mathrm{top}}/\mu_{a,\mathrm{bot}}$ increases

Effect of Top Layer Thickness

Simulated $\Delta\mu_a$ ($\Delta\mu_{a,\mathrm{Sim}}$) from data generated in a two-layered medium for different values of the top layer thickness (in the range 2 mm to 8 mm) are shown in Figure 3.6. In the cases where $\Delta\mu_{a,\mathrm{top}}>\Delta\mu_{a,\mathrm{bot}}$ (Figure 3.6(a)) or $\Delta\mu_{a,\mathrm{top}}<\Delta\mu_{a,\mathrm{bot}}$ (Figure 3.6(c)), as the top layer thickness increases $\Delta\mu_{a,\mathrm{Sim}}$ tends toward $\Delta\mu_{a,\mathrm{top}}$ for every data type. This is an intuitive result, since a thicker superficial layer is expected to result in a greater sensitivity to it. The case where $\Delta\mu_{a,\mathrm{top}} = \Delta\mu_{a,\mathrm{bot}}$ (Figure 3.6(b)) yields less intuitive results in which $\Delta\mu_{a,\mathrm{Sim}}$ obtained with I data show a closer agreement to the true homogeneous $\Delta\mu_a$ than $\Delta\mu_{a,\mathrm{Sim}}$ obtained with ϕ data. This latter result was also observed in the case of $\mu'_{s,\mathrm{top}}/\mu'_{s,\mathrm{bot}} \leq 1$, regardless of the baseline absorption coefficients of the two layers (see Figure 3.4(b) and Figure 3.5(b)).

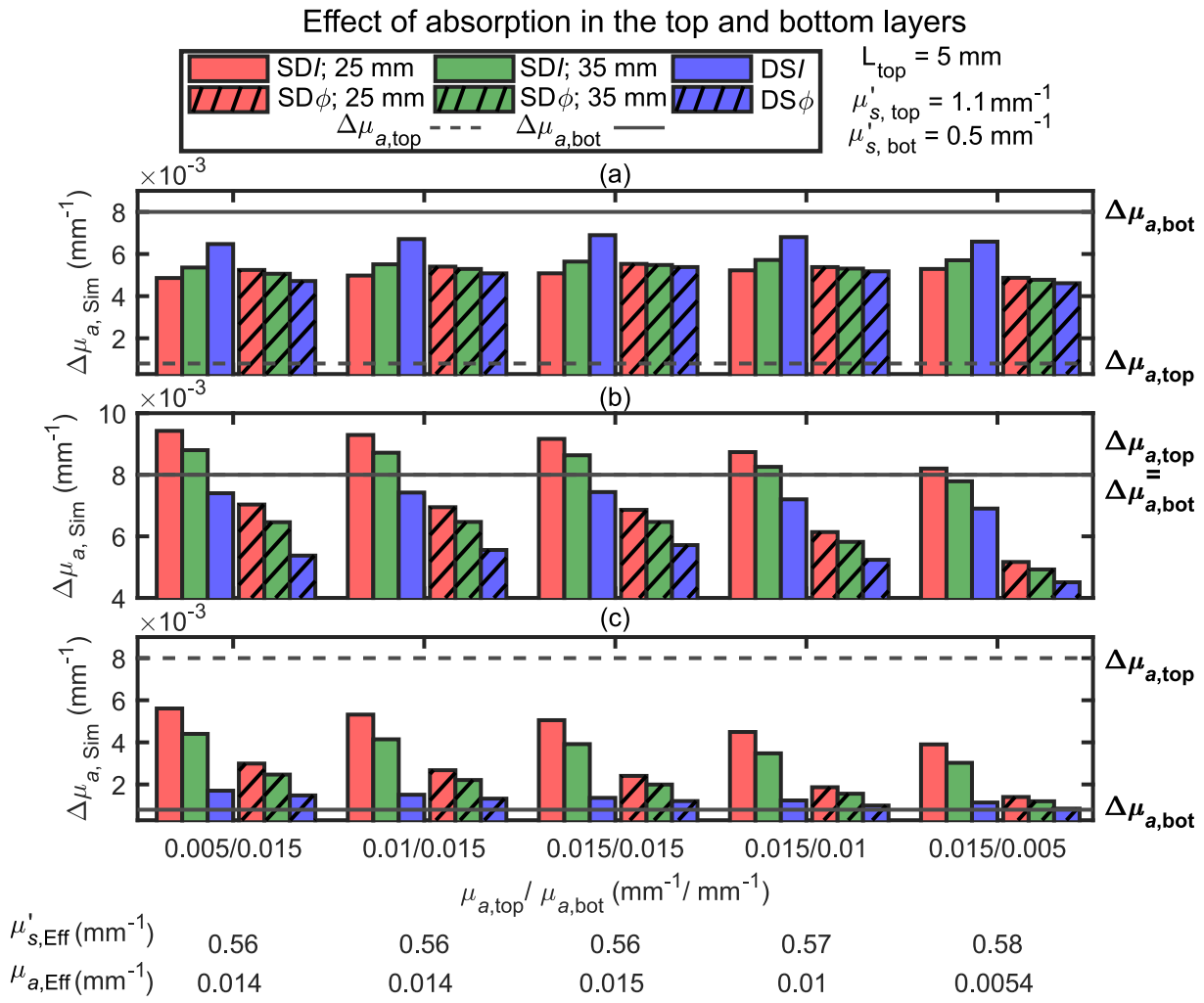

Figure 3.5: Simulated absorption coefficient change ($\Delta\mu_a$) ($\Delta\mu_{a,\mathrm{Sim}}$) obtained with different data types collected on two-layer medium with different baseline absorption coefficient (μ_a) in the top layer ($\mu_{a,\mathrm{top}}$) and bottom layer ($\mu_{a,\mathrm{top}}$). For all simulations, the top layer thickness (L_{top}) was 5 mm, and the reduced scattering coefficient (μ'_s) was set to 1.1 mm^{-1} for the top layer ($\mu'_{s,\mathrm{top}}$) and to 0.5 mm^{-1} for the bottom layer ($\mu'_{s,\mathrm{bot}}$). In all panels, measurements using phase (ϕ) data are represented by a hatched bar, measurements using Intensity (I) data by a solid bar, measurements using Single-Distance (SD) at 25 mm are colored in red, measurements using Single-Distance (SD) at 35 mm are in green, and measurements using Dual-Slope (DS) are in blue. The absorption coefficient change ($\Delta\mu_a$) for the top ($\Delta\mu_{a,\mathrm{top}}$) and bottom ($\Delta\mu_{a,\mathrm{bot}}$) layers were simulated for the cases if (a) $\Delta\mu_{a\mathrm{top}}<\Delta\mu_{a,\mathrm{bot}}$ ($\Delta\mu_{a,\mathrm{top}}$=0.0008 mm^{-1} $\Delta\mu_{a,\mathrm{bot}}$ = 0.008 mm^{-1}); (b) $\Delta\mu_{a,\mathrm{top}}=\Delta\mu_{a,\mathrm{bot}}$ ($\Delta\mu_{a,\mathrm{top}}$ = $\Delta\mu_{a,\mathrm{bot}}$ = 0.008 mm^{-1}); (c) $\Delta\mu_{a,\mathrm{top}}>\Delta\mu_{a,\mathrm{bot}}$ = ($\Delta\mu_{a,\mathrm{top}}$=0.008 mm^{-1}, $\Delta\mu_{a,\mathrm{bot}}$=0.0008 mm^{-1}). These values of baseline optical properties and absorption changes were chosen to be consistent with the results of *in-vivo* measurements. The bottom of the horizontal axis label reports the effective homogeneous absorption coefficient (μ_a) ($\mu_{a,\mathrm{Eff}}$) and reduced scattering coefficient (μ'_s) ($\mu'_{s,\mathrm{Eff}}$) obtained from the combination of DSI and DSϕ data.

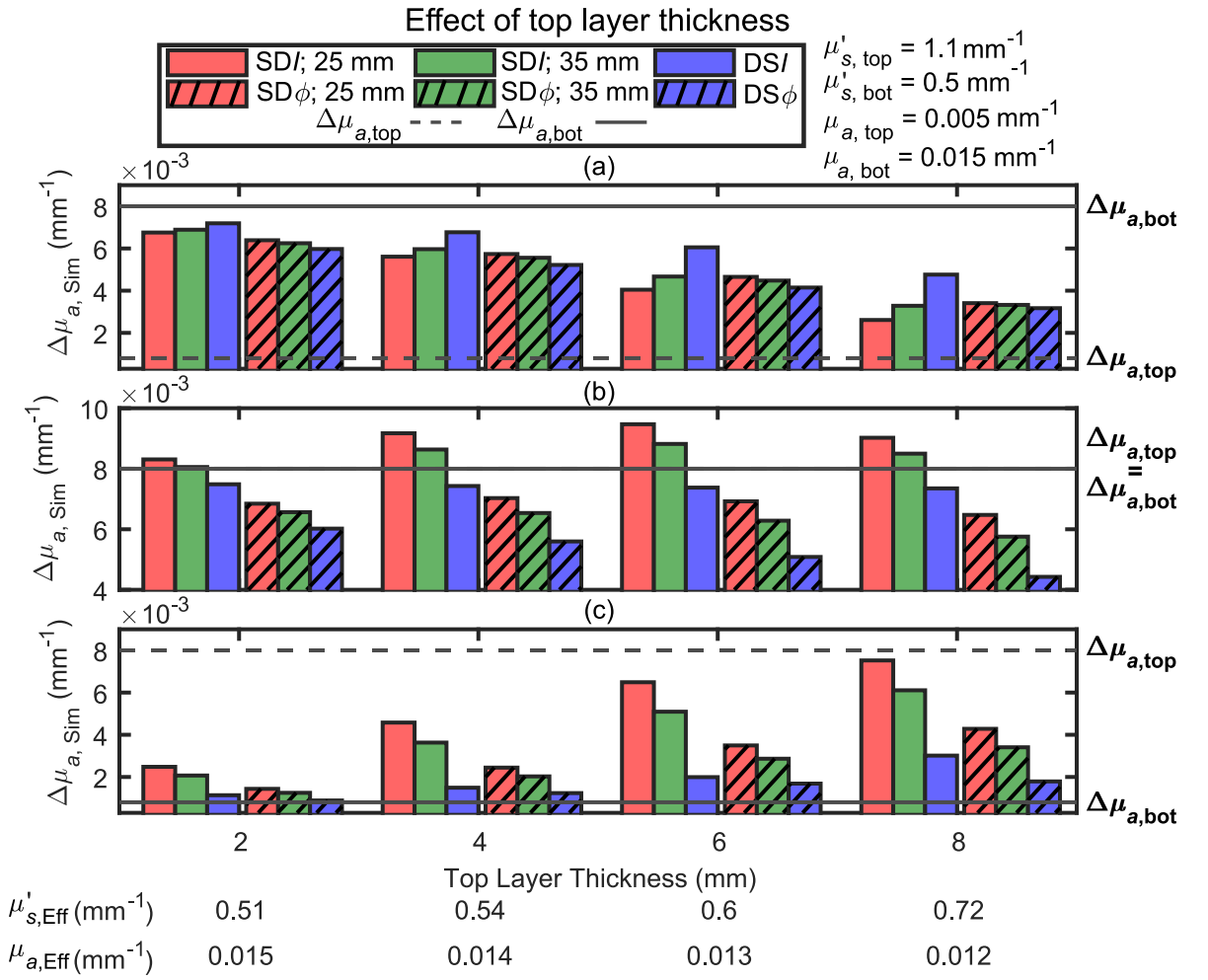

Figure 3.6: Simulated absorption coefficient change ($\Delta\mu_a$) ($\Delta\mu_{a,\mathrm{Sim}}$) obtained with different data types collected on two-layer medium with different values of the top-layer thickness (L_{top}). For all simulations, the absorption coefficient (μ_a) of the top layer ($\mu_{a,\mathrm{top}}$) was set to $0.005\,\mathrm{mm}^{-1}$ and the one of the bottom layer ($\mu_{a,\mathrm{bot}}$) was set to $0.015\,\mathrm{mm}^{-1}$, whereas the reduced scattering coefficient (μ'_s) was set to $1.1\,\mathrm{mm}^{-1}$ for the top layer ($\mu'_{s,\mathrm{top}}$) and to $0.5\,\mathrm{mm}^{-1}$ for the bottom layer ($\mu'_{s,\mathrm{bot}}$). In all panels, measurements using phase (ϕ) data are represented by a hatched bar, measurements using Intensity (I) data by a solid bar, measurements using Single-Distance (SD) at 25 mm are colored in red, measurements using Single-Distance (SD) at 35 mm are in green, and measurements using Dual-Slope (DS) are in blue. The absorption coefficient change ($\Delta\mu_a$) for the top ($\Delta\mu_{a,\mathrm{top}}$) and bottom ($\Delta\mu_{a,\mathrm{bot}}$) layers were simulated for the cases if (a) $\Delta\mu_{a\mathrm{top}}<\Delta\mu_{a,\mathrm{bot}}$ ($\Delta\mu_{a,\mathrm{top}}$=$0.0008\,\mathrm{mm}^{-1}$ $\Delta\mu_{a,\mathrm{bot}}$ = $0.008\,\mathrm{mm}^{-1}$); (b) $\Delta\mu_{a,\mathrm{top}}$=$\Delta\mu_{a,\mathrm{bot}}$ ($\Delta\mu_{a,\mathrm{top}}$ = $\Delta\mu_{a,\mathrm{bot}}$ = $0.008\,\mathrm{mm}^{-1}$); (c) $\Delta\mu_{a,\mathrm{top}}>\Delta\mu_{a,\mathrm{bot}}$ = ($\Delta\mu_{a,\mathrm{top}}$=$0.008\,\mathrm{mm}^{-1}$, $\Delta\mu_{a,\mathrm{bot}}$=$0.0008\,\mathrm{mm}^{-1}$). These values of baseline optical properties and absorption changes were chosen to be consistent with the results of *in-vivo* measurements. The bottom of the horizontal axis label reports the effective homogeneous absorption coefficient (μ_a) ($\mu_{a,\mathrm{Eff}}$) and reduced scattering coefficient (μ'_s) ($\mu'_{s,\mathrm{Eff}}$) obtained from the combination of DSI and DSϕ data.

3.4 Discussion

3.4.1 Baseline *in-vivo* Optical Properties

The effective homogeneous baseline optical properties, measured on the human forearm by a combination of DSI and DSϕ data analyzed with diffusion theory for a semi-infinite homogeneous medium, are reported in Table 3.1 for all subjects and wavelengths (690 nm and 830 nm). The μ_a and μ_s' values are in the range 0.015 mm^{-1} to 0.019 mm^{-1} and 0.48 mm^{-1} to 0.60 mm^{-1}, respectively, across the various subjects. These values agree with optical properties measured non-invasively on human skeletal muscle (specifically, the vastus lateralis) using FD-NIRS [104]. With an assumed 75 % water content, these baseline absorption coefficients at the two wavelengths result in the following range of values for the hemoglobin plus myoglobin related quantities: O: 40 µM to 56 µM; D: 24 µM to 35 µM; T: 69 µM to 82 µM; tissue saturation (StO_2): 55 % to 70 %. These values are also comparable to previous FD-NIRS measurements [21, 105, 106] even though StO_2 values are at the lower end of the range of values typically reported, possibly due to correction for water absorption [113]. In this work, the relevance of baseline effective optical properties is for the determination of $\langle L \rangle_I$ and $\langle L \rangle_\phi$ used to calculated the $\Delta\mu_a$ for SD and DS (section 2.3).

3.4.2 Absorption Changes and Associated Hemodynamics *in-vivo*

The measured absorption changes of the forearm tissue in response to a vascular occlusions vary for different data types (Figure 3.3). Because these absorption changes reflect blood accumulation (during a VO) and blood deoxygenation (during an AO), they are the basis for measurements of muscle BF (using a VO protocol) and muscle OC (using an AO protocol). Even though the experimental $\Delta\mu_a$ values reported in Figure 3.3 are maximum changes during vascular occlusions, whereas BF and OC are obtained from initial rates of change of ΔO and ΔD during vascular occlusion, we found qualitatively similar results for BF and OC obtained with different data types. The range of values observed for rest

BF was $0.48\,\mathrm{mL\,100mL^{-1}\,min^{-1}}$ to $4.7\,\mathrm{mL\,100mL^{-1}\,min^{-1}}$ and $0.95\,\mu\mathrm{mol\,100mL^{-1}\,min^{-1}}$ to $2.2\,\mu\mathrm{mol\,100mL^{-1}\,min^{-1}}$ or $0.02\,\mathrm{mL\,100mL^{-1}\,min^{-1}}$ to $0.05\,\mathrm{mL\,100mL^{-1}\,min^{-1}}$ for rest OC. These values are comparable to those previously reported for muscle BF and muscle OC using NIRS measurements during VO and AO, respectively [20, 21, 56, 60]. The emphasis of this work is on taking advantage of the different values of $\Delta\mu_a$ obtained with the different data types considered here (SDI, SDϕ, DSI, DSϕ) to be able to discriminate the superficial (skin + adipose tissue) and deeper (skeletal muscle) hemodynamics. The goal of this research is to perform hemodynamic measurements that are representative of skeletal muscle considering the fact that adipose tissue and muscle tissue have different baseline optical properties and feature different hemodynamics during external perturbations or physiological processes.

3.4.3 Theoretical Simulations in a Two-layered Medium

We used diffusion theory to simulate data in two-layered medium of known geometrical and optical properties to reproduce key features of experimental data collected on the forearm muscle during vascular occlusion protocols. To make a fair comparison, the same methods for calculating $\Delta\mu_a$ was used on simulated and experimental data. A fundamental approach in these methods was that the $\langle L\rangle$ for I and ϕ used to calculate the DPF and DSF were calculated using the effective homogeneous optical properties. Previous work has studied the dependence of the DPF (obtained from the mean photon time of flight measured with TD-NIRS) on the optical properties and top layer thickness of a two-layered medium [114], but did not study the effect of assuming a homogeneous medium in the calculation of the DPF. To see the impact on our results of obtaining DPF and DPF under the assumption that the tissue is homogeneous, we re-ran the simulations reported in Figure 3.4 using the correct DPF and DSF (i.e., $\langle L\rangle_M$ calculated using the correct optical properties of a two-layered medium). Our most surprising and counter-intuitive result was shown in Figure 3.4(a), where the recovered $\Delta\mu_a$ (found with ϕ data) exhibited opposite dependence on the source-detector distance when $\mu'_{s,\mathrm{top}}>\mu'_{s,\mathrm{bot}}$. Our goal was to explore if one potential reason for this result

was the incorrect assumption of a homogeneous medium in the determination of the DPF and DSF.

For the specific case of Figure 3.4 (a) with $\mu'_{s,\text{top}} = 1.1\,\text{mm}^{-1}$ and $\mu'_{s,\text{bot}} = 0.5\,\text{mm}^{-1}$, Figure 3.7(a) shows simulations using DPF and DSF calculated from the effective homogeneous optical properties (as in Figure 3.4(a)), whereas Figure 3.7(b) shows simulations using DPF and DSF calculated using the correct two-layer medium optical properties. Using the known two-layer optical properties changes the values of $\Delta\mu_a$ obtained with the different data types so that data collected at longer ρs and in the DS configurations result in progressively greater values of $\Delta\mu_a$ for both I and ϕ. This result is consistent with a greater absorption change in the bottom layer for both I and ϕ data types and shows that the use of the effective homogeneous optical properties in calculating the $\langle L \rangle$ is one possible cause of the paradoxical results. Multiple simulations with a mismatch in μ'_s in the two-layers that recreated the paradoxical trend were run utilizing the $\langle L \rangle$ calculated from the two-layer optical properties, all of which showed the reversal of the trend in ϕ. While the use of the two-layer optical properties showed the reversal of the trend between ϕ data types, there is a small difference (approximately 1% to 2%) between the data types that could become insignificant when noise is taken into account.

To further test this result on experimental data, we calculated $\Delta\mu_{a,\text{Exp}}$ for one subject (subject 1) and one wavelength (690 nm) during an AO using the DPF and DSF calculated for the two-layer optical properties that best matched the experimental data (used in Figure 3.7(b)). The $\langle L \rangle$ values derived for I ($\langle L \rangle_I$) and ϕ ($\langle L \rangle_\phi$) assuming homogeneous and two-layered optical properties are reported in Table 3.2. Using the DPF and DSF for a homogeneous medium results in values of $\Delta\mu_{a,\text{Exp}}$ (reported in Figure 3.7(c)) that follow the same trend as those in Figure 3.3(a). Using the DPF and DSF for a two-layered medium modifies the values of $\Delta\mu_{a,\text{Exp}}$ (as reported in Figure 3.7(d)) similarly to the simulation in Figure 3.7(b)). While there is a reversal of the trend across data types for ϕ using the $\langle L \rangle$ using the two-layer optical properties, all are within the reported error showing no apparent

difference between the calculated $\Delta\mu_{a,\mathrm{Exp}}$. In this particular case, changing the method of calculating $\langle L \rangle$ changed the average behavior. This could potentially be due to other factors affecting this relationship that are not the $\langle L \rangle$ and an incorrect guess in the optical properties. This specific example is reported to show the potential of the incorrect $\langle L \rangle$ affecting the relationship between data types, and applying this technique to the other subjects did not show a reversal in the $\Delta\mu_{a,\mathrm{Exp}}$ calculated with ϕ data types.

In the absence of knowledge of the optical properties of the top and bottom layer, the assumption of a homogeneous medium to calculate the DPF and DSF was required. Several studies, particularly in CW-NIRS, have assumed a wavelength-independent DPF [20, 35, 72] taken from the literature, which will introduce errors in the measured values of $\Delta\mu_a$ and in their wavelength dependence.

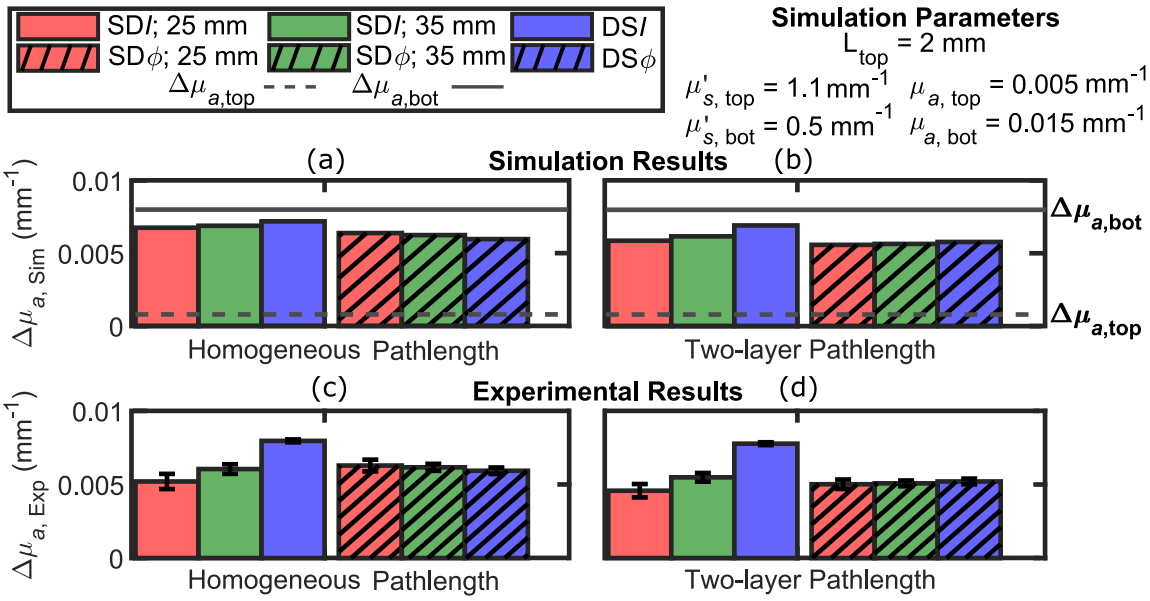

Figure 3.7: Comparison of absorption coefficient change ($\Delta\mu_a$) obtained from a total optical path-length ($\langle L \rangle$) assuming either a homogeneous medium (panels (a) and (c)) or a two-layer medium (panels (b) and (d)) in simulations ($\Delta\mu_{a,\mathrm{Sim}}$) (panels (a) and (b)) and in experiments *in-vivo* ($\Delta\mu_{a,\mathrm{Exp}}$) (panels (c) and (d)) on Subject 1 at 690 nm during arterial occlusion. For all simulations, the top layer thickness (L_{top}) was 2 mm, the absorption coefficient (μ_a) in the top layer ($\mu_{a,\mathrm{top}}$) was 0.005 mm^{-1} and the bottom layer ($\mu_{a,\mathrm{bot}}$) was 0.015 mm^{-1}, the reduced scattering coefficient (μ'_s) for the top layer ($\mu'_{s,\mathrm{top}}$) was 1.1 mm^{-1} and the bottom layer ($\mu'_{s,\mathrm{bot}}$) was 0.5 mm^{-1}.

Table 3.2: Total optical path-length ($\langle L \rangle$) for Intensity (I) ($\langle L \rangle_I$) and phase (ϕ) ($\langle L \rangle_\phi$) at 690 nm using either a homogeneous medium with optical properties calculated from experimental data, or a two-layer medium. For the two-layer medium, the top layer thickness (L_{top}) was 2 mm, the absorption coefficient (μ_a) in the top layer ($\mu_{a,\text{top}}$) was 0.005 mm^{-1} and in the bottom layer ($\mu_{a,\text{bot}}$) was 0.015 mm^{-1}, the reduced scattering coefficient (μ'_s) for the top layer ($\mu'_{s,\text{top}}$) was 1.1 mm^{-1} and the bottom layer ($\mu'_{s,\text{bot}}$) was 0.5 mm^{-1}. Here, the source-detector distance (ρ) are 25 mm (ρ_1) and 35 mm (ρ_2).

Sub 1 at 690 nm	$\langle L \rangle_I$(mm)		$\langle L \rangle_\phi$(mm)	
	ρ_1	ρ_2	ρ_1	ρ_2
Homogeneous Medium	106	153	10.3	15.6
2-layer Medium	121	168	12.9	19.8

Acronyms: generalized optical path-length for intensity ($\langle L \rangle_I$), generalized optical path-length for phase ($\langle L \rangle_\phi$), source-detector distance (ρ)

3.4.4 Limitations of Modeling Based on a Two-layered Medium

Modeling tissue as a two-layered medium assumes lateral homogeneity. Lateral inhomogeneities in tissue optical properties and in tissue hemodynamics under the optical probe can arise for several reasons, including physiological/anatomical differences or uneven contact pressure between the probe and tissue. Spatial mapping of skeletal muscle has shown variability across muscle regions [56, 104, 115]. The data sets for this study resulted in similar $\Delta\mu_{a,\text{Exp}}$ for the two SDs at the same distance but on opposite sides on the probe (Figure 3.1(c)), which supports the assumption of lateral homogeneity. However, in the presence of lateral heterogeneity in the tissue optical properties, tissue hemodynamics, and/or probe-tissue contact pressure, the assumption of lateral homogeneity intrinsic in the two-layered model may lead to incorrect results. Special care must be taken in applying the optical probe with even pressure on the muscle tissue, and the lateral homogeneity of the measured hemodynamics should be verified before applying the methods presented here.

3.4.5 Implications of This Study for Optical Measurements of Muscle Hemodynamics

Comparison between the experimental results *in-vivo* for the various data types (Figure 3.3) and the simulations on two-layered medium (Figure 3.4, Figure 3.5, and Figure 3.6) lead to the following conclusions for the baseline optical properties and the absorption changes in the top and bottom tissue layers:

1. In the case of an AO, $\mu'_{s,\text{top}} > \mu'_{s,\text{bot}}$ and $|\Delta\mu_{a,\text{top}}| < |\Delta\mu_{a,\text{bot}}|$ (see Figure 3.4), and $\mu_{a,\text{top}} \leq \mu_{a,\text{bot}}$ (see Figure 3.5(a)). These results for baseline optical properties are consistent with the higher scattering and lower absorption previously reported for adipose tissue vs. muscle tissue [103, 116, 117]. The lower absorption change in the top (adipose) layer, vs. the bottom, (muscle) layer during arterial occlusion implies a lower OC in adipose vs. muscle tissue at rest, which has previously been reported [20, 103, 110, 118].

2. In the case of venous occlusion, the *in-vivo* results in subject 2 are in line with the AO results above, whereas in subjects 3 and 4 they are consistent with either of these two scenarios: (1) $\mu'_{s,\text{top}} > \mu'_{s,\text{bot}}$ and $\Delta\mu_{a,\text{top}} \geq \Delta\mu_{a,\text{bot}}$ (see Figure 3.4(b) and Figure 3.4(c)), or (2) $\mu'_{s,\text{top}} < \mu'_{s,\text{bot}}$ and $\Delta\mu_{a,\text{top}} > \Delta\mu_{a,\text{bot}}$ (Figure 3.4(c)). For consistency with the baseline optical properties observed in the arterial occlusion case, scenario (1) is the selected one. The greater or comparable absorption change in the top (adipose) layer, vs. the bottom (muscle) layer, during venous occlusion implies a greater or comparable blood flow in adipose vs. muscle tissue at rest. This result is in line with a previous study that reported a constant (or slightly increasing) measured BF with NIRS as a function of adipose layer thickness [20].

3. The top layer thickness in the range 2 mm to 8 mm (Figure 3.6) significantly impacted the magnitude of $\Delta\mu_a$ obtained using different data types, but only marginally impacted their relative values.

The results presented here demonstrate the different impact of baseline optical properties and absorption changes of a two-layered medium on the various data types measured with FD-NIRS in a dual-slope configuration of sources and detectors on the tissue surface. Therefore, these results suggest the feasibility of discriminating baseline optical properties and hemoglobin concentration changes in adipose and muscle tissue by fitting measured and simulated $\Delta\mu_a$ obtained with the various data types.

3.5 Conclusions

The objective of this work is to explore the feasibility of discriminating superficial and deep tissue hemodynamics by performing non-invasive optical measurements with rich temporal and spatial information content. FD-NIRS is used to collect the amplitude (or intensity (I)) and the phase (ϕ) of photon-density waves injected into the tissue by intensity-modulated illumination. Multiple (two in this work) source-detector separations are used to collect data (I and ϕ) that achieve different penetration depths into tissue. A special, symmetrical arrangement of two sources and two detectors is used to perform self-calibrating measurements of baseline optical properties, and robust measurements of absorption changes that are largely insensitive to instrumental drifts and motion artifacts. This work shows that the data types (I and ϕ) and geometrical arrangements of data collection (Single-Distance (SD), Dual-Slope (DS)) result in a set of measurements with a strong dependence on the baseline optical properties and absorption changes in 2-layered medium. This can be the basis for discriminating absorption dynamics in superficial and deep tissue by collecting data that are analyzed under the assumption of tissue homogeneity and fitting them using data generated with a two-layer tissue model that is analyzed the same a homogeneous tissue model used on experimental data. In the case of muscle measurements, the thickness of the top layer (adipose tissue) can be measured with a skin-fold caliper or ultrasound. It is also possible to further expand the data space beyond what was done in this work, by introducing multiple

DS sets of sources and detectors that feature multiple pairs of source-detector distances.

The approach proposed here is an alternative method to one in which the collected data are directly analyzed using a two-layer tissue model, as already proposed for studies in muscle [103, 107, 111] and brain [29, 119, 120]. This latter method, however, may be less robust and require an even greater data space (in the temporal and spatial domains) than the one proposed here. Future research will explore practical implementations of the method proposed in this work in comparison with a full-fledged two-layer tissue model for the hemodynamic characterization of layered tissue. This is a significant objective for non-invasive optical studies of biological tissue, with direct implications for skeletal muscle studies as well as human brain studies.

3.6 Acknowledgments and Contributions

Authors who contributed to this work are Cristianne Fernandez, Giles Blaney, Jodee Frias, Fatemeh Tavakoli, Angelo Sassaroli, and Sergio Fantini. All are with the Department of Biomedical Engineering at Tufts University. I would like ot thank Jodee Frias and Fatemeh Tavakoli for assisting with data collection and Giles Blaney and Angelo Sassaroli for the implementation of the two-layer model.

Chapter 4

Dual-Slope Imaging of Coherent Cerebral Hemodynamics

4.1 Introduction

This chapter switches gears from the application of skeletal muscle to that of cerebral hemodynamics. Here, we will investigate the application of the Dual-Slope (DS) in limiting the effect of extra cerebral tissue to obtain measurements more representative of the brain.

Diffuse Optical Imaging (DOI) using functional Near-InfraRed Spectroscopy (fNIRS) has been demonstrated in both behavior and social studies [45] as well as clinical applications [40] on the brain. fNIRS has the ability to spatially map brain hemodynamics and activation in specific cortical regions while being non-invasive, portable, and low-cost especially when comparing the latter two advantages to functional Magnetic Resonance Imaging (fMRI) [12]. These advantages allow for real time continuous monitoring of the brain at the bedside in the clinical setting and in real-life scenarios. However, implementations of fNIRS and DOI struggle due to their significant sensitivity to superficial, extracerebral tissue [6, 9, 29, 48]. Most techniques still preferentially measure scalp and skull hemodynamics with only a weak contribution from the brain itself. Therefore, the field has continually investigated methods

that seek to identify or suppress this superficial signal, and allow for more specific brain measurements [6, 27–29, 31, 121].

Typical implementations of DOI utilize Continuous-Wave (CW) despite the fact that these measurement are the most strongly affected by superficial hemodynamics. In Frequency-Domain (FD) [32] or Time-Domain (TD) [34] techniques, the phase (ϕ) or higher moments of the photon time-of-flight distribution, respectively, intrinsically provide measurements that are more specific to deeper tissue [31, 33, 47]. Despite this, a majority of the aforementioned techniques to determine the brain's contribution to the signal are targeted toward CW data and include measurements that are specifically sensitive to superficial hemodynamics [6, 27–29]. A recent push in the field has focused on the implementation of FD for the use of ϕ data and TD techniques with the information from higher moments.

Single-Distance (SD) measurements, defined as measurements between one source and one detector (described in subsection 2.3.2), are commonly utilized in DOI. Since SD measurements are largely sensitive to superficial tissue, the use of multiple SDs has been implemented [6, 12, 27–29, 47, 121] but is still unclear which set of source-detector distances will optimally reconstruct deeper hemodynamics. This work utilizes the DS (described in subsection 2.3.3), which is a configuration of two sources and two detectors which realize symmetric measurements of two slopes of optical data versus source-detector distance (ρ) [44, 99]. These slopes are averaged to achieve DS measurements that feature a sensitivity selective to deeper tissue [30, 31, 44] and also suppress artifacts from changes in the probe-tissue coupling or from instrumental drifts (inherited from the Self-Calibrating (SC) method) [43, 122].

Coherent Hemodynamics Spectroscopy (CHS) is a method based on dynamic measurements of cerebral hemodynamics (namely the Oxy-hemoglobin concentration change (ΔO) and Deoxy-hemoglobin concentration change (ΔD)) that are coherent with a driving physiological process, for example oscillations in Arterial Blood Pressure (ABP) [91]. Transfer function analysis between ΔO and ΔD oscillations coherent with ABP give insights into

the relative dynamics of Blood Flow (BF) and Blood Volume (BV) oscillations. Transfer function analysis between cerebral hemodynamics and ABP using Transcranial Doppler ultrasound (TCD) [16, 88–90] and Near-InfraRed Spectroscopy (NIRS) [19, 123] have shown that their phase relationship can give indications about impaired autoregulation. Measured NIRS cerebral hemodynamics are a combination of BF and BV (as well as oxygen consumption) changes occurring in superficial tissue (i.e., scalp) and deep tissue (i.e., brain), leading to a need for a method to preferentially measure BF changes in the brain to assess cerebral autoregulation. CHS has been applied utilizing one DS set and has shown a stronger relative contribution of BF driven changes attributed to the brain [31]. The combination of DOI and CHS applied to the human brain has the potential to provide spatial information relating cerebral autoregulation over a brain region, and when applied with DS, preferentially reconstruct deeper cerebral hemodynamics [13].

This chapter will use DS DOI with FDNIRS during a CHS protocol and demonstrate the ability of this method to achieve a preferential sensitivity to the brain in comparison to the dominant sensitivity to extra cerebral, superficial tissue featured by traditional Single-Distance Intensity (SDI) measurements. This will be achieved by applying a large imaging array on one subject and a modular hexagonal array to a total of 3 subjects where a comparison of reconstructed images with different data-types (i.e., SD and DS with either Intensity (I) or ϕ).

4.2 Methods

4.2.1 Study Protocol and Data Acquisition

FD NIRS measurements were performed during systemic ABP oscillations using either a large imaging array or two hexagonal array probes (described in section 4.2.1). All FD NIRS measurements were performed using an ISS Imagent V2 [Champaign, IL USA] which utilizes two optical wavelengths (λs) (830 nm and 690 nm) and a modulation frequency (f_{mod})

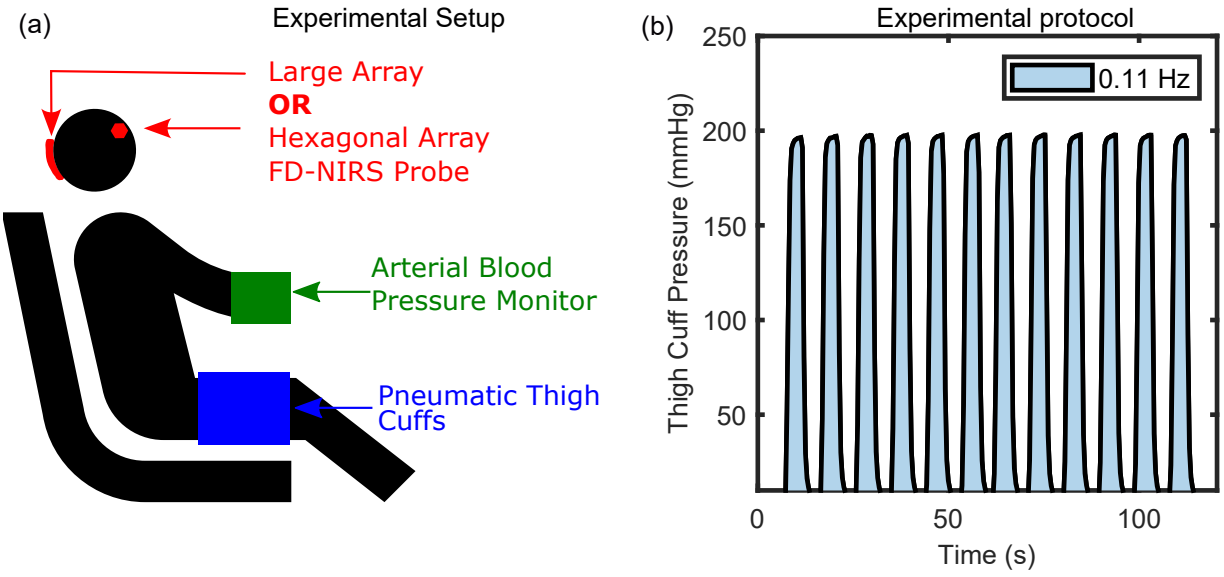

Figure 4.1: (a) Depiction of the experimental set up used to induce Arterial Blood Pressure (ABP) oscillations. Each participant was in a seated position with either a large imaging array or two hexagonal arrays placed on the head to take Frequency-Domain (FD)-Near-InfraRed Spectroscopy (NIRS) measurements. Two pneumatic thigh cuffs were placed around the subject's thighs and an ABP monitor was placed on the subject's left arm. (b) A systemic blood pressure oscillations protocol was performed, where oscillations lasted for 3 min and the pneumatic cuff pressure was set to 200 mmHg.

of 140.625 MHz. Systemic ABP oscillations were induced at a frequency of 0.11 Hz using a cuff secured on the upper portion of each of the subject's thighs. The dimensions of each cuff were 180 mm $\times$ 1080 mm when laid flat. The cuffs were placed so that they were centered on the thighs and secured not to shift during the inflation and deflation procedures. The amplitude of the cuff pressure oscillations was set to 200 mmHg (Figure 4.1(b)) and were measured continuously with a Series 626 Pressure Transmitter Dwyer Instruments Inc [Michigan City, IN USA] (digital manometer). Continuous ABP measurements were taken throughout the experiment using an NIPD100D BIOPAC Systems [Goleta, CA USA] (beat-to-beat finger plethysmography system). Figure 4.1(a) shows an example of the experimental setup. Experiments with both imaging arrays followed the same protocol. The experimental protocol started with a 1 min baseline that was used to find baseline tissue optical properties (absorption coefficient (μ_a) and reduced scattering coefficient (μ_s'); section 4.2.2). Following

the initial baseline, the oscillation sequence began and lasted 3 min, leading to 19 oscillation periods at the set frequency of 0.11 Hz.

Large Imaging Array

One healthy human subject (28 yr old male) participated in a Tufts University Institutional Review Board (IRB) approved study that utilized the large imaging array. The large imaging array was placed on the back of the subject's head so that the upper part of the array was over the *occipital* lobe and consisted of 57 SD sets and 30 DS sets. The array had an overall triangular shape and covered an area of approximately 120 mm on a side (about 7200 mm^2). All of the DS ρs pairs were approximately 25 mm and 37 mm. A schematic of the large imaging array is shown in Figure 4.2(a). Construction and design of the large imaging array was done previous to this work by another lab member and is described in Blaney *et al* (2020) [99].

Hexagonal Arrays

A total of 3 subjects (1 Male, 2 Female: Age range 25 yr to 29 yr) participated in a Tufts University IRB approved study that utilized 2 modular hexagonal imaging arrays placed on the forehead on each side of the midline above the eyebrows. Each hexagonal array consisted of 2 detectors and 2 sources with source detector separations of 25 mm and 37 mm. This led to 2 SD pairs at 25 mm, 2 SD pairs at 37 mm, and 4 DS sets. Referring to source and detector names in Figure 4.2(b), the side lengths are 16.7 mm for sides 12 and 34 and 25 mm for sides 1A, 4A, 2B, and 3A.

Construction of the hexagonal array modules utilized here was specifically done so that the source fibers could be easily detached. After the design of the hexagonal probe, a mesh made of Ultra High Molecular Weight polyethylene (UHMW) was cut with holes for the sources and detectors, along with small holes around the center of the mesh. These small holes allow the mold material to pass through, as the mesh will be in the center. To allow for

easy connection of the source fibers, a SMA bulkhead adapters was utilized as it allowed fibers to be easy screwed in. The adapter was placed at the source locations, and the two lock nuts were utilized to secure the adapter to the mesh. Next, epoxy was used to secure the detector fibers and source adapters to the mesh. Lastly, liquid urethane rubber was poured into the mold and left to harden. This process was completed for each modular hexagonal probe. The distance between the two optical probes was set to approximately 30 mm (between detectors B and C) utilizing a specially cut velcro that holds the two optical probes and secures them around the head.

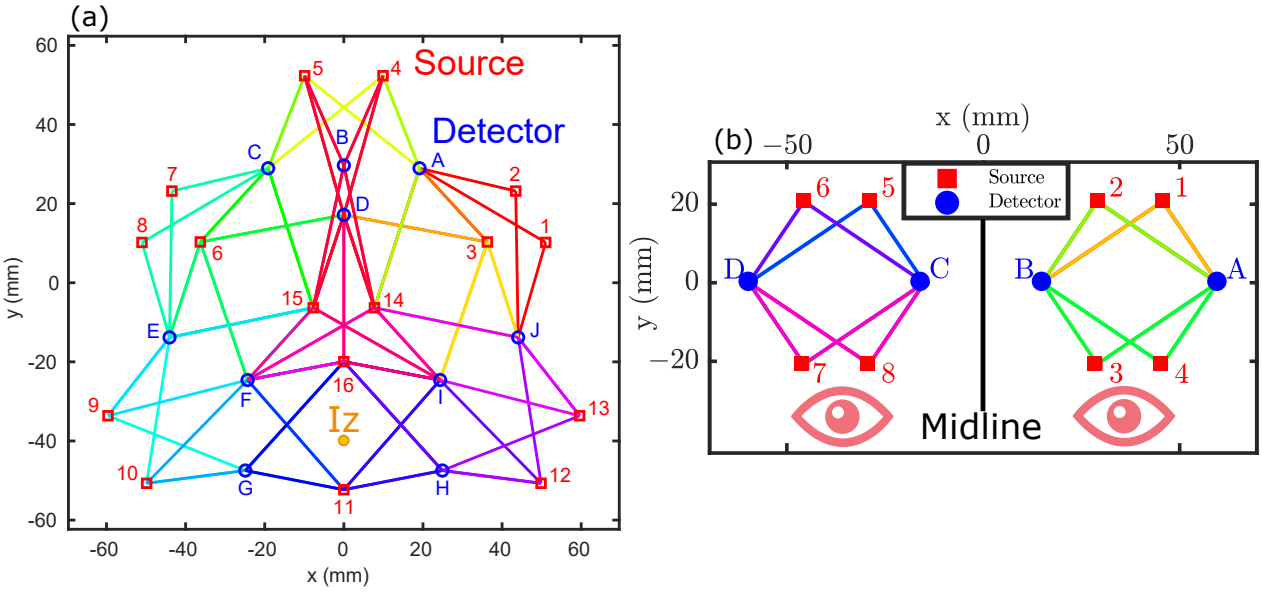

Figure 4.2: (a)Schematic of the large imaging array where lines of differing colors show different DS sets. The approximate *Inion* (Iz) location is shown in yellow. The subject's Iz to *Nasion* (Nz) distance was 365 mm. (b) Schematic of the two hexagonal modular arrays used where lines of differing colors show different DS sets. The probes were placed on the forehead above the eyebrows so that the center of each probe was above the eye. The distance between detectors B and C was approximately 30 mm.

Skull Thickness Measurements

Ultrasound measurements were taken on the region of the forehead in which the hexagonal probe was places. These measurements were taken with an SonoSite S-Nerve FU-

JIFILM SonoSite Inc [Bothell, WA USA] (ultrasound system) system equipped with a multi-frequency, broadband, 50 mm linear array transducer probe (HFL50x, frequency range: 6 MHz to 15 MHz). Measurements with the ultrasound system were taken longitudinally on both the left and right sides of the forehead, where the center of the transducer was placed approximately at the center of the probe location. These images were then analyzed to retrieve approximate skull thickness for the regions under the upper and lower portions of modular hexagonal probes.

4.2.2 Near-InfraRed Spectroscopy Signal Processing

Absolute Optical Property Recovery

Tissue absolute μ_a and μ_s' were calculated for each DS set by using the DS set in SC FD-NIRS mode. To convert the FD slopes to μ_a and μ_s', an iterative method based on a semi-infinite homogeneous medium and extrapolated boundary conditions was used. Briefly, this method uses the complex Reflectance ($\widetilde{R}$) versus ρ and an initial guess of the complex effective attenuation coefficient ($\widetilde{\mu}_{eff}$) using assumptions of linearity to find μ_a and μ_s' by iteratively solving the analytical equation for $\widetilde{R}$ in a semi-infinite homogeneous medium. The iteratively recovered $\widetilde{\mu}_{eff}$ was then converted to μ_a and μ_s' for each DS set.

Changes in Hemoglobin Concentration

Dynamic changes in I or ϕ for SD or DS were translated into absorption coefficient change ($\Delta\mu_a$) using methods described in section 2.3 using the absolute optical properties recovered (as described in section 4.2).

4.2.3 Phasor Analysis

Transfer function analysis was performed during the period of systemic ABP oscillations. All processing described here was done for each array, SD pair, DS set, and data type (I

or ϕ) independently. The analysis was done to retrieve a phasor ratio vector between Oxy-hemoglobin and Arterial blood pressure ($\widetilde{O}/\widetilde{ABP}$) and a phasor ratio vector between Deoxy-hemoglobin and Arterial blood pressure ($\widetilde{D}/\widetilde{ABP}$) at the induced frequency of 0.11 Hz. These vectors represented the amplitude ratio and the phase difference of the two signals considered. First, the Continuous Wavelet Transform (CWT), based on a complex Morlet mother wavelet, was taken of the temporal signals ΔO, ΔD, and ABP during the oscillation period. This step gave phasor maps of the Oxy-hemoglobin phasor ($\widetilde{O}$), Deoxy-hemoglobin phasor ($\widetilde{D}$), and Arterial blood pressure phasor ($\widetilde{ABP}$) over time (t) and frequency (f). Then the phasors maps were divided to obtain the phasor vector ratio maps of the transfer functions $\widetilde{O}/\widetilde{ABP}$ and $\widetilde{D}/\widetilde{ABP}$ over t and f.

To identify which t and f regions to use in further analysis, the wavelet Coherence between the Oxy-hemoglobin and Arterial blood pressure phasors ($COH(\widetilde{O}, \widetilde{ABP})$) and the Coherence between the Deoxy-hemoglobin and Arterial blood pressure phasors ($COH(\widetilde{D}, \widetilde{ABP})$) were calculated using a modified version of the MATLAB wcoherence function, which removes smoothing in frequency. A Coherence (COH) threshold generated from the 95^{th} percentile ($\alpha = 0.05$) of COH between random surrogate data was used to mask both $COH(\widetilde{O}, \widetilde{ABP})$ and $COH(\widetilde{D}, \widetilde{ABP})$ maps so that only ts and fs with significant coherence between the considered signals contained Boolean *true*. Next, a logical AND was taken between both threshold-ed $COH(\widetilde{O}, \widetilde{ABP})$ and $COH(\widetilde{D}, \widetilde{ABP})$ Boolean maps so that only ts and fs in which both ΔO and ΔD were coherent with ABP retained *true* Boolean values. This map of significant COH was then used to mask the $\widetilde{O}/\widetilde{ABP}$ and $\widetilde{D}/\widetilde{ABP}$ transfer function maps, allowing only transfer function relationships of significant coherence between both ΔO and ABP as well as ΔD and ABP to be considered in the analysis.

4.2.4 Image Reconstruction

Image reconstruction was performed using the Moore-Penrose inverse (MP) with Tikhonov regularization (scaling parameter $a = 1$). Here, image reconstruction was done for each

data-type (I or ϕ) and source-detector configuration (SD or DS) independently so that comparisons can be made between them. Firstly, $\widetilde{O}/\widetilde{ABP}$ and $\widetilde{D}/\widetilde{ABP}$ were translated into a phasor ratio vector between the absorption coefficient and Arterial blood pressure ($\widetilde{\mu_a}/\widetilde{ABP}$) using Beer's law [124] implemented in the image reconstruction. For the image reconstruction the following forward model was used:

$$\overrightarrow{\widetilde{\mu_a}/\widetilde{ABP}}^{(meas)} = \boldsymbol{\mathcal{S}}\overrightarrow{\widetilde{\mu_a}/\widetilde{ABP}}^{(true)} \tag{4.1}$$

where $\widetilde{\mu_a}/\widetilde{ABP}^{(meas)}$ is a kx1 vector of measured phasor ratio vector between the absorption coefficient and Arterial blood pressure ($\widetilde{\mu_a}/\widetilde{ABP}$), $\boldsymbol{\mathcal{S}}$ is a kxn matrix of sensitivities (where n is the number of voxels considered) and $\overrightarrow{\widetilde{\mu_a}/\widetilde{ABP}}^{(true)}$ is a nx1 vector of true voxel $\widetilde{\mu_a}/\widetilde{ABP}$. To solve Equation 4.1, the MP was with Tikhonov regularization formulated as:

$$\begin{aligned}\overrightarrow{\widetilde{\mu_a}/\widetilde{ABP}}^{(recon)} &= \boldsymbol{\mathcal{S}}^{+}\overrightarrow{\widetilde{\mu_a}/\widetilde{ABP}}^{(Actual)} \\ \boldsymbol{\mathcal{S}}^{+} &= \boldsymbol{\mathcal{S}}^{T}(\boldsymbol{\mathcal{S}}\boldsymbol{\mathcal{S}}^{T} + \alpha\mathbf{I})^{-1} \\ \alpha &= a \times \max(diag(\boldsymbol{\mathcal{S}}\boldsymbol{\mathcal{S}}^{T}))\end{aligned} \tag{4.2}$$

where $\overrightarrow{\widetilde{\mu_a}/\widetilde{ABP}}^{(recon)}$ is the vector of the reconstructed voxel absorption changes, and $\mathbf{I}$ is the identity matrix. The matrix of sensitivity to an absorption change ($\boldsymbol{\mathcal{S}}$) was generated considering a semi-infinite homogeneous medium (using methods described in section 2.4) [99] and the local DS measured optical properties (also used for calculation of Differential Path-length Factor (DPF) or Differential Slope Factor (DSF)). Only pairs that passed the data evaluation were considered in the $\boldsymbol{\mathcal{S}}$. The medium was voxelized using two layers of pillars (voxels in z depth) with a lateral pitch of 1 mm (along x and y) and an axial size (along z) of 5 mm for the top-layer and 25 mm for the bottom-layer. The images reported here represent reconstructed values of the bottom-layer voxels in the $x-y$ plane. This method for voxelizing the medium was used before for DS imaging in Blaney *et al* (2020) [99] & Blaney

et al (2020) [125]. Spatial maps of $\widetilde{\mu_a}/\widetilde{ABP}$ at the two λ were then converted to maps of $\widetilde{O}/\widetilde{ABP}$ and $\widetilde{D}/\widetilde{ABP}$, again using Beer's law [124]. Finally, maps of the phasor ratio vector between Deoxy-hemoglobin and Oxy-hemoglobin ($\widetilde{D}/\widetilde{O}$) were created using the ratio of $\widetilde{O}/\widetilde{ABP}$ and $\widetilde{D}/\widetilde{ABP}$, and maps of the phasor ratio vector between Total-hemoglobin and Arterial blood pressure ($\widetilde{T}/\widetilde{ABP}$) was found using their sum. These maps of complex numbers were then smoothed using a Gaussian filter with a characteristic length equal to the average array resolution [99] to remove artifacts created by applying MP to complex numbers.

4.2.5 Data Evaluation

Data quality evaluation was conducted so that only sufficiently good-quality data were used for further analysis and image reconstruction. This is especially important, as any set that did not pass the quality checks were not included in the $\boldsymbol{\mathcal{S}}$ (the region under a bad set did not contain voxels used in image reconstruction). All checks were completed for SD and DS for both data with I and ϕ. Firstly, all signals with higher noise amplitude than 1 µM in Total-hemoglobin concentration change (ΔT) were considered bad and excluded from further analysis as noise of this amplitude would dominate over responses associated with functional or physiological cerebral hemodynamics. This threshold was evaluated by first high-pass filtering to 1.7 Hz (chosen to be above heart rate) to eliminate power from physiological oscillations. Then the average of the sliding windowed standard deviation (window size of 10 s) was taken as the noise amplitude (corrected for power lost at low f from the filter, assuming white noise).

Further quality evaluation was conducted beyond the wavelet COH analysis described in subsection 4.2.3. Any voxels with a Sensitivity to an absorption change ($\mathcal{S}$) below the 1$^{\text{st}}$ percentile of all $\mathcal{S}$ in $\boldsymbol{\mathcal{S}}$ were ignored, as well as any measurement pairs that measured less than 0.001 µM mmHg^{-1} in amplitude. The reasoning for the former is that voxels with small $\mathcal{S}$ will create large artifacts in image reconstruction (only partially addressed by Tikhonov

regularization), and the reason for the latter is that one cannot claim that such a small amplitude transfer function vector is measurable considering the noise in the system. An amplitude below 0.001 µM mmHg^{-1} would correspond to a small oscillation in cerebral hemodynamics on the order of 0.01 µM considering a typical ABP oscillation amplitude on the order of 10 mmHg.

4.3 Results

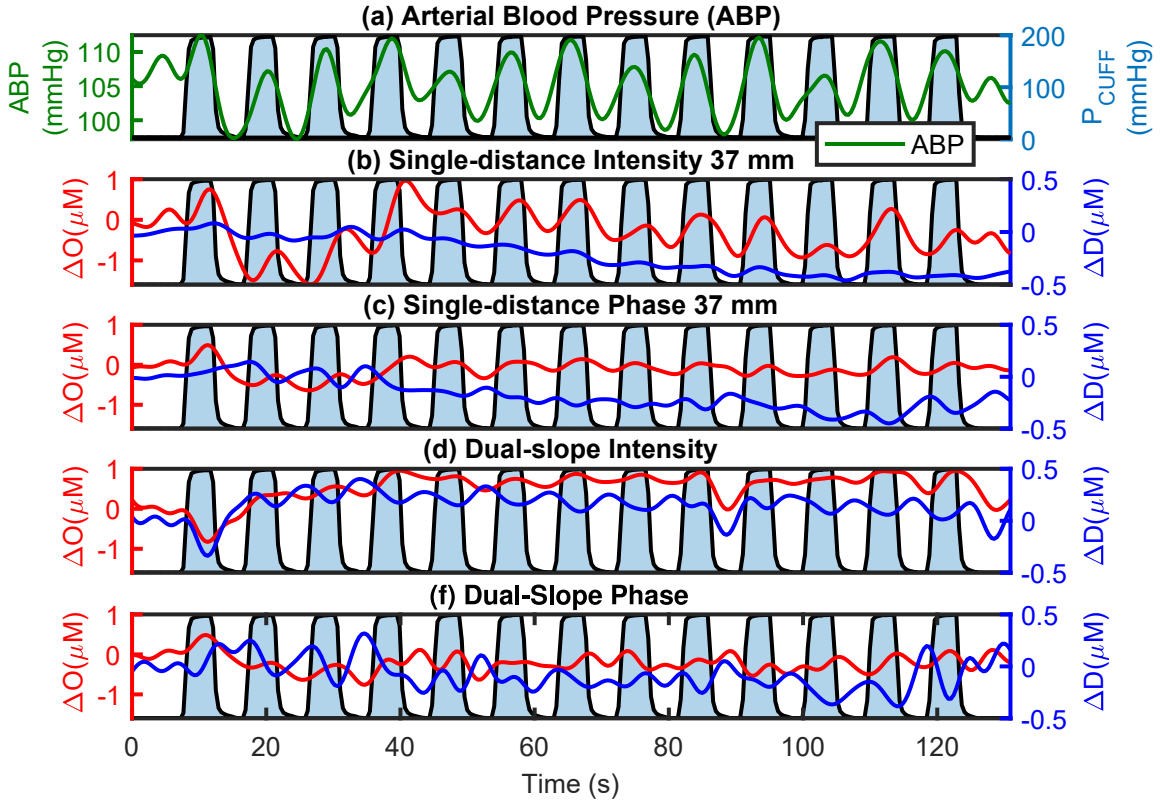

Figure 4.3: Example time traces of (a) Arterial Blood Pressure (ABP), Oxy-hemoglobin concentration change (ΔO) and Deoxy-hemoglobin concentration change (ΔD) calculated using data from (b) Single-Distance Intensity (SDI) at 37 mm, (c) Single Distance phase (SDϕ) at 37 mm, (d) Dual-Slope Intensity (DSI) and (e) Dual Slope phase (DSϕ) during thigh cuff oscillations. In all panels the thigh cuff oscillations are colored in light blue, with the measured pressure of the pneumatic thigh cuffs (P_{CUFF}) shown in (a). Presented data was taken with the hexagonal probe on subject 1. All signals were low-pass filtered to 0.2 Hz for visualization.

Figure 4.4, Figure 4.5, Figure 4.7, and Figure 4.7 present the reconstructed images for systemic ABP oscillations. The reconstructed images show the amplitude ratio and phase difference for $\widetilde{D}/\widetilde{O}$ and $\widetilde{T}/\widetilde{ABP}$. Interpretation of these maps requires the simultaneous examination of the amplitude ratio ($|\widetilde{D}/\widetilde{O}|$ or $|\widetilde{T}/\widetilde{ABP}|$) and the phase difference ($\angle(\widetilde{D}/\widetilde{O})$ or $\angle(\widetilde{T}/\widetilde{ABP})$) of the phasors. $\widetilde{D}/\widetilde{O}$ represents the interplay between BV and BF oscillations as described by CHS [95]. When the vector has an angle of π rad and a magnitude of 1, the $\widetilde{D}$ and $\widetilde{O}$ are in opposition of phase and have the same amplitude, thus the measured hemodynamics are dominated by BF. On the other hand, when $\widetilde{D}/\widetilde{O}$ has an angle of 0 rad, the phasors are in-phase, and the measured hemodynamics are dominated by BV. $\widetilde{T}/\widetilde{ABP}$ is used as a BV surrogate, where a higher amplitude ratio suggests larger BV oscillations. Superficial scalp tissue hemodynamics are considered mostly being dominated by BV oscillations driven by blood pressure changes. In contrast, hemodynamics in the brain are mostly associated with BF oscillations and limited BV oscillations (attributed to the limited compressibility of the brain within the skull). This thought process was used to analyze the large imaging array and modular hexagonal array reconstructed images using SDI, Single Distance phase (SDϕ), Dual-Slope Intensity (DSI), and Dual Slope phase (DSϕ).

4.3.1 Large Imaging Array

Figure 4.4 shows the results from a repeated systemic ABP oscillation experiment using a large imaging array with 57 SD sets and 30 DS sets on one subject. The images show either $\widetilde{D}/\widetilde{O}$ or $\widetilde{T}/\widetilde{ABP}$ (Figure 4.4(a-h) and Figure 4.4(i-p), respectively). Figure 4.4 is reported in Blaney and Fernandez *et al* (2023) [13]. White areas indicate a lack of data after data quality restrictions were enforced. Note that areas for the same data types (i.e., SDI, SDϕ, DSI, and DSϕ) for both $\widetilde{D}/\widetilde{O}$ and $\widetilde{T}/\widetilde{ABP}$ are missing the same areas of data, due to the method used for image reconstruction (subsection 4.2.4).

$\widetilde{D}/\widetilde{O}$ images are shown in Figure 4.4(a)-(h). All data types except SDI found the signature of BF-dominated hemodynamic oscillations in the upper portion of the array (cor-

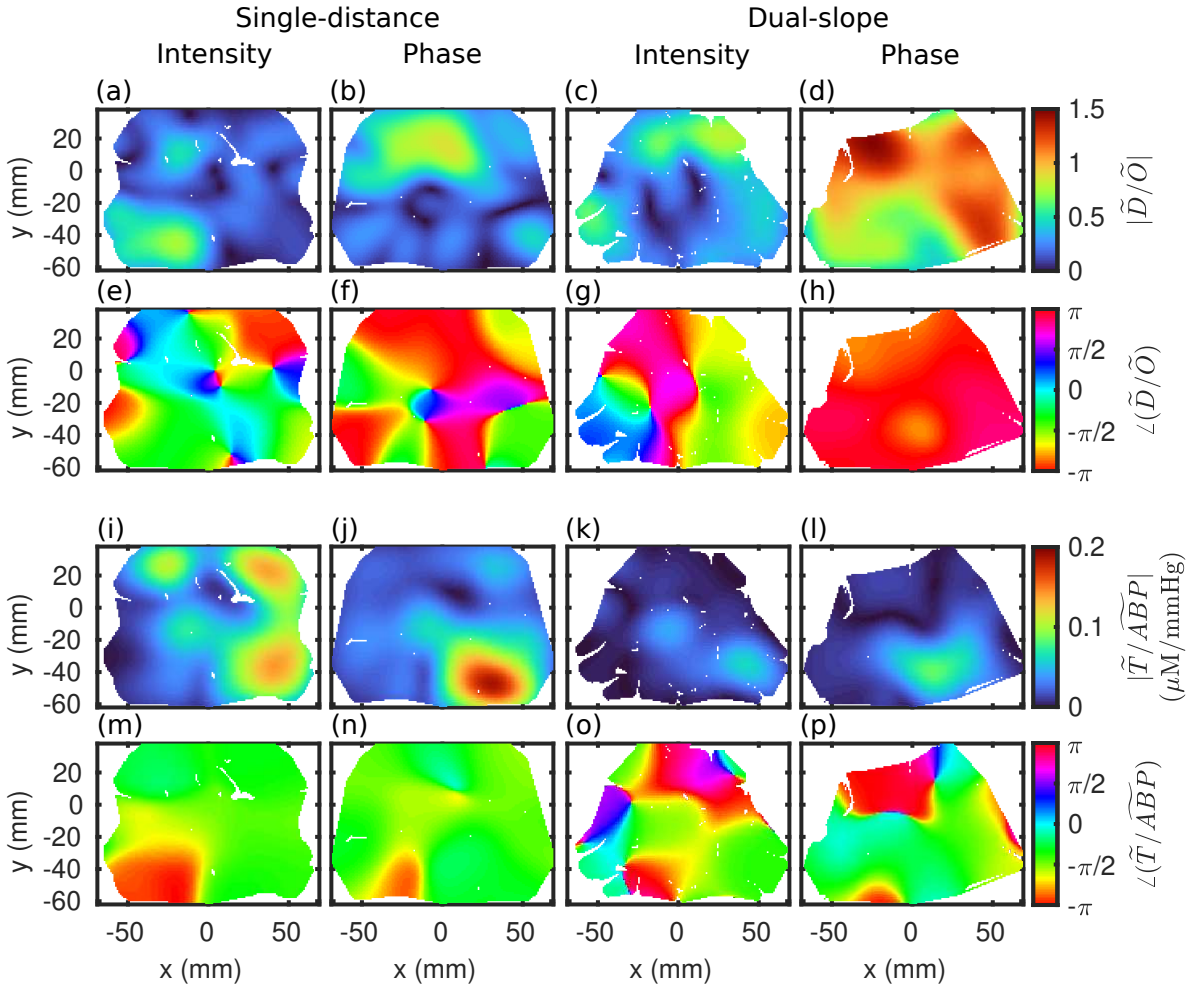

Figure 4.4: Reconstructed maps of the phasor ratio vector between Deoxy-hemoglobin and Oxy-hemoglobin ($\widetilde{D}/\widetilde{O}$) (a)-(g) and the phasor ratio vector between Total-hemoglobin and Arterial blood pressure ($\widetilde{T}/\widetilde{ABP}$) (i)-(p) at an Arterial Blood Pressure (ABP) oscillation frequency of 0.11 Hz for Single-Distance Intensity (SDI) (a)(e)(i)(m), SDϕ (b)(f)(j)(n), Dual-Slope Intensity (DSI)(c)(g)(k)(o), and DSϕ(d)(h)(l)(p) from the large array. White areas indicate a lack of data after data quality restrictions were enforced.

responding to the *occipital* lobe) but not in the thicker tissue, including skeletal muscle, probed in the lower portion of the array (Figure 4.2(a)). In particular, DSϕ displays BF-driven hemodynamics at almost every probed location, with a higher amplitude of $\widetilde{D}/\widetilde{O}$ in the top of the image. Meanwhile, SDϕ and DSI exhibit BF-driven hemodynamics in the upper portion of the image, but very low $|\widetilde{D}/\widetilde{O}|$ values in the lower portion, likely making the $\angle(\widetilde{D}/\widetilde{O})$ in that region unreliable. Looking at SDI, there is a low value of $|\widetilde{D}/\widetilde{O}|$ in the

upper and right portions of the imaged area, again indicating unreliability of the $\angle(\widetilde{D}/\widetilde{O})$ image in those regions. However, the lower left portion of the SDI image does show a larger value of $|\widetilde{D}/\widetilde{O}|$ and corresponding in-phase $\angle(\widetilde{D}/\widetilde{O})$ suggesting a BV-driven hemodynamic oscillation or some combination of BF and BV contributions.

Images of $\widetilde{T}/\widetilde{ABP}$ relate BV oscillations (using the Total-hemoglobin phasor ($\widetilde{T}$) as a BV surrogate) to the $\widetilde{ABP}$ and can give insight when combined with information gathered from $\widetilde{D}/\widetilde{O}$. It can be noticed from $|\widetilde{D}/\widetilde{O}|$ and $|\widetilde{T}/\widetilde{ABP}|$ across all images (Figure 4.4(a-d) and (i-m)) that areas of the high amplitude of one parameter correspond to a lower amplitude in the other. Looking at SDI, all regions with a low $|\widetilde{D}/\widetilde{O}|$ show a relatively large $|\widetilde{T}/\widetilde{ABP}|$. This means that for SD$I$, the entire upper portion and lower right portion of the array measured a strong $\widetilde{O}$ amplitude which dwarfed $\widetilde{D}$, likely due to dominating BV oscillations of the arterial vascular compartment. For the SDI measurements in the lower left portion, there is a low $|\widetilde{T}/\widetilde{ABP}|$ meaning that the $\angle(\widetilde{T}/\widetilde{ABP})$ value is likely unreliable. However, these results, in combination with the $\widetilde{D}/\widetilde{O}$ image, lead to an additional observation. In this portion of the imaged area, SDI measured $\widetilde{O}$ and $\widetilde{D}$ both with a large amplitude and with an intermediate relative phase (i.e., between 0 rad and $\pi/2$ rad), resulting in a small $|\widetilde{T}/\widetilde{ABP}|$. This result most probably means that SDI in this portion of the array measured a combination of BV and BF contributions to the observed hemodynamics. For DSI and DSϕ, regions at the bottom of the probe that showed smaller $|\widetilde{D}/\widetilde{O}|$ and $\angle(\widetilde{D}/\widetilde{O})$ further from π rad show a larger $|\widetilde{T}/\widetilde{ABP}|$ amplitude and $\angle(\widetilde{T}/\widetilde{ABP})$ being mostly in-phase or slightly negative. In this case, DSϕ has a $\angle(\widetilde{T}/\widetilde{ABP})$ slightly closer to 0 rad than DSI, suggesting a measurement less affected by BV oscillations. This same sort of image is obtained with SDϕ, only with a higher $|\widetilde{T}/\widetilde{ABP}|$ compared to DSI and DSϕ. Note that since $\widetilde{ABP}$ is the same for all images, this means that $\widetilde{T}$ had a higher amplitude for SDϕ in the lower right than DSI and DSϕ.

In summary, DSϕ measured a BF oscillation across the image that is strongest in the upper portion, and both DSI and SDϕ measured a BF oscillation in the upper portion of the

image, and SDI measured a BV or BV mixed with BF oscillation in the lower left portion. Note again that the upper portion of the image corresponds to the *occipital* lobe, while the lower portion is likely probing the subject's posterior neck muscles. While this imaging array can cover a large head region, the material and need for numerous sources and detectors make it difficult to conform to the head. With comfort in mind, the modular hexagonal arrays were designed and constructed.

4.3.2 Hexagonal Arrays

Figure 4.5, Figure 4.7, and Figure 4.8 show reconstructed images for three different subjects using the two modular hexagonal probes on the forehead (Figure 4.2(b)). Here, the use of left and right refer to the reader's left and right. All figures follow the same format as Figure 4.4 where panels (a-h) show $\widetilde{D}/\widetilde{O}$ and panels (i-p) show $\widetilde{T}/\widetilde{ABP}$ and blue circles are sources and red squares are detectors. The protocol and data processing steps for the large array and modular hexagonal arrays were consistent to to allow for the same assessment. Analysis of $\widetilde{D}/\widetilde{O}$ and $\widetilde{T}/\widetilde{ABP}$ will be done simultaneously to understand the contributions of BF and BV to the reconstructed phasor ratios.

Starting with subject 1 (Figure 4.5), SDI shows the smallest $|\widetilde{D}/\widetilde{O}|$ for both optical probes with a phase difference closer to π rad in the lower region of the right probe. All regions with a low $|\widetilde{D}/\widetilde{O}|$ show a relatively large $|\widetilde{T}/\widetilde{ABP}|$ which suggests a $\widetilde{O}$ amplitude that dwarfed $\widetilde{D}$, likely due to dominating BV oscillations of the arterial vascular compartment. This trend was also seen in the large imaging array results (Figure 4.4). Moving across the subplots, SDϕ reconstructed a larger maximum $|\widetilde{D}/\widetilde{O}|$ than SDI and a phase difference of π rad across both optical probes with low amplitude in $\widetilde{T}/\widetilde{ABP}$. This result suggests a lower contribution from BV in SDϕ compared to oscillations measured with SDI. For DS, the largest amplitude ratio and phase difference closer to π rad is reconstructed with DSϕ, suggesting a larger contribution from BF. This result is supported by a low $|\widetilde{T}/\widetilde{ABP}|$, which was $\sim$16 times smaller than that reconstructed with SDI. Comparing the amplitude ratios

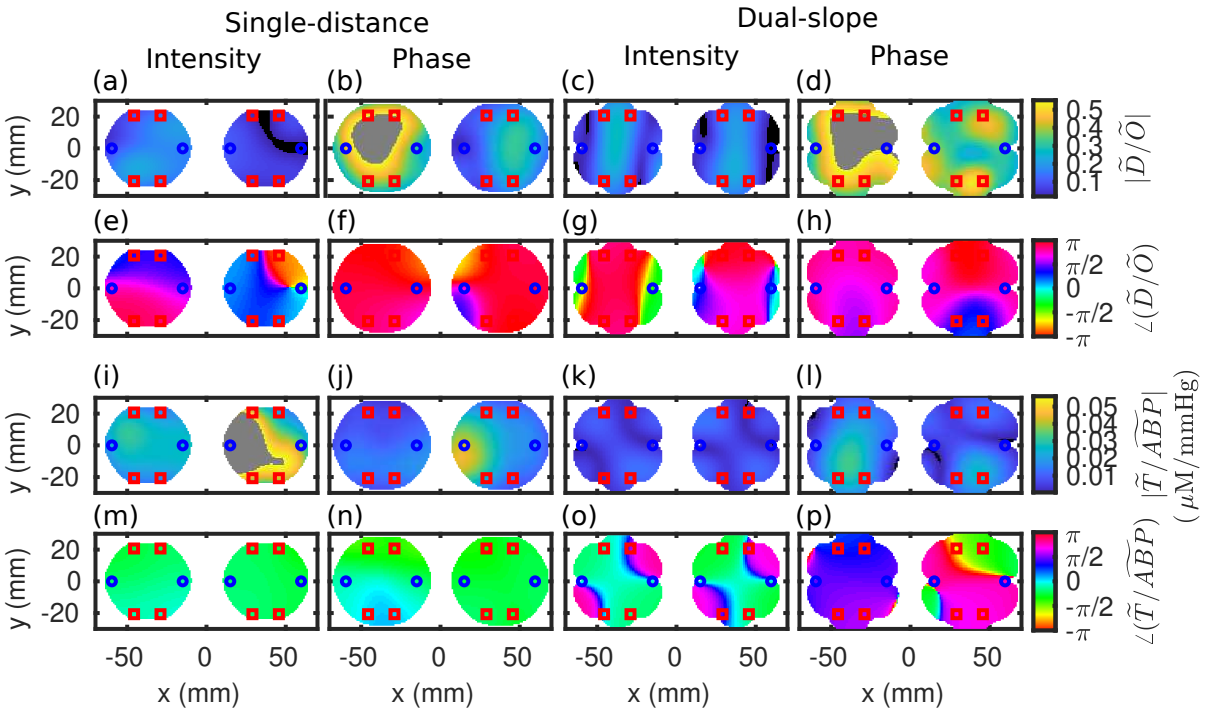

Figure 4.5: The phasor ratio vector between Deoxy-hemoglobin and Oxy-hemoglobin ($\widetilde{D}/\widetilde{O}$) (a)-(g) and the phasor ratio vector between Total-hemoglobin and Arterial blood pressure ($\widetilde{T}/\widetilde{ABP}$) (i)-(p) reconstructed maps at 0.11 Hz for Single-Distance Intensity (SDI) (a)(e)(i)(m), SDϕ (b)(f)(j)(n), Dual-Slope Intensity (DSI)(c)(g)(k)(o), and DSϕ(d)(h)(l)(p) from the large array. White areas indicate a lack of data after data quality restrictions were enforced for subject 1 with the two modular arrays. White areas indicate a lack of data after data quality restrictions were enforced, blue circles depict the location of the detectors, and red squares depict the location of the optical sources.

for $\widetilde{D}/\widetilde{O}$, the DS$\phi$ recovered higher values over the entirety of the optical probe as compared to SDI, with the maximum for DSϕ being $\sim$2.5 times larger. Interestingly, the right optical probe (readers right) measured a lower $|\widetilde{D}/\widetilde{O}|$ and larger $|\widetilde{T}/\widetilde{ABP}|$ as compared to the left optical probe throughout all of the data types.

Looking closely at the phase between $\widetilde{D}$ and $\widetilde{O}$ for DSϕ (Figure 4.5(h)), the lower region of the probe reconstructs a phase difference of $\pi/2$ rad while the upper region has a phase difference of π rad. The probe on the right side shows the largest difference between the top and bottom of the probe for $\angle(\widetilde{D}/\widetilde{O})$ with a larger $|\widetilde{T}/\widetilde{ABP}|$ for the bottom portion of the probe. This suggested that the bottom region of the optical probe measured more

BV versus BF oscillations. This difference over spatial location on the probe can potentially be explained by heterogeneous cerebral hemodynamics. However, differing skull thickness may also contribute, as previous work has shown that top layer thickness (i.e., scalp + skull) affects the sensitivity to deeper layers [92]. The approximate top layer thickness at the top of the probe was ∼7 mm while the bottom was ∼9 mm, where a thicker skull was the potential cause for a phase difference between ΔO and ΔD oscillations further from π rad. Figure 4.6 shows an ultrasound image of the right forehead under the optical probe where the blue circle represents the top of the ultrasound probe placed upwards facing the hairline. It can be visually seen in both Figure 4.6(a) and Figure 4.6(b) that the upper portion of the skull is thicker than that of the lower portion. This result is presented in Fernandez *et al* (2023) [126].

For subject 2 (Figure 4.7), a similar story is seen regarding the trends across data types. Data measured with SDI showed the smallest $|\widetilde{D}/\widetilde{O}|$ with the largest $|\widetilde{T}/\widetilde{ABP}|$ and a phase difference further from π for both optical probes. This suggests a larger BV oscillation as measured with SDI. The largest $|\widetilde{D}/\widetilde{O}|$ was reconstructed with DSϕ where the entirety of the optical probe showed a phase difference close to πrad and a low $|\widetilde{T}/\widetilde{ABP}|$. In this case, the reconstructed amplitude of $\widetilde{D}/\widetilde{O}$ was 5 times larger using DSϕ than SDI, with the amplitude of $\widetilde{T}/\widetilde{ABP}$ approximately 3 times larger with SDI. This result suggests a larger BF oscillation as measured with DSϕ. SDϕ has the second largest $|\widetilde{D}/\widetilde{O}|$ with a phase difference close to π rad for the top portion of both optical probes (Figure 4.7(c and g)). This lower region of the optical probes also had a larger $|\widetilde{T}/\widetilde{ABP}|$, which suggests a lower BF oscillation and a larger BV oscillation. This difference over spatial location may be attributed to a differing skull layer thickness on the top and bottom portions of the optical probe (as in Subject 1). DSI has a lower $|\widetilde{D}/\widetilde{O}|$ as compared to SDϕ and DSϕ and a phase difference close to π rad only in the upper region of the probe. All probes and data types reconstructed an $\angle(\widetilde{D}/\widetilde{O})$ that was homogeneous and consistent with previously reported results.

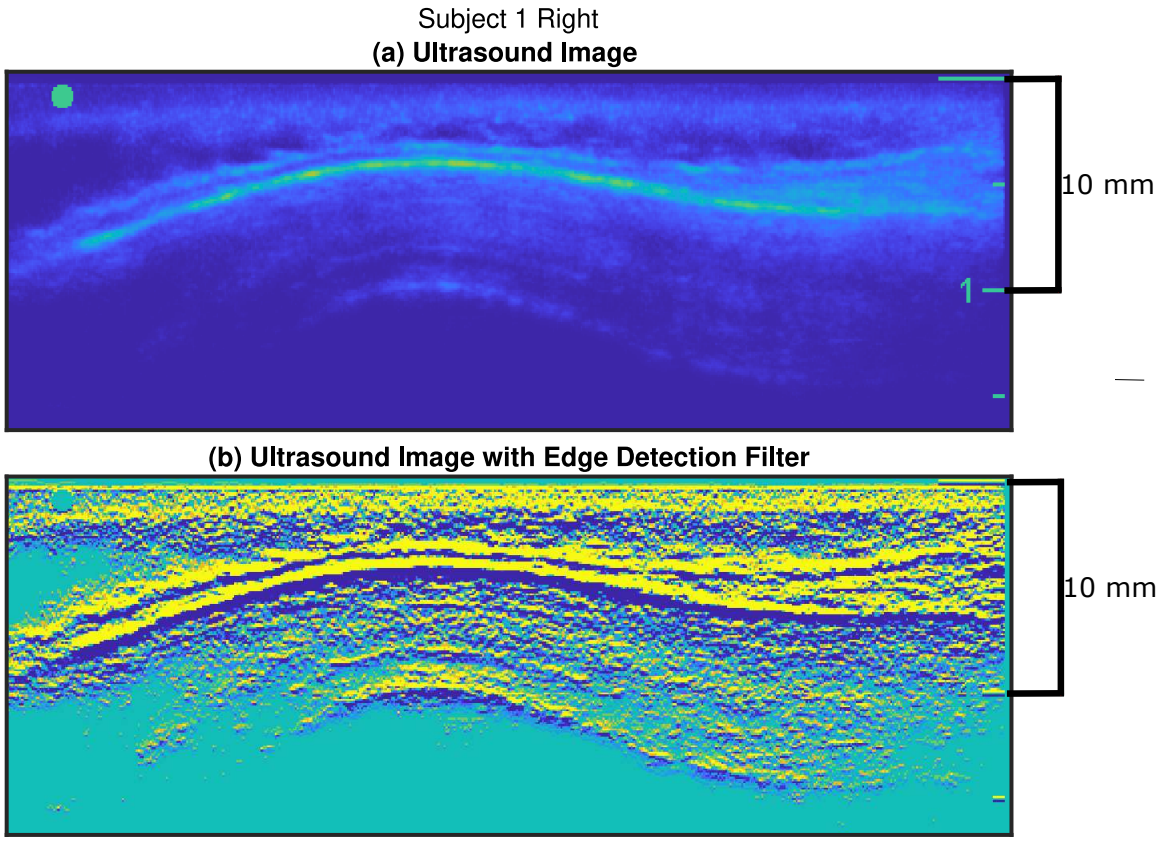

Figure 4.6: Example ultrasound image of the right side of the forehead taken on subject 1 where (a) shows the original image and (b) shows the image with an edge detection filter applied. The blue circle represents the top of the ultrasound transducer which was placed so that it was closest to the hairline and represents the top of the optical probe. In both images the scale bar represented 10 mm and the orientation of the image is consistent.

Figure 4.8 presents the reconstructed images for subject 3. Lack of data after the data quality evaluation (detailed in subsection 4.2.5) is evident in this subject, where the left probe is missing sections of data that is especially evident in the DSϕ. Comparing each data type and probe, the SDI showed the lowest $|\widetilde{D}/\widetilde{O}|$ (approximately 1.2 times smaller than DSϕ) and the highest $|\widetilde{T}/\widetilde{ABP}|$ ($\sim$3.7 times larger than DSϕ). This result is consistent with Subjects 1 and 2 and the large imaging array. Interestingly, the $\angle(\widetilde{D}/\widetilde{O})$ utilizing SDI data reconstructed a phase difference closer to πrad across a majority of the two optical probes, which suggests a limited effect of in-homogeneity, unlike Subjects 1 and 2. Looking across data-types, all reconstruct a $\angle(\widetilde{D}/\widetilde{O})$ closer to πrad. All data types except the

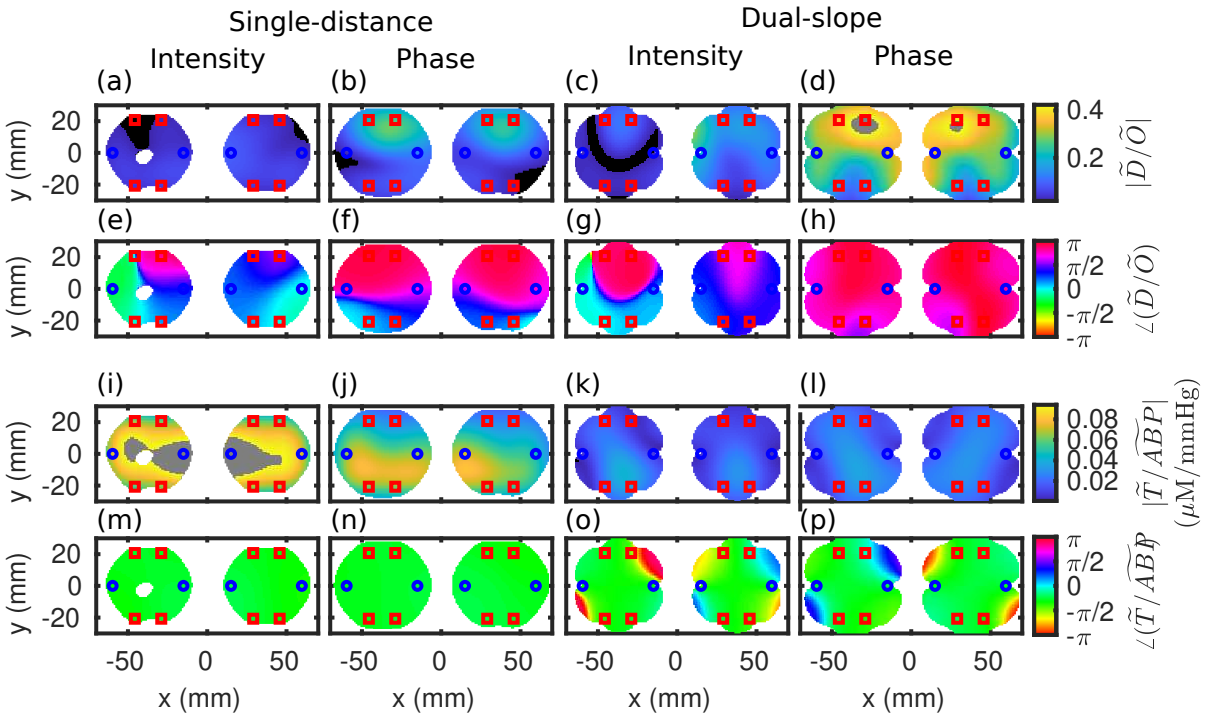

Figure 4.7: The phasor ratio vector between Deoxy-hemoglobin and Oxy-hemoglobin ($\widetilde{D}/\widetilde{O}$) (a)-(g) and the phasor ratio vector between Total-hemoglobin and Arterial blood pressure ($\widetilde{T}/\widetilde{ABP}$) (i)-(p) reconstructed maps at 0.11 Hz for Single-Distance Intensity (SDI) (a)(e)(i)(m), SDϕ (b)(f)(j)(n), Dual-Slope Intensity (DSI)(c)(g)(k)(o), and DSϕ(d)(h)(l)(p) from the large array. White areas indicate a lack of data after data quality restrictions were enforced for subject 2 with the two modular arrays. White areas indicate a lack of data after data quality restrictions were enforced, blue circles depict the location of the detectors, and red squares depict the location of the optical sources.

DSϕ reconstructed a relatively large $|\widetilde{T}/\widetilde{ABP}|$ across both optical probes where the SD reconstructed an amplitude ratio ∼3.7 times larger than DSϕ. This finding suggests a mix of BF and BV in all measurements but is least evident in DSϕ.

4.4 Discussion

Here we have used two different imaging arrays to reconstruct images of phasor ratio maps (specifically $\widetilde{D}/\widetilde{O}$ and $\widetilde{T}/\widetilde{ABP}$) to examine the contributions of BF and BV oscillations in different data types. The large imaging array results in Blaney and Fernandez *et al* (2023) [13]

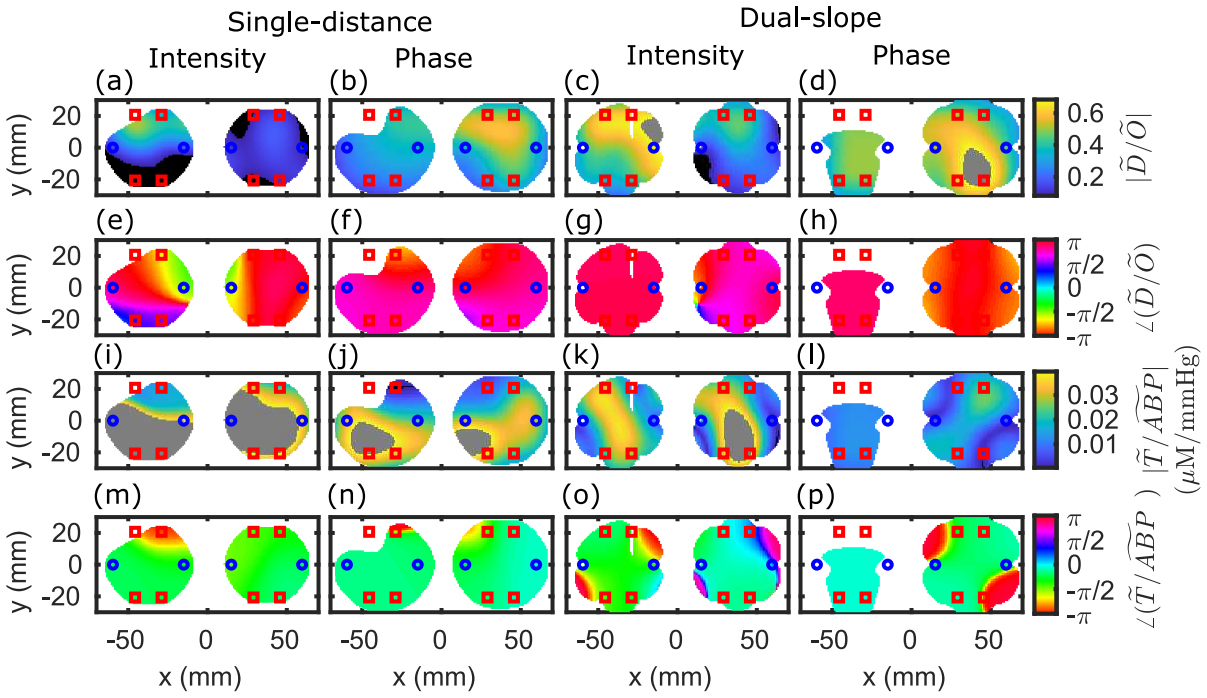

Figure 4.8: The phasor ratio vector between Deoxy-hemoglobin and Oxy-hemoglobin ($\widetilde{D}/\widetilde{O}$) (a)-(g) and the phasor ratio vector between Total-hemoglobin and Arterial blood pressure ($\widetilde{T}/\widetilde{ABP}$) (i)-(p) reconstructed maps at 0.11 Hz for Single-Distance Intensity (SDI) (a)(e)(i)(m), SDϕ (b)(f)(j)(n), Dual-Slope Intensity (DSI)(c)(g)(k)(o), and DSϕ(d)(h)(l)(p) from the large array. White areas indicate a lack of data after data quality restrictions were enforced for subject 3 with the two modular arrays. White areas indicate a lack of data after data quality restrictions were enforced, blue circles depict the location of the detectors, and red squares depict the location of the optical sources.

were the first to report imaging during a CHS protocol. The large array showed that all data types except SDI found BF dominated oscillations in the upper portion of the imaged area, corresponding to the *occipital* lobe (Figure 4.2(a)&Figure 4.4), and found BV oscillations in the lower right portion (primarily evident in SDϕ and DSI), corresponding to neck muscles. It is also noted that for DSϕ, some mixture of contributions from BV and BF oscillations may have been measured in the lower right portion. Meanwhile, SDI found BV dominated oscillations almost across the entire image except for the lower left portion, which measured a combination of BV and BF oscillations. The next step in this work was the implementation of the modular hexagonal arrays to CHS imaging, as they were more comfortable for the subjects and could be applied to a larger population of subjects. Results

using the modular hexagonal arrays on the forehead of 3 subjects showed results consistent with that of the large array. Specifically, all data types showed larger contributions from BF oscillations compared to SDI with DSϕ having BF oscillations over the majority of the optical probes. In some cases, the lower portion of the optical probe showed less BF driven oscillations corresponding to a larger skull thickness.

Presented results align with previous work using CHS, which found that during ABP oscillations, there is a transition between mainly measuring BV oscillations when probing more superficial tissue to measuring more BF oscillations when probing deeper tissue, as BF changes appear to dominate over BV changes in cerebral tissue[41, 127]. It is reasonable to expect that ABP oscillations result in stronger BV oscillations in scalp tissue than in brain tissue confined within the rigid skull enclosure. This result is consistent with previous work considering CHS [31, 41, 127] and may help explain the seemingly unresolved paradoxical results showing cerebral BV changes despite the incompressibility and rigidity of the brain fluid dynamic system [128]. These comparisons to previous works all focus on the phase and amplitude relationships of different data types, not on the spatial dependence of the hemodynamics.

One way to examine the spatial mapping results is in terms of the effect of superficial hemodynamics on measurements over the whole array. Contact pressure between the imaging array and the scalp can affect the superficial hemodynamics [129], creating in-homogeneities across the array if contact pressure is inconsistent throughout the entire array. This is particularly a concern when superficial dynamics dominate a measurement since the results may be significantly impacted by how the optical probe is applied to the subject's head. In these studies, no control was implemented to ensure that contact pressure did not suppress superficial hemodynamics, nor was contact pressure measured or controlled. For the large array data, this is one possible explanation for the in-homogeneity in measured amplitude ratio and phase difference for $\widetilde{D}/\widetilde{O}$ and $\widetilde{T}/\widetilde{ABP}$, especially for SD or I data types. Another possibility for in-homogeneity is the differing skull thicknesses, as previous work has shown

differing sensitivities to deeper tissues (i.e., the brain) as skull thickness increases [92]. While no skull thickness measurements were done for the large imaging array due to the large surface probed, they were taken on each subject for the modular hexagonal arrays. Ultrasound images (Figure 4.6) showed a smaller skull thickness for the upper portion of the optical probe than the lower portion. Notably, the measured skull thicknesses on the frontal bone were consistent with literature which has an average thickness of approximately 8 mm [130–132], where variability is seen in different subjects.

Requirements on $\widetilde{O}/\widetilde{ABP}$ and $\widetilde{D}/\widetilde{ABP}$ were set to ensure that only data with an amplitude of $0.001\,\mu M^{-1}\,mmHg$ (as described in subsection 4.2.5) were considered as these low amplitudes would lie well below reasonable noise. Smaller oscillations in ΔD are typically seen in data types that are more sensitive to superficial tissue (such as SDI at 37 mm in Figure 4.3(a)). Moving to data types with preferentially sensitive to deeper dynamics, these oscillations on ΔD become larger and closer to that of ΔO (Figure 4.3(d)). This result indicates that the lower ΔD oscillation is due to limited sensitivity to the brain and are mainly the contribution from superficial tissue to the signal. Small oscillations in ΔO can be a limiting factor, especially when below the noise threshold. Measurements of larger oscillations with SDϕ and DS are promising in limiting the effect of low ΔD oscillations and measuring larger ΔD oscillations associated with the brain.

4.5 Conclusions

In this work, we used a large imaging arrays and two modular hexagonal probes during a protocol based on induced oscillations in arterial blood pressure to evaluate cerebral hemodynamic oscillations and their association with BF and BV oscillations. Our results suggest that DSϕ is more sensitive to deeper tissue as it measures hemodynamic oscillations that are driven mainly by BF as expected in cerebral tissue, while SDI measures hemodynamics that are driven mainly by BV as expected in scalp tissue. Differing skull thickness across the

measurement region was shown to potentially influence recovered dynamics, which highlights the importance of this measurement in interpreting results. The use of DS DOI with CHS allows for spatial mapping of hemodynamics that are more closely representative of the brain compared to SD imaging methods. Presented results are promising and show the ability to do spatial mapping using these modular DS arrays. Future work includes measurements on multiple subjects with differing skull thicknesses as well as across multiple oscillation frequencies to spatially study the CHS frequency spectrum, looking into measurements of spontaneous hemodynamic oscillations, and exploring methods to secure the imaging array with even contact pressure that is monitored and controlled throughout the measurement.

4.6 Acknowledgments and Contributions

Authors who contributed to this work are Cristianne Fernandez, Giles Blaney, Angelo Sassaroli, and Sergio Fantini. All are with the Department of Biomedical Engineering at Tufts University.I would specifically like to thank Giles Blaney who designed both imaging arrays and constructed the large imaging array, as well as for his work on the imaging reconstruction methods.

Chapter 5

Coherent Spontaneous Hemodynamics in the Human Brain

5.1 Introduction

Arterial Blood Pressure (ABP) oscillations can be induced via physiological perturbations (such as with cyclic thigh cuff inflation as in Chapter 4 and Chapter 6) but also occur spontaneously. The use of spontaneous oscillations has the potential to increase the clinical translatibility of the proposed techniques in Chapter 4 and Chapter 6 as they do not require physiological perturbations. This will explore the use of spontaneous oscillation in ABP with the aim to show their usefulness and potential with Coherent Hemodynamics Spectroscopy (CHS).

Cerebral hemodynamics measured with Near-InfraRed Spectroscopy (NIRS) result from a combination of cardiac pulsation ($\sim$1 Hz), respiration ($\sim$0.2 Hz to 0.5 Hz) [133], Low Frequency Oscillations (LFOs) (Mayer waves; $\sim$0.1 Hz) [134], and very low-frequency oscillations ($\sim$0.01 Hz to 0.05 Hz) [133] that are mostly driven by ABP fluctuations. Spontaneous LFOs of systemic and cerebral vessels are affected by neuronal[135], metabolic[136], myogenic stimuli [137] and sympathetic changes [138–140]. LFOs have been investigated using NIRS,

Transcranial Doppler ultrasound (TCD), and other techniques for fundamental, functional connectivity and autoregulation studies [141].

Transfer Function Analysis (TFA) has been used in TCD to investigate the frequency dependence of the gain and phase for coherent oscillations of Cerebral Blood Flow Velocity (CBFV) and ABP [16, 89, 142, 143]. However, this technique is limited because it cannot measure microvasculature and localized changes in cerebral blood flow. Several systematic studies on the detection of LFOs by NIRS on human subjects have been reported[123, 137, 144] mainly focusing on 0.1 Hz. At this frequency, CBFV leads ABP meaning that there is a delay in the cerebrovascular resistance reaction to ABP changes [88, 145] as the cerebral regulatory system functions as a high-pass filter where low frequencies are dampened.[90] Studies have shown that this phase lag is affected in patients with impaired cerebral hemodynamics [145] which leads to the importance of measurements in this frequency range.

In the low-frequency range, the highest coherence between cerebral hemodynamics and ABP has been shown to lie around 0.1 Hz [137, 146] but this claim has been limited in the number of subjects investigated. Spontaneous oscillations have lower coherence than induced oscillations [94] and a lower signal-to-noise ratio [142], but are relevant when inducing oscillations is not feasible. Induced oscillations (as presented in Chapter 4 and Chapter 6) require physiological perturbations to subjects, such as thigh cuff oscillations, which are not feasible in specific populations, and can cause a lengthy protocol when multiple frequencies are wanted [89]. On the other hand, the use of spontaneous oscillations allows for the evaluation of multiple frequencies within the same time window, eliminates the need for any extra perturbations, and may be used on a broader range of subjects [89]. The motivation behind this work is to look at the amplitude ratio, phase shift and coherence in hemodynamic parameters of spontaneous oscillations in a relatively large data set.

In this chapter we report a study on 78 healthy human subjects involved in a simple driving task with a series of braking events with the goal of evaluating the use of spontaneous coherent hemodynamics. The time of coherent oscillations during 3 min periods was

evaluated over a large range of subjects to assess the extent to which spontaneous oscillations feature significant coherence. Transfer function analysis was done to evaluate the relative amplitude and phase between cerebral hemodynamics and ABP, at 0.1 Hz, with the goal of evaluating the variance within and across subjects. Lastly, the baseline driving condition and periods with braking events were compared to evaluate the impact of brain activation on coherent spontaneous cerebral hemodynamics. This work was published in Fernandez *et al* (2023) [147].

5.2 Methods

5.2.1 Study Protocol and Data Acquisition

A total of 78 subjects (42M, 36F, 18-39 years old) participated in 2 sessions in a Tufts University Institutional Review Board (IRB) approved study. Continuous-Wave (CW) cerebral NIRS and systemic ABP measurements were performed while the subject was in a RTI [Ann Arbor, MI USA] (medium fidelity partial-cab driving simulator), which has been previously described McWilliams *et al* (2018) [148]. CW-NIRS measurements were acquired with a NIRx Medical Technology [Berlin, Germany] (NIRScout) sampled at 7.81 Hz. The instrumental configuration consisted of 8 Light-Emitting Diode (LED) sources (wavelengths: 780 nm and 850 nm) and 7 Photo-Diode (PD) detectors which created 20 Single-Distance (SD) measurement channels at a source-detector spacing of 30 mm on the pre-frontal cortex (Figure 5.1(a)). A beat-to-beat finger plethysmography system, used to measure non-invasive ABP using changes in blood volume in the artery [149], was placed on the subjects' left fingers and upper arm. All ABP signals were sampled at 20 Hz. Figure 5.1(b) depicts the driving simulator set up with the Arterial Blood Pressure (ABP) and CW-NIRS instruments connected to the subject.

The driving simulator consisted of five 45 inch LCD screens that created a 180 deg field of view and had a working steering wheel, accelerator and brake pedals, and an automatic

gear shifter. The driving environment consisted of a two-lane highway in each direction lined with trees on a clear day during the daytime. Approximately every 30 s, a car passed the participants in the left lane, and traffic was light. The speed limit was listed at 65 mph, and each participant was instructed to maintain a comfortable and appropriate speed and stay in the right lane. The experimental protocol consisted of a baseline period in which the subject experienced uneventful, constant-speed driving for approximately 3 min on a 2-lane highway. Next, the participants engaged in a total of 10 events where the order was randomized for each subject and session. Six events were labeled as real braking (where the participant needed to brake to avoid a collision with a leading car that was braking) and four fake braking (where the leading car appeared but did not slow down to require the subject to brake). An example experimental protocol can be seen in Figure 5.1(a).

5.2.2 Near-InfraRed Spectroscopy and Arterial Blood Pressure Processing

Methods described here were independently applied to each subject, experiment session, and SD channel. NIRS Intensity (I) measurements for both wavelengths and the ABP signal were synchronized and interpolated to 20 Hz. All NIRS measurements were evaluated for artifacts due to non-physiological changes by linear piece-wise detrending, which found sections in which the variance of the signal is above the 75^{th} and below the 25^{th} percentiles and using these as breakpoints in the detrend. The Oxy-hemoglobin concentration change (ΔO) and Deoxy-hemoglobin concentration change (ΔD) were calculated using the modified Beer Lambert Law (as described in 2.3.2) with a wavelength dependent Differential Path-length Factor (DPF) using assumed absorption coefficient (μ_a) and reduced scattering coefficient (μ_s') at the two wavelengths [46]. Channels with non-physiological variation over 1 µM were disregarded from further analysis.[13] Values in time in which ABP re calibration occurred were automatically neglected in further analysis. Example time traces of ΔO and ΔD can be seen in Figure 5.2(b) and of ABP in Figure 5.2. 2(c) where the solid line shows the signal

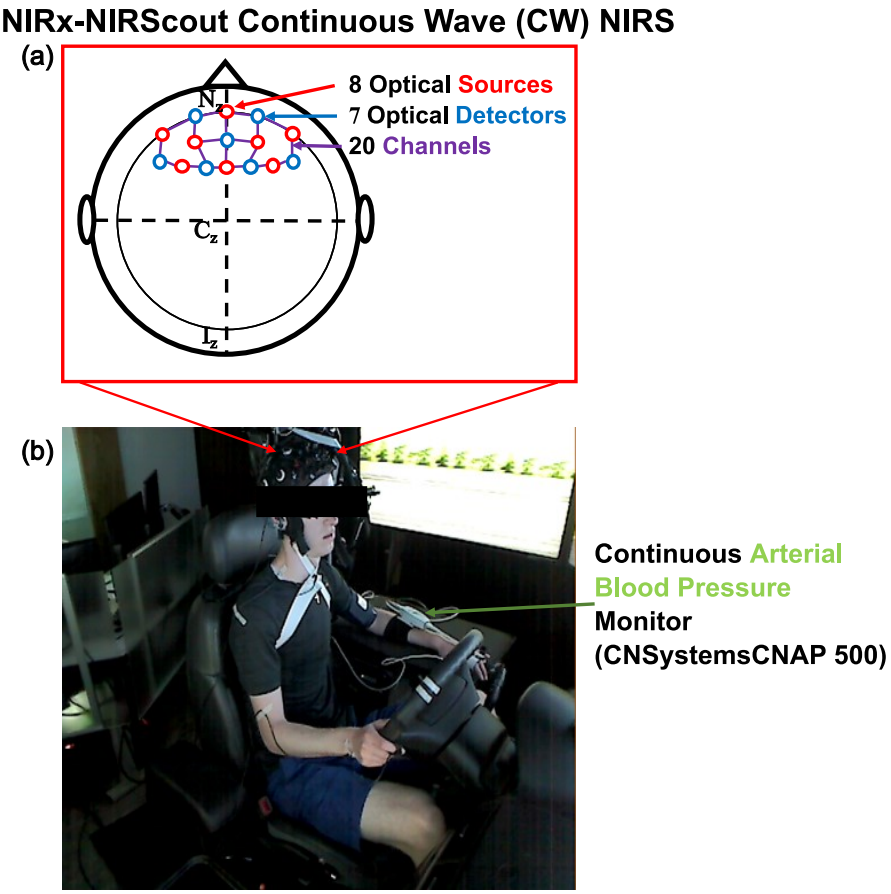

Figure 5.1: (a) Schematic of the location of the 8 optical sources and 7 detectors from the Continuous-Wave (CW) Near-InfraRed Spectroscopy (NIRS) instrument on the human head. (b) Experimental set-up, where a subject is seated with the CW-NIRS device on their head and the beat-to-beat finger plethysmography system for continuous Arterial Blood Pressure (ABP) measurements on their fingers and upper arm.

low-passed to 0.2 Hz and the shaded region is the original signal that reflects systolic-diastolic variation.

5.2.3 Transfer function and Coherence Analysis

Transfer function and coherence analysis between the hemodynamic signals (ΔO and ΔD) and ABP for all subjects, experiments, and channels utilizing the following methods. Data were first sectioned into a total of six 3 min non-overlapping blocks, where the first 3-minute block (minutes 0 to 3) is referred to as the baseline. Each block was then processed indepen-

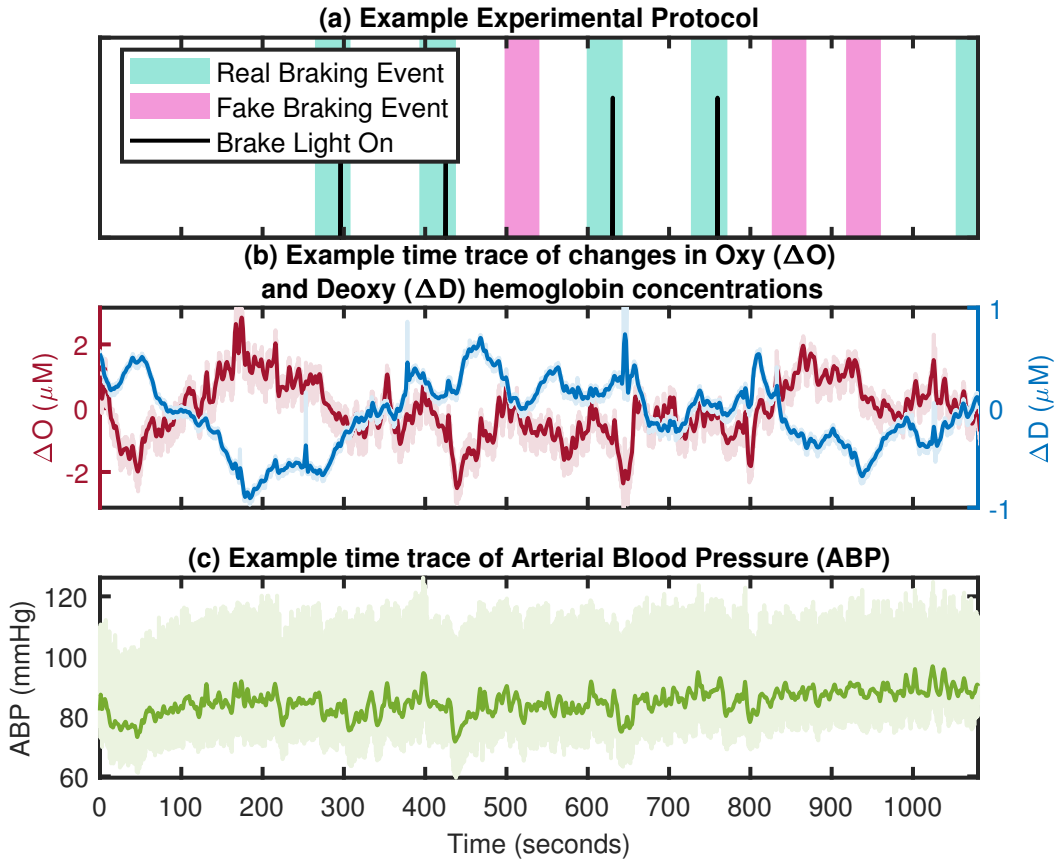

Figure 5.2: (a) Example protocol with the time markings of real and fake braking events and for when the leading cars brake lights turned on. (b) Time trace of Oxy-hemoglobin concentration change (ΔO) and Deoxy-hemoglobin concentration change (ΔD) calculated with data from on Single-Distance (SD) channel. (c) Time trace of the Arterial Blood Pressure (ABP) for the same subject. For (b) and (c) the solid lines depict the signal low-passed to 0.2 Hz and the shaded region encompasses unfiltered data.

dently. All data sets used in this work were over 18 min in length, so each block had the same number of subjects. Time-frequency maps of the wavelet coherence between ΔO and ABP, and ΔD and ABP were calculated using a modified version of MATLABs wcoherence function that removes smoothing in frequency. A coherence threshold generated using random surrogate data (alpha level = 0.05) [150, 151] was applied so that only pixels in time and frequency that have statistically significant coherence were evaluated. Figure 5.3(a) shows the time-frequency map of the coherence between ΔO and ABP for the example time trace in Figure 5.2 and Figure 5.3(b) shows the pixels in time and frequency that have statistically

significant coherence. Multiple comparisons were not accounted for. A logical AND was taken between the ΔD-ABP and ΔO-ABP maps to create a significant coherence map used for ΔO and ΔD. Transfer function analysis between time signals of ΔO and ABP, ΔD and ABP, and ΔD and ΔO for each block were performed using the continuous wavelet transform with a complex Morlet mother wavelet to find maps of the phasor ratio vector between Oxy-hemoglobin and Arterial blood pressure ($\widetilde{O}/\widetilde{ABP}$), phasor ratio vector between Deoxy-hemoglobin and Arterial blood pressure ($\widetilde{D}/\widetilde{ABP}$), and phasor ratio vector between Deoxy-hemoglobin and Oxy-hemoglobin ($\widetilde{D}/\widetilde{O}$) in time and frequency [19, 31]. This analysis resulted in the amplitude ratio and the phase difference between the two parameters across time and frequency.

5.2.4 Coherent Requirements and Spontaneous Oscillations Frequencies

Coherent spontaneous oscillations within the range of 0.01 Hz to 1.5 Hz were considered. A series of central frequencies and their bandwidths (as determined by the half-power bandwidth of a sinusoidal wave at that central frequency [19]) were found. In total, there were 18 central frequencies with a bandwidth of approximately 5 frequencies. Maps of significant coherence for Oxy-hemoglobin phasor ($\widetilde{O}$) and Arterial blood pressure phasor ($\widetilde{ABP}$), Deoxy-hemoglobin phasor ($\widetilde{D}$) and $\widetilde{ABP}$, and the logical AND were further filtered to require that in each frequency band of interest, significant coherence lasted longer than one period of the central frequency and significant coherence at the central frequency. Filtered maps were applied to the phasor ratio maps so that only pixels in time and frequency with statistically significant coherence that passed the requirements were considered in further analysis. The logical map between ΔD-ABP and ΔO-ABP was applied to the phasor ratio map of $\widetilde{D}/\widetilde{O}$ as only times with coherent systemic oscillations in both hemodynamic parameters are of interest. An average phasor ratio was computed for $\widetilde{O}/\widetilde{ABP}$, $\widetilde{D}/\widetilde{ABP}$, and $\widetilde{D}/\widetilde{O}$ over each frequency band, resulting in one value for each block (6), channel (20), subject (78), and

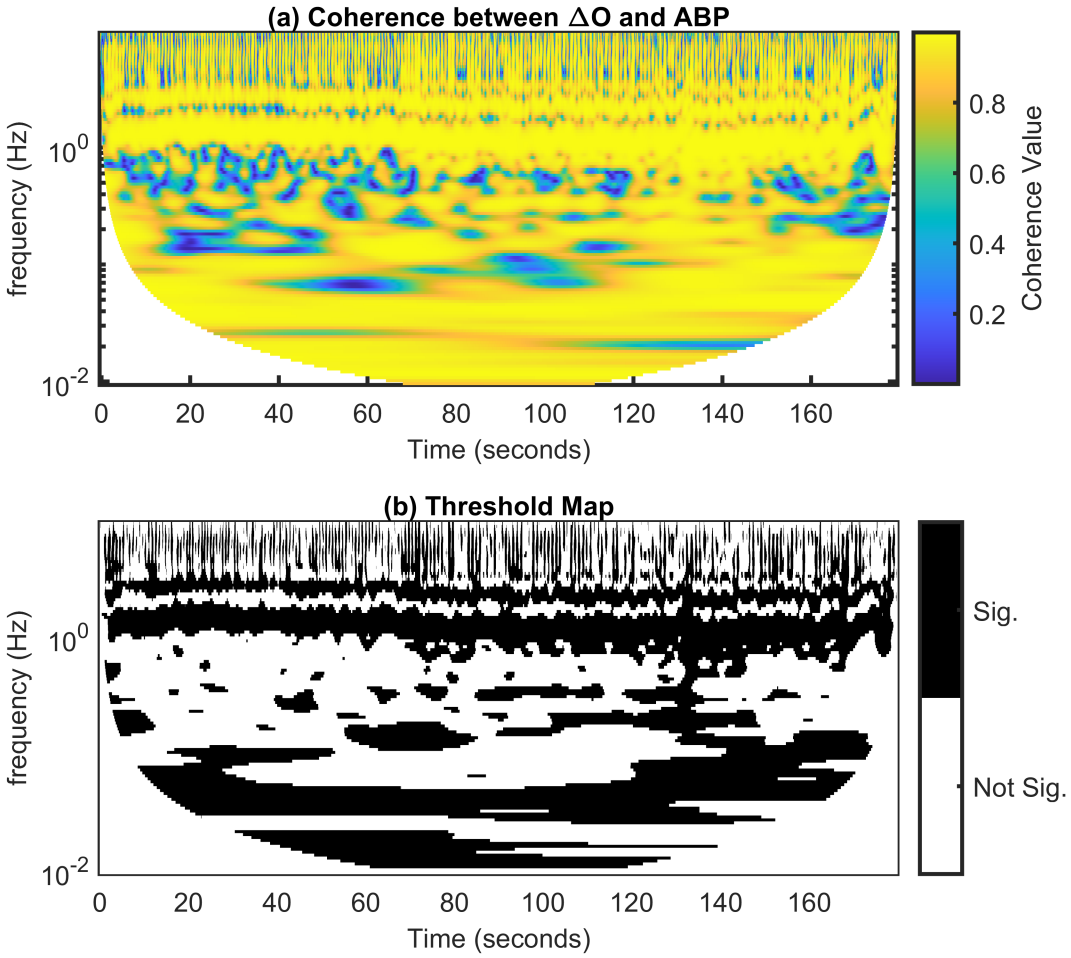

Figure 5.3: (a) Wavelet coherence between Oxy-hemoglobin concentration change (ΔO) and Arterial Blood Pressure (ABP) with data from on Single-Distance (SD) channel. (b) Coherence that passed the coherence threshold applied to the data set in (a).

session (2) across frequency.

5.3 Results

5.3.1 Availability of Coherent Hemodynamics

The fraction of time, during baseline, for which the coherence requirements were fulfilled (statistically significant coherence for at least one period of the central frequency) across frequency are shown in Figure 5.4(a) for $\widetilde{O}/\widetilde{ABP}$, $\widetilde{D}/\widetilde{ABP}$ and for the logical AND between

$\widetilde{D}/\widetilde{ABP}$ and $\widetilde{O}/\widetilde{ABP}$. The values for each channel, subject, and experiment were treated as independent data points. This means that there was a maximum number of 120 data points at each frequency. Figure 5.4(b) depicts the number of subjects with significant data in 10 or more CW-NIRS channels. The highest fraction of time with coherence occurred at approximately 1 Hz, which is indicative of the heart rate. At this frequency, $\widetilde{O}/\widetilde{ABP}$ has the highest fraction of coherence as arterial pulsation results in hemodynamic oscillations that are primarily associated with oxyhemoglobin (oxygen saturation of arterial blood is close to 100 %). Large arterial oscillations can be seen in Figure 5.2(b) in the ΔO, while the ΔD signal has a smaller contribution. The peak at approximately 0.3 Hz is due to respiration. At minimum, 90 % of subjects and sessions had data in at least 10 channels. Some channels may have been excluded from analysis due to motion artifacts or re-calibration of the ABP signal.

In the range of physiologically relevant frequencies for assessing cerebral health (0.01 Hz to 0.1 Hz),[17, 141] the highest fraction of time of coherence occurred at approximately 0.1 Hz with on average ∼32 % for $\widetilde{O}/\widetilde{ABP}$, ∼19 % for $\widetilde{D}/\widetilde{ABP}$, and ∼13 % for $\widetilde{D}/\widetilde{O}$. Out of 158 data sets, there were 139, 131, and 91 available for the respective data types. At all frequencies, $\widetilde{O}/\widetilde{ABP}$ showed the largest fraction, followed by $\widetilde{D}/\widetilde{ABP}$. The logical condition is the lowest on average, which shows that ΔO is not always coherent with ABP when ΔD is coherent with ABP. This result indicates that both hemodynamic parameters are not always concurrently driven by ABP.

5.3.2 Average Baseline Phasor Ratios

Figure 5.5(a), (b), and (c) show the average phasor ratios at 0.1 Hz over channels and sessions for each subject. In this case, there is one phasor ratio for each subject (a total of 78) except for $\widetilde{D}/\widetilde{O}$ which has 77 due to one subject having no data that passed all of the coherence requirements. Averaging over the channels and sessions gives insight into the variability across subjects. The lowest spread in phase difference was seen in $\widetilde{O}/\widetilde{ABP}$ (Figure 5.5(a)), while

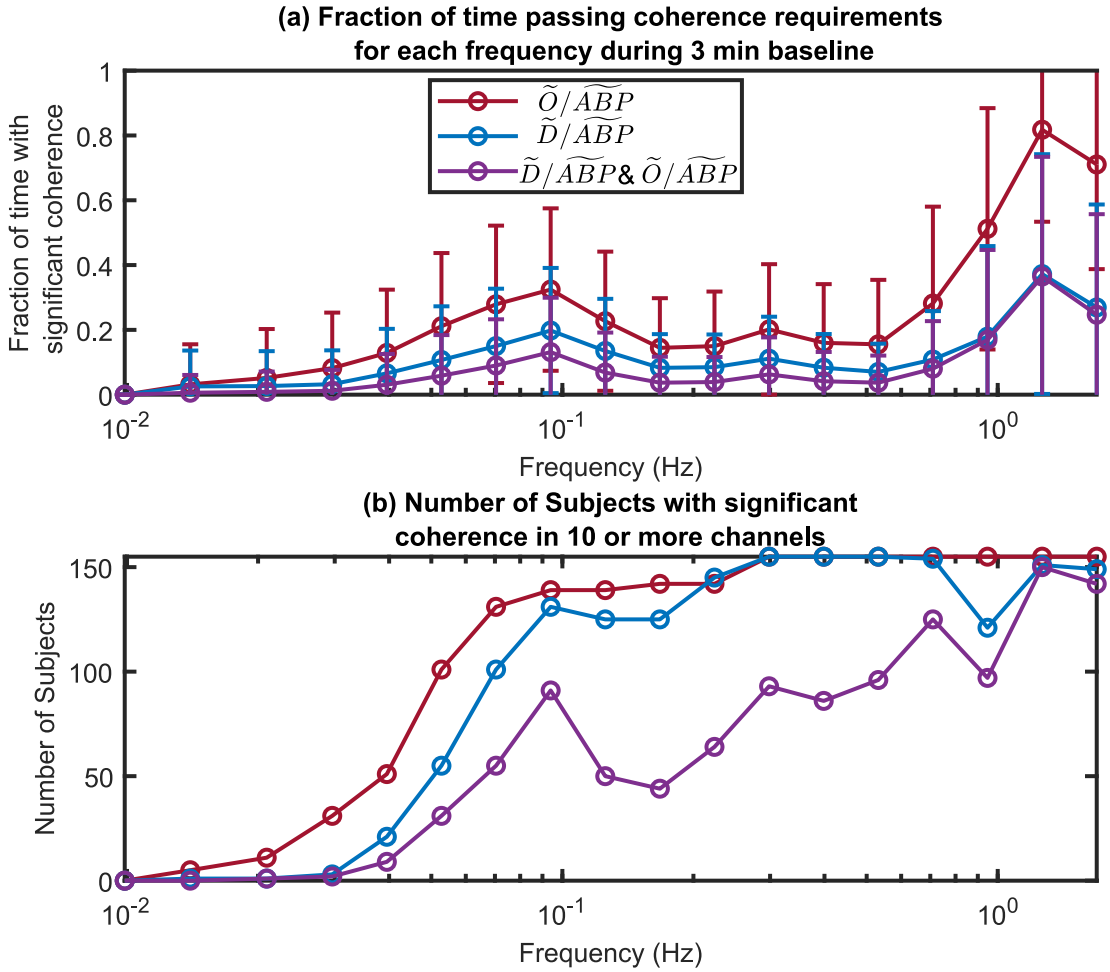

Figure 5.4: (a) Fraction of time during the baseline in which the coherence requirements were met for each frequency for the phasor ratio vector between Oxy-hemoglobin and Arterial blood pressure ($\widetilde{O}/\widetilde{ABP}$), phasor ratio vector between Deoxy-hemoglobin and Arterial blood pressure ($\widetilde{D}/\widetilde{ABP}$), and the logical AND between $\widetilde{O}/\widetilde{ABP}$ and $\widetilde{D}/\widetilde{ABP}$. (b) Number of subjects across frequency in which 10 or more channels had statistically significant coherence that passed the coherence requirements.

$\widetilde{D}/\widetilde{ABP}$ varied by ∼120 deg, with varying amplitude ratios across subjects. For $\widetilde{D}/\widetilde{ABP}$ and $\widetilde{D}/\widetilde{O}$, as the phase difference approached 0 the amplitude decreased. Figure 5.5(d), (e), and (f) show the average phasor ratios at 0.1 Hz over subjects and sessions for each channel leading to 20 phasor ratios per plot (i.e., one for each SD channel). Averaging over subjects and sessions for each channel gives insight onto the spatial variability over the probed brain region. Neither $\widetilde{O}/\widetilde{ABP}$, $\widetilde{D}/\widetilde{ABP}$, or $\widetilde{D}/\widetilde{O}$ show qualitative significant differences among

the channels.

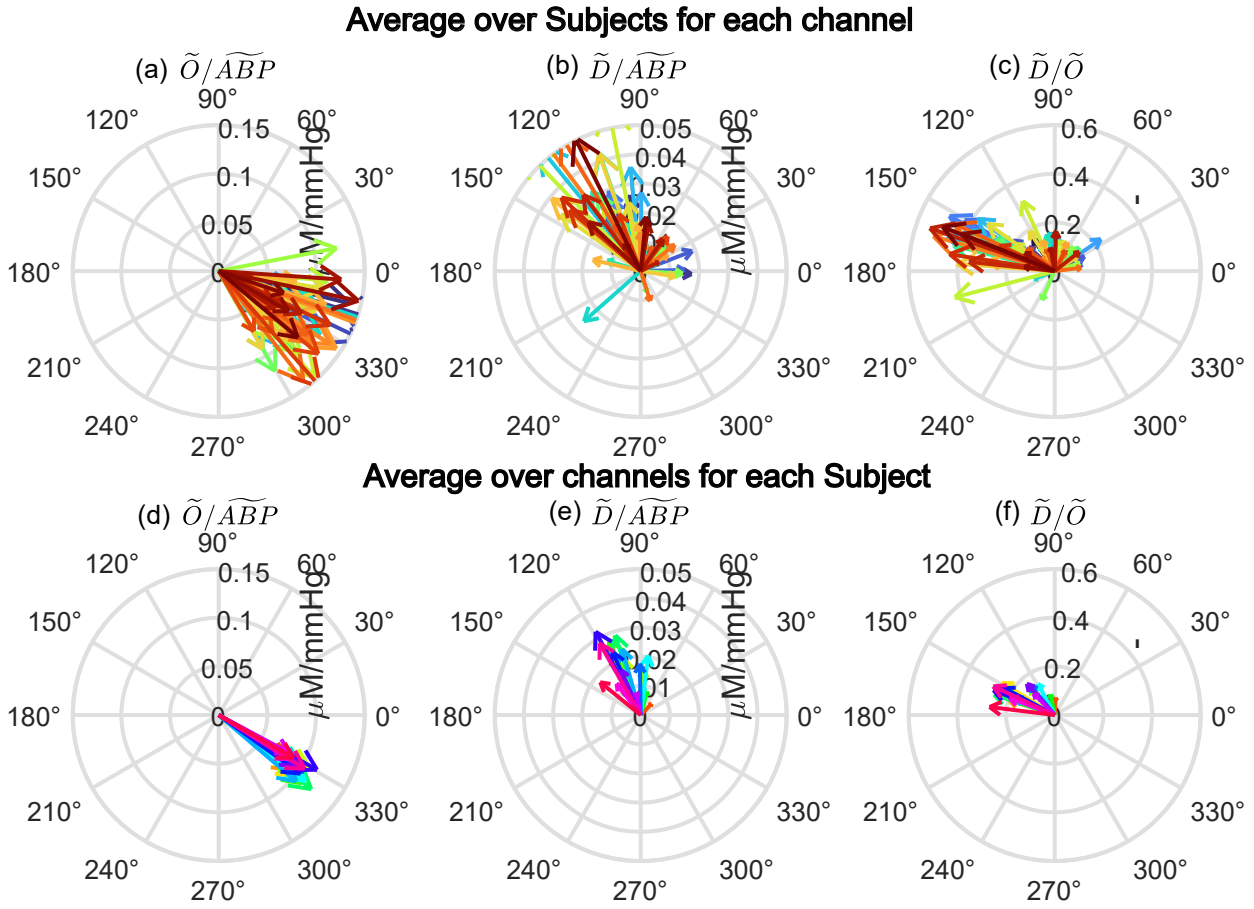

Figure 5.5: Average phasor ratios for each subject (a,b, and c) at 0.1 Hz where each arrow represents one subject(78 possible) and the average phasor ratios over subjects for each channel (d, e, and f) where each arrow represents one channel (20 possible).(a) and (d) show the phasor ratio vector between Oxy-hemoglobin and Arterial blood pressure ($\widetilde{O}/\widetilde{ABP}$), (b) and (e) show the phasor ratio vector between Deoxy-hemoglobin and Arterial blood pressure ($\widetilde{D}/\widetilde{ABP}$), and (c) and (f) show the phasor ratio vector between Deoxy-hemoglobin and Oxy-hemoglobin ($\widetilde{D}/\widetilde{O}$).

The average over channels, subjects, and sessions for $\widetilde{O}/\widetilde{ABP}$, $\widetilde{D}/\widetilde{ABP}$, and $\widetilde{D}/\widetilde{O}$ is shown in Figure 5.6(a), (b), and (c), allowing for an examination of the range among the population. The standard deviation for the phase difference was ∼30 deg for $\widetilde{O}/\widetilde{ABP}$, 60 deg for $\widetilde{D}/\widetilde{ABP}$, and 70 deg for $\widetilde{D}/\widetilde{O}$. For the amplitude ratio, $|\widetilde{D}/\widetilde{ABP}|$ had the lowest standard deviation of 0.03 µM mmHg^{-1}, while it was 0.06 µM mmHg^{-1} for $|\widetilde{O}/\widetilde{ABP}|$.

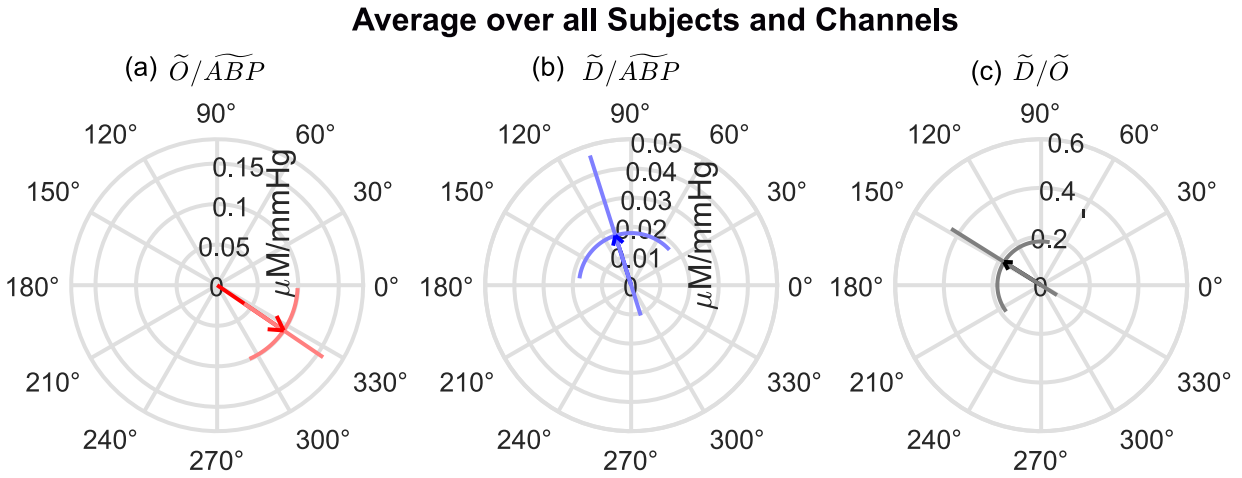

Figure 5.6: Average phasor ratio across 78 subjects, 20 channels and 2 sessions at baseline for (a) the phasor ratio vector between Oxy-hemoglobin and Arterial blood pressure ($\widetilde{O}/\widetilde{ABP}$), (b) the phasor ratio vector between Deoxy-hemoglobin and Arterial blood pressure ($\widetilde{D}/\widetilde{ABP}$), (c) the phasor ratio vector between Deoxy-hemoglobin and Oxy-hemoglobin ($\widetilde{D}/\widetilde{O}$).

5.3.3 Average Phasor Ratios between Blocks

Figure 5.7 reports the average phasor ratios across all subjects, sessions, and channels for the 6 Blocks (BLs). Braking events occurred randomly for every subject/session, and due to their approximate timing during the experiment it was assumed that at least one event occurred during each block. The average phasor ratios for $\widetilde{O}/\widetilde{ABP}$, $\widetilde{D}/\widetilde{ABP}$, and $\widetilde{D}/\widetilde{O}$ for each block (denoted by a different color) are shown in Figure 5.7. All phasor ratios lie within the standard deviations and overlap, showing no difference between all 6 BLs. Table 5.1 reports the average amplitude ratio and phase difference with the standard deviation for each block, where BL 1 is the baseline. $\widetilde{O}/\widetilde{ABP}$ showed the smallest deviation between the blocks and overall variability.

5.4 Discussion

An in-depth analysis was performed to evaluate the amount of time with coherent hemodynamics at frequencies between 0.01 Hz to 1.5 Hz driven by spontaneous oscillations in ABP.

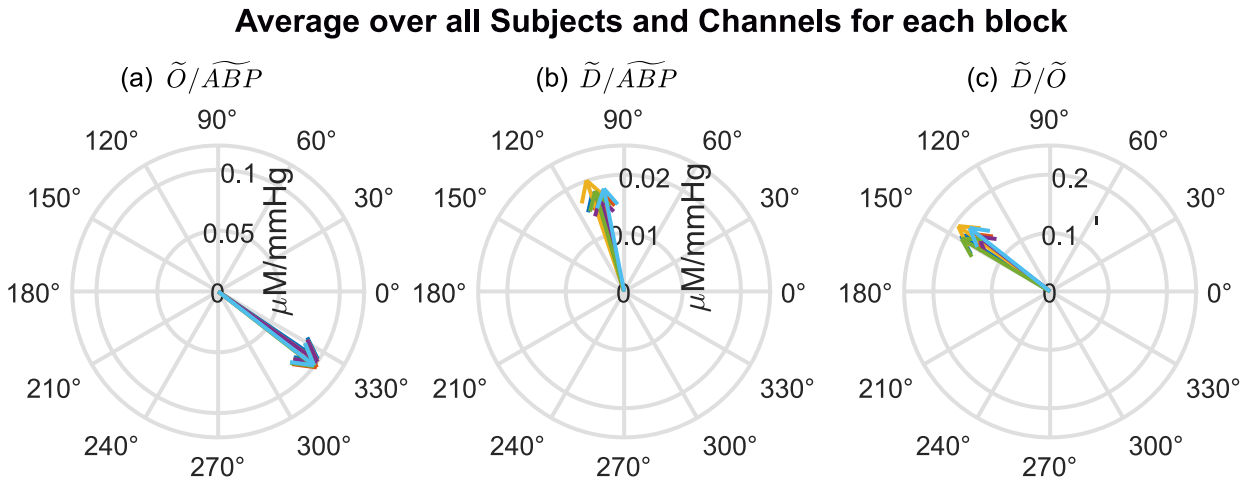

Figure 5.7: Average phasor ratio across 78 subjects, 20 channels and 2 sessions for each of the six blocks for (a) the phasor ratio vector between Oxy-hemoglobin and Arterial blood pressure ($\widetilde{O}/\widetilde{ABP}$), (b) the phasor ratio vector between Deoxy-hemoglobin and Arterial blood pressure ($\widetilde{D}/\widetilde{ABP}$), (c) the phasor ratio vector between Deoxy-hemoglobin and Oxy-hemoglobin ($\widetilde{D}/\widetilde{O}$). Each block is a 3 min non-overlapping interval during the experiment starting from 0 min to 18 min, where 0 min to 18 min was baseline.

The heart rate showed the highest amount, which has previously been reported,[137] and is expected due to arterial pulsation contributions to ΔO measurements. The lower fraction of time from ΔD can be explained by the small ΔD signal (and thus small signal-to-noise ratio) originating from the arteries due to high oxygen saturation of arterial blood.

For LFOs, ∼0.1 Hz showed the highest fraction of time with coherence for $\widetilde{O}/\widetilde{ABP}$, $\widetilde{D}/\widetilde{ABP}$, and the logical AND between $\widetilde{O}/\widetilde{ABP}$ and $\widetilde{D}/\widetilde{ABP}$ (Figure 5.4). A peak at ∼0.1 Hz has previously been shown [137, 146]. This frequency is associated with Mayer waves, which are linked with spontaneous oscillations in ABP and oscillations in sympathetic nerve activity [141]. These systemic oscillations drive cerebral hemodynamics and account for the high coherence observed. Previous studies considered a low number of subjects (3 and 13, respectively [137, 146]), while the results presented in Figure 5.4 allow for examination of variability across the 78 subjects, 2 sessions, and 20 channels. This study shows the promise of using spontaneous oscillations for CHS given that in 3 min, on average, 30 % of time features coherent cerebral hemodynamics at 0.1 Hz in as many as half of the NIRS channels

Table 5.1: Average Amplitude Ratio and Phase Difference for Each Block.

BL -	$\lvert\widetilde{O}/\widetilde{ABP}\rvert$ (μM mmHg^{-1})	$\angle\widetilde{O}/\widetilde{ABP}$ deg	$\lvert\widetilde{D}/\widetilde{ABP}\rvert$ (μM mmHg^{-1})	$\angle\widetilde{D}/\widetilde{ABP}$ deg	$\lvert\widetilde{D}/\widetilde{O}\rvert$ -	$\angle\widetilde{D}/\widetilde{O}$ deg
1	0.10 ± 0.06	-30 ± 30	0.02± 0.03	110 ± 60	0.2 ± 0.6	150 ± 70
2	0.10 ± 0.06	-40 ± 30	0.02± 0.03	100 ± 70	0.2 ± 0.2	140 ± 70
3	0.10 ± 0.06	-40 ± 30	0.02± 0.03	110 ± 70	0.2 ± 0.3	140 ± 70
4	0.1 ± 0.06	-40 ± 30	0.02± 0.03	100 ± 70	0.2 ± 0.3	140 ± 70
5	0.1 ± 0.06	-40 ± 30	0.02± 0.04	110 ± 70	0.2 ± 0.4	150 ± 70
6	0.1 ± 0.06	-40 ± 30	0.02± 0.03	100 ± 70	0.2 ± 0.3	140 ± 70

Acronyms:Oxy-hemoglobin phasor ($\widetilde{O}$), Deoxy-hemoglobin phasor ($\widetilde{D}$), Arterial blood pressure phasor ($\widetilde{ABP}$), Block (BL)

used in this study.

Spontaneous and induced oscillations at 0.1 Hz have been used in combination with NIRS [31, 137, 144] to study the relationship between hemodynamics and ABP. In this study, $\widetilde{D}/\widetilde{O}$ had an average amplitude ratio ($\sim$0.18) and phase difference (~ -212 deg) that aligns with reported results on 5 subjects with repeated induced oscillation measurements at 0.1 Hz and 30 mm source-detector separation [127]. The mean phase difference for all phasor ratios aligned with reported results on healthy human subjects [31, 123].

The phase difference for $\widetilde{O}/\widetilde{ABP}$ had the lowest standard deviation in all blocks (Table 5.1). Higher variability in $\widetilde{D}/\widetilde{ABP}$ and $\widetilde{D}/\widetilde{O}$ can be explained by their sensitivity to changes in blood flow, a higher sensitivity to blood volume changes in superficial tissue, and a lower signal-to-noise associated with measurements of ΔD. Assuming a constant $\widetilde{O}/\widetilde{ABP}$, a relative increase in blood volume contributions versus blood flow contributions to the optical measurements would shift $\widetilde{D}/\widetilde{ABP}$ towards $\widetilde{O}/\widetilde{ABP}$ and cause a decrease in its amplitude [146]. This result was seen for $\widetilde{D}/\widetilde{ABP}$ over subjects (Figure 5.5(b)) and could explain the larger variability as the contribution of blood volume to the optical signal differed for each subject. One parameter that was not taken into account is a varying skull thickness across the subject population, which has an effect on the amount of optical signal that probes the brain. Previous work has shown more blood flow-driven oscillations as source-detector

distance increases [146] (i.e., measurement sensitivity to the brain becoming larger) and sensitivity to changes in the brain as skull thickness changes [92].

Spatial averages (Figure 5.5(d), (e), and (f)) showed no significant qualitative differences between channels suggesting spatially uniform cerebral hemodynamics associated with systemic changes in ABP [152, 153]. Variability among the subjects (Figure 5.5(a), (b) , and (c)) was larger than across the channels and indicated that subjects might be separable from each other resulting from individual cerebrovascular or anatomical features.

Comparison between baseline and other blocks that involved a braking task showed no qualitative significant difference (Figure 5.7). This lack of difference implies no detectable changes in the relative dynamics of cerebral hemodynamics and ABP during the driving events. Previous work showed an increase in the wavelet coefficient amplitude between straight driving and driving mixed with tasks in the frequency range of 0.0095 Hz to 0.021 Hz on the pre-frontal cortex[154] but not at the frequency band including 0.1 Hz for ΔO which aligns with presented results. Previous work has shown a signature of brain activation driving tasks [7], and it was hypothesized that the braking scenarios would elicit this response. Evaluation of the hemoglobin traces during these events showed no signs of activation during either real or fake braking over all subjects, channels, and sessions. The lack of difference can be attributed to no activation due to this specific task or contributions from scalp hemodynamics, as Single-Distance Intensity (SDI) measurements are highly sensitive to superficial tissue. This result implies the importance of the use of data types more sensitive to the brain during cognitive tasks, such as the Dual-Slope (DS) or phase (ϕ) measurements.

5.5 Conclusion

Cerebral hemodynamics coherent with systemic ABP provide indications of the health of cerebral perfusion and Auto-Regulation (AR) [19, 123, 155]. Measurements of cerebral hemodynamics (specifically, Oxy-hemoglobin (O) and Deoxy-hemoglobin (D)) with NIRS

are non-invasive and reflect blood volume, blood flow, and rate of oxygen delivery to tissue at the micro circulation level [16, 123]. This work has shown that NIRS can measure spontaneous cerebral hemodynamic oscillations in the AR frequency range of 0.1 Hz that show a significant coherence and meet strict requirements with ABP for about 10 % to 20 % of the measurement time. This result means that spontaneous coherent hemodynamics can be measured with NIRS to evaluate cerebral perfusion health and efficiency of cerebral AR, at least when measurements can be performed over a time of at least a few minutes and physiological conditions remain stable during this period. Another implication of this work is that CHS [91, 95] may be based on spontaneous rather than induced ABP and cerebral hemodynamic oscillations, provided that proper care is taken in identifying significant levels of coherence which is needed to ensure changes in ABP are the driving forces for the hemodynamic changes. The possibility of relying on spontaneous hemodynamics rather than induced hemodynamics has important practical implications as subjects would not be required to undergo physiological maneuvers or perturbations. Finally, the finding of a lack of significant effects from braking tasks on the relative amplitude and phase of coherent cerebral hemodynamics and ABP may be specific to this measurement protocol. Future work will involve functional brain activation with a variety of motor, visual, or cognitive workloads for a more thorough characterization of coherent cerebral hemodynamics during brain activation.

5.6 Acknowledgments and Contributions

Cristianne Fernandez, Tapan Das, Giles Blaney, Angelo Sassaroli, and Sergio Fantini are with the Department of Biomedical Engineering, Tufts University, Medford, MA, USA. Zachary Haga is with the Department of Computer Science, Tufts University, Medford, MA, USA. Julia Mertens and Thomas McWilliams are with the Department of Psychology, Tufts University, Medford, MA, USA. I would like to specifically thank Zachary Haga and Thomas McWilliams for their effort in the data collection on all subjects.

Chapter 6

Application in the NeuroCritical Care Unit

6.1 Introduction

Clinical translation of the methods utilized in Chapter 4 and Chapter 5 is key in demonstrating the potential impact of these techniques. Work in this chapter applies a Coherent Hemodynamics Spectroscopy (CHS) protocol in the NeuroCritical Care Unit (NCCU) at Tufts Medical Center to explore the feasibility of monitoring cerebral autoregulation on patients with brain injuries. Cerebral autoregulation (as described in Chapter 1) is a homeostatic feedback mechanism that maintains stable Cerebral Blood Flow (CBF) despite moderate changes in Arterial Blood Pressure (ABP). This mechanism utilizes the arteries and arterioles of the brain, that can dilate and constrict, to regulate CBF and limit its variability. In the NCCU, measurements of cerebral autoregulation in patients with traumatic brain injuries can help the diagnosis and monitoring of pathological conditions to improve patient care and to prevent further injury to the brain [156]. Impaired cerebral autoregulation is linked to poor clinical outcomes in a variety of conditions such as subarachnoid hemorrhage, stroke, traumatic brain injury, etc. [157–159].

Assessment of dynamic cerebral autoregulation has been widely investigated with the use of Transcranial Doppler ultrasound (TCD) by evaluating the relationship between measured cerebral blood flow velocity and ABP [88, 142, 160]. Dynamic changes in ABP can be spontaneous (as shown in Chapter 5) or induced using protocols such as thigh cuff oscillations (as shown in Chapter 4) and paced breathing [18, 142, 161]. A transfer function analysis is performed to quantify the relationship between ABP (input, as monitored simultaneously by finger plethysmography) and CBF (output, as monitored by TCD). A more positive phase shift between CBF versus ABP (i.e., a faster recovery of CBF in response to ABP changes) is often associated with effective cerebral autoregulation [18, 123, 143, 162]. This technique has been applied in the clinical setting to assess cerebral autoregulation in patients with intracranial hypertension [160], traumatic brain injury [163], acute ischemic stroke [14, 164], carotid artery occlusive disease [88, 123], intracranial hemorrhage [159]. It was shown that a higher correlation coefficient [159] and a smaller phase difference [14] between CBF and ABP implies worsening autoregulation in those patients.

This chapter aims to demonstrate the feasibility of using Near-InfraRed Spectroscopy (NIRS) measurements with a protocol based on blood-pressure-induced hemodynamic oscillations to monitor cerebral autoregulation efficiency in patients with brain injuries. In the sample of NCCU patients, results from a healthy subject population in Pham and Fernandez *et al* (2021) [19] guide the clinical interpretation of three patients.

6.2 Methods

6.2.1 Study Protocol and Data Acquisition

A total of 3 patients (one female, two males, age range: 17 yr to 67 yr) in the NCCU participated in a Tufts University approved Institutional Review Board (IRB) for Frequency-Domain (FD)-NIRS measurements during systemic ABP oscillations. The NCCU patients were recruited from Tufts Medical Center, and a summary of patient demographic infor-

mation can be found in Table 6.1. All patients signed an informed consent prior to the experiment. For the NCCU patients, patient 1 participated on three days, patient 2 on two days, and patient 3 on one day. Each day, the measurement session was repeated three times. Here, the results for a single day and measurement session are reported. These measurements were selected based on low motion artifacts, a high signal-to-noise ratio of the optical data, and maximum extent of induced oscillations in ABP and cerebral hemodynamics.

Table 6.1: Summary of patient information from NeuroCritical Care Unit (NCCU). Values are reported as median [25%, 75% quartiles] over the entire experimental time trace.

Patient	Age	Sex	Cuff Pressure (mmHg)	ICP (mmHg)	MAP (mmHg)	CPP (mmHg)	Clinical Diagnosis
1	61	M	180	12 [11,14]	82 [80, 84]	69 [66,73]	Left basal ganglia hemorrhage extending out to subcortical and parietal area, cerebral edema, ventricular effacement
2	67	M	150	0 [−1,1]	81 [79,85]	81 [78,85]	Isolated IVH of unclear etiology with no apparent brain tissue injury, Hydrocephalus
3	17	F	170	10 [10,11]	73 [68,77]	63 [58,67]	Left occipital AVM with IVH, AVM involves posterior circulation

Acronyms: Male (M), Female (F), IntraCranial Pressure (ICP), Mean Arterial Pressure (MAP), Cerebral Perfusion Pressure (CPP), Cerebral Perfusion Pressure (CPP), Intra-Ventricular Hemorrhage (IVH), ArterioVenous Malformation (AVM)

Figure 6.1(b) depicts the experimental setup for patients in the NCCU used to induce systemic ABP oscillations. Firstly, two pneumatic thigh cuffs were wrapped around the subject's thighs and were connected to an E-20 Rapid Cuff Inflation System, D.E. Hokanson, Inc [Bellevue, WA USA] (automatic cuff inflation system) that ran the experimental protocol and controlled the pressure in the cuffs. The air pressure in the thigh cuffs was monitored by a Series 626 Pressure Transmitter Dwyer Instruments Inc [Michigan City, IN USA] (digital manometer). The maximum pressure was set to be above systolic blood pressure, specifically between 150 mmHg to 180 mmHg (reported in Table 6.1) for the NCCU patients. This value was dependent on individual blood pressure and the physician's recommendation. The pneu-

matic thigh cuffs were inflated smoothly to maximum pressure, which took approximately 4 s.

FD-NIRS measurements were performed using an ISS OxiplexTS [Champaign, IL USA] (wavelengths: 690 nm and 830 nm; modulation frequency: 110 MHz) at a sampling rate of 12.5 Hz. The optical probe was placed on the left side of the patient's forehead. The probe consisted of one detector fiber bundle and four separate source fiber pairs, with source-detector distances of 20 mm, 25 mm, 30 mm and 35 mm (Figure 6.1(a)). The optical system was calibrated using a phantom of known optical properties, allowing for absolute measurements of tissue optical properties. Non-invasive ABP measurements were acquired with an NIPD100D BIOPAC Systems [Goleta, CA USA] (beat-to-beat finger plethysmography system).

The experimental protocol consisted of 5 min baseline, 2 min cyclic thigh cuff inflation and deflation at a frequency of 0.063 Hz, and 5 min of recovery. Figure 6.2(a) shows a typical experimental time trace for the measured pneumatic cuff pressure signal, and Figure 6.2(b) reports the time traces of ABP. Here, oscillations in ABP can be visually seen, with an average amplitude of 10 mmHg [93].

6.2.2 Measurements of Relative Hemoglobin Concentrations

Tissue optical properties at baseline, namely the absorption coefficient (μ_a) and the reduced scattering coefficient (μ_s'), were obtained at the two wavelengths using the calibrated Multi-Distance (MD) method (described in section 2.2). The μ_a and μ_s' solved using an iterative approach on the NIRS Intensity (I) and phase (ϕ) data collected at baseline. A full description of this iterative technique can be found in Blaney *et al* (2021) [98]. Changes in I and ϕ for Single-Distance (SD) and Single-Slope (SS) were calculated using methods described in 2.3 using the absolute optical properties during baseline to calculate the Differential Pathlength Factor (DPF) and Differential Slope Factor (DSF).

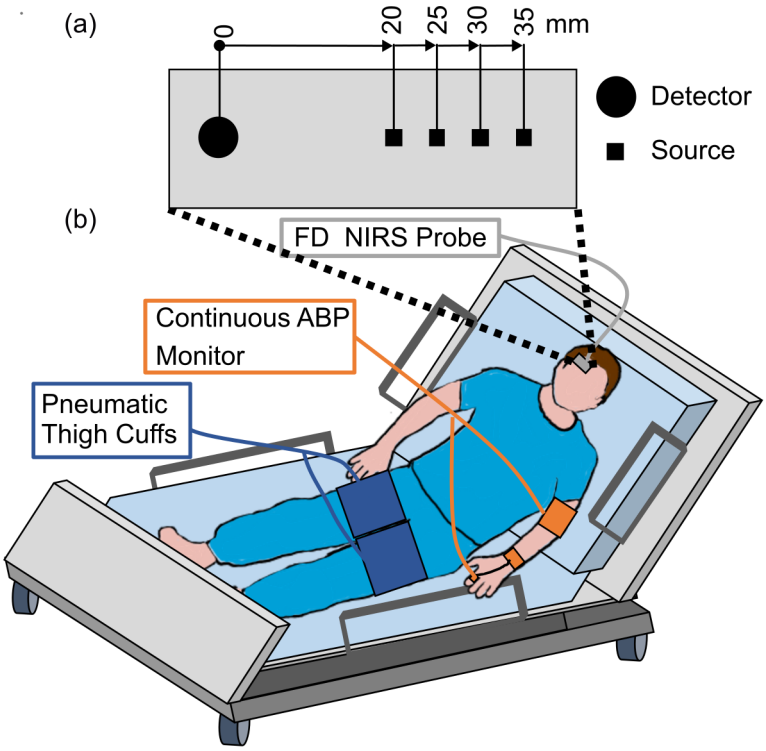

Figure 6.1: Experimental setup and schematic diagrams of the optical probes used for Neuro-Critical Care Unit (NCCU) patients. (a) The optical probe was placed on the left side of the forehead and it featured four source-detector distances of 20 mm, 25 mm, 30 mm and 35 mm in a multi-distance configuration. The clinical setup included the optical probe, NIPD100D BIOPAC Systems [Goleta, CA USA] (beat-to-beat finger plethysmography system), and pneumatic thigh cuffs wrapped around both thighs as depicted in (b).

6.2.3 Wavelet Coherence and Phasor Analysis

Transfer function analysis using Wavelet coherence and phasor analysis was performed to determine the phase differences and amplitude ratios of the coherent hemodynamic oscillations (i.e., oscillations in Oxy-hemoglobin concentration change (ΔO), and Deoxy-hemoglobin concentration change (ΔD)) versus ABP oscillations within the interval of the thigh cuff inflation-deflation oscillations. The Continuous Wavelet Transform (CWT) with a complex Morlet mother wavelet was used to get maps of Oxy-hemoglobin phasor ($\widetilde{O}$), Deoxy-hemoglobin phasor ($\widetilde{D}$), and Arterial blood pressure phasor ($\widetilde{ABP}$) in time (t) and frequency (f). The phasor ratio maps for the phasor ratio vector between Oxy-hemoglobin and Arterial blood pressure ($\widetilde{O}/\widetilde{ABP}$) and the phasor ratio vector between Deoxy-hemoglobin and

Arterial blood pressure ($\widetilde{D}/\widetilde{ABP}$) were then computed for each patient, data type and source-detector arrangement. Next, coherence maps of the Coherence between the Oxy-hemoglobin and Arterial blood pressure phasors ($COH(\widetilde{O}, \widetilde{ABP})$) and Coherence between the Deoxy-hemoglobin and Arterial blood pressure phasors ($COH(\widetilde{D}, \widetilde{ABP})$) were computed. A coherence threshold was then applied to each coherence map to create a boolean map of time-frequency pixels with statistically significant coherence. This boolean map was then applied to each phasor ratio map. The coherence threshold map was generated from random surrogate data [150, 151] at $\alpha = 0.05$ significance level.

After applying the coherence threshold, we only considered the average $\widetilde{O}/\widetilde{ABP}$ and $\widetilde{D}/\widetilde{ABP}$ with significantly high coherence within the time intervals of the thigh cuff oscillation and a frequency band centered at the central frequency of the induced oscillation. Here, the central frequency was 0.063 Hz with a bandwidth of five frequencies in the range of 0.055 Hz to 0.074 Hz (as determined by the half power bandwidth of a simulated test sinusoidal signal). Further criteria required continuous coherence longer than one period of the central frequency and at least two continuous frequency bands (where one is the central frequency). Here, the argument of the phasor ratio is focused on and represents the phase difference between the two phasors.

6.3 Results on 3 Clinical Patients

Figure 6.2 presents representative time traces of ΔO and ΔD calculated with Single-Distance Intensity (SDI) (c) and Single Distance phase (SDϕ) (d) at a source-detector distance (ρ) of 35 mm, as well as Single-Slope Intensity (SSI)(e) using ρs at 25 mm and 35 mm . In this work, we focus on the relationship between ABP (shown in Figure 6.2(b)) and both ΔO and ΔD.

Figure 6.3 reports the relative phase of $\widetilde{D}$ versus $\widetilde{ABP}$ (panel (a)) and $\widetilde{O}$ versus $\widetilde{ABP}$ (panel (b)) for the three NCCU patients. Results are shown for the phasor ratios calculated

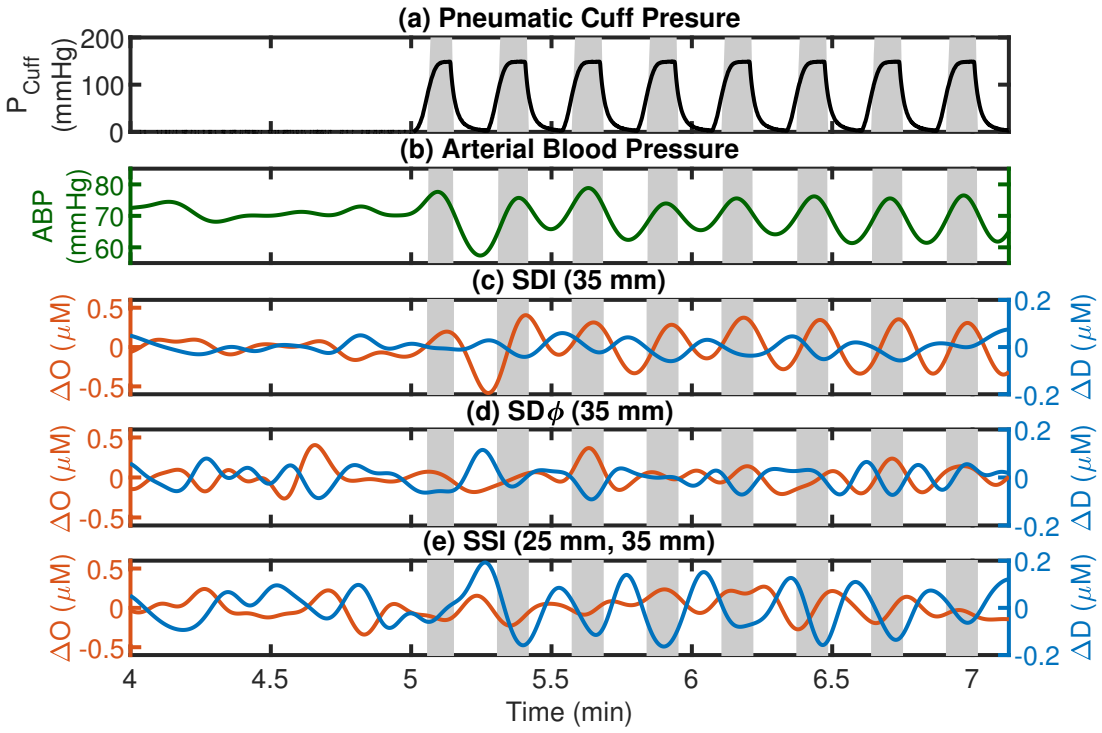

Figure 6.2: Representative time traces of data collected on one NeuroCritical Care Unit (NCCU) patient (patient 2). Signals are shown for pneumatic thigh cuff pressure (P_{CUFF}) in (a), Arterial Blood Pressure (ABP) in (b), and for Oxy-hemoglobin concentration change (ΔO) and Deoxy-hemoglobin concentration change (ΔD) measured with Single-Distance Intensity (SDI) (c), Single Distance phase (SDϕ) (d), and (e) Single-Slope Intensity (SSI).

with SDI data at a ρ of 35 mm, SDϕ data at ρ of 35 mm, and SSI data with ρs at 25 mm and 35 mm. The relative phase of $\widetilde{D}/\widetilde{ABP}$ and $\widetilde{O}/\widetilde{ABP}$ are reported here as work on a subset of healthy subjects showed these parameters as most sensitive to autoregulation changes [19]. The amplitude ratio showed no change due to a change in autoregulation, and in turn is not reported here.

It should be noted that the results of Figure 6.3 allow for a patient-by-patient comparison, but the number of patients (three) is too small to draw general conclusions. Additionally, we lack an independent measurement of cerebral autoregulation in each subject and cannot make a definite statement on reproducibility among trials in individual patients due to a lack of clean data for all three patients. Patients 1 and 3 had high-quality data for only one day and trial, whereas patient 2 had multiple trials with acceptable data quality in a given

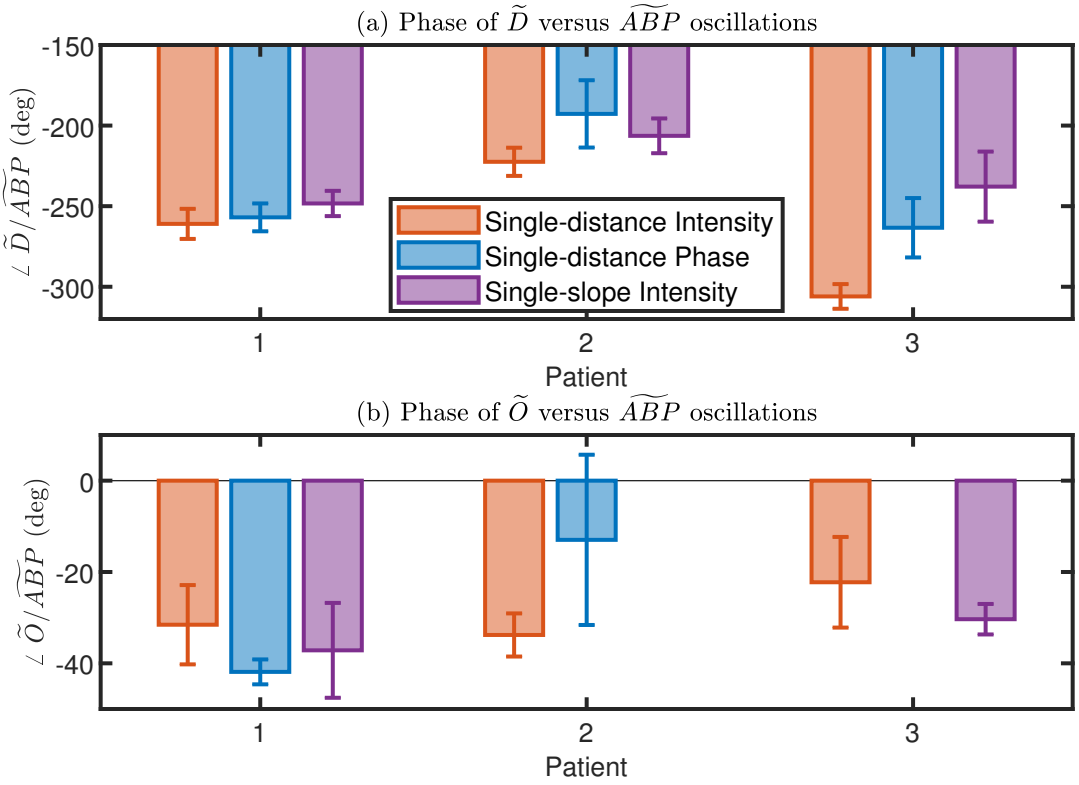

Figure 6.3: Relative phase of the phasor ratio vector between Deoxy-hemoglobin and Arterial blood pressure ($\widetilde{D}/\widetilde{ABP}$) (a) and phasor ratio vector between Oxy-hemoglobin and Arterial blood pressure ($\widetilde{O}/\widetilde{ABP}$) (c) for oscillations at 0.063 Hz in 3 NeuroCritical Care Unit (NCCU) patients measured with Single-Distance Intensity (SDI), Single Distance phase (SDϕ), and Single-Slope Intensity (SSI). Error bars represent the standard errors of the measurements. Data for SDϕ in patient 3 and SSI in patient 2 are missing due to a coherence level below the threshold.

day. The inter-trial variability of the relative phase of $\widetilde{D}/\widetilde{ABP}$ in patient 2 was smaller than the inter-patient differences reported in Figure 6.3(a). However, more work needs to be done to better characterize intra-patient and inter-patient variability in these noninvasive optical measurements of cerebral hemodynamics. Nevertheless, these results allow us to report the technical feasibility of NIRS measurements of cerebral oscillatory hemodynamics that are coherent with ABP. Furthermore, the measurements on healthy subjects during normocapnia and hypercapnia (reported in Pham and Fernandez *et al* (2021) [19]) provide a key reference to read and interpret the results observed in the NCCU patients in relation to different levels of cerebral autoregulation.

Work reported in Pham and Fernandez *et al* (2021) [19] (specifically Figure 3) showed that impairment of cerebral autoregulation (during hypercapnia) results in a more negative relative phase of $\widetilde{D}/\widetilde{ABP}$ as compared to normocapnia. In the NCCU patients (Figure 6.3(a)), we observe a less negative phase of $\widetilde{D}/\widetilde{ABP}$ (with all measurements: SDI, SDϕ, SSI) in patient 2 compared to patients 1 and 3, suggesting better autoregulation in patient 2. The phase between $\widetilde{O}$ and $\widetilde{ABP}$ also became more negative with impaired autoregulation in healthy subjects. The results for the relative phase of $\widetilde{O}$ versus $\widetilde{ABP}$ in the NCCU (Figure 6.3(b)) were not as clear as those for the relative phase of $\widetilde{D}$ versus $\widetilde{ABP}$. This was due to a lack of some data (due to low coherence) for SDϕ in patient 3 and SSI in patient 2 as well as opposite results for SDI (more negative phase for patient 2) and SDϕ (less negative phase for patient 2). This result is in line with the smaller impact of autoregulation changes in the phase of $\widetilde{O}$ versus $\widetilde{ABP}$ than $\widetilde{D}$ versus $\widetilde{ABP}$ in the data from healthy subjects. These results may be a consequence of incoherent hemodynamics contributions from the arterial compartment in scalp tissue.

6.4 Discussion

This pilot clinical study on NCCU patients demonstrated the proof of concept and technical feasibility of applying a protocol involving induced oscillations in ABP and associated coherent cerebral hemodynamic oscillations in a clinical setting. The non-invasive measurement of these coherent cerebral hemodynamics with FD-NIRS techniques, in conjunction with well-defined criteria for the required levels of coherence with ABP, allows for the measurement of quantities that are sensitive to the degree of dynamic cerebral autoregulation. The representative results reported here on three NCCU patients suggest better cerebral autoregulation conditions for patient 2 compared to patients 1 and 3 based on the relative phase of $\widetilde{D}$ versus $\widetilde{ABP}$. The values of the relative phase of $\widetilde{D}$ versus $\widetilde{ABP}$ for patient 2 are also within the range observed in healthy subjects ($-222\,\text{deg}$ to $-192\,\text{deg}$) across methods

for patient 2, and for healthy subjects (-214 deg to -208 deg as reported in Pham and Fernandez *et al* (2021) [19])). This is bolstered by the fact that patient 2 recorded the lowest IntraCranial Pressure (ICP) value and highest Cerebral Perfusion Pressure (CPP) value over the time of the trial compared to the other two patients, as reported in Table 6.1. A higher ICP value is associated with decreased intracranial compliance, which can lead to lower CPP [165]. Clinically, this could be a manifestation of poor cerebral autoregulation [159] resulting in reduced CBF [166]. Higher ICP values in patients with a traumatic brain injury have previously been shown to be associated with poorer dynamic autoregulation [160], which alludes to the potential for patient 2 to have better autoregulation compared to the other two patients. The clinical diagnosis between patients (Table 6.1) indicates that patient 2 had no apparent brain injury and had an intraventricular hemorrhage that caused an obstruction of cerebral spinal fluid (CSF) flow. On the other hand, patient 1 had a large hemorrhage in the left frontal and parietal lobes, and patient 3 had a left occipital hemorrhage, both of these causing a larger brain injury than in patient 2. This larger brain damage in patients 1 and 3 compared to patient 2 can potentially explain the results.

The current clinical gold standard for monitoring traumatic brain injury is the use of invasive ICP monitoring which requires surgical implantation which can lead to added risks. A non-invasive method that can allow for real time monitoring of cerebral health can be extremely valuable in the clinical setting in a brain injured patient. Here we have utilized NIRS during a CHS protocol for the assessment of cerebral autoregulation, which is connected to the traditionally measured ICP. This link between impaired cerebral autoregulation, a decreased cerebral blood flow (given a decrease cerebral perfusion pressure and constant Mean Arterial Pressure (MAP)), and a higher ICP is the key in the implementation of the technique. The non-invasive metric of cerebral autoregulation determined by the techniques presented here could be a powerful tool for monitoring the disease course after injury and potentially eliminate the need for invasive ICP measurements.

6.5 Conclusions

The pilot clinical study presented here demonstrated the feasibility of measuring coherent ΔD and ABP oscillations to assess autoregulation in the NCCU. Clinical measurements taken here were collected by a previous graduate student. Recent collection of data in the NCCU has been stunted due to COVID and difficulty in subject recruitment. Since 2019, a total of 3 subjects have been recruited. Out of these 3 subjects, a total of 2 had FD-NIRS measurements taken. Studies on these subjects implemented the Dual-Slope (DS) arrangement with the goal of measuring hemodynamics mostly associated with deeper tissue, as well as limiting motion and coupling artifacts that can be due to clinical care occurring during NIRS measurements. Future studies will target a more complete characterization of the depth sensitivity of various data types of FD-NIRS measurements in heterogeneous tissue, especially in this protocol of systemic blood pressure oscillations, and applications to clinical scenarios with a larger sample size.

6.6 Acknowledgments and Contributions

Those who worked on this research include Thao Pham, Giles Blaney, Kristen Tgavalekos, Angelo Sassaroli and Sergio Fantini from the Department of Biomedical Engineering at Tufts University and Xuemei Cai, Steve Bibu, and Joshua Kornbluth from the Department of Neurology at Tufts University School of Medicine. This research is supported by the National Institutes of Health, Grant No. R01-NS095334. We also acknowledge support from the Neuroscience and Pain Research Unit at Pfizer Inc. and from the National Institutes of Health, Grant No. R21-EB020347, for the collection of data from patients in the neurological critical care unit. I would like to specifically thank Kristen Tgavalekos who collected the data presented here in the NCCU.

Chapter 7

Future Directions

Near-InfraRed Spectroscopy (NIRS) is an exciting tool for the non-invasive assessment of both skeletal muscle and brain hemodynamics and has seen growth in both the technology and applications over the last 30 yr. The ability for real-time, non-invasive measurements makes NIRS incredibly useful in the clinical setting. To make NIRS a reliable clinical tool, much work is needed in calibration and standardization across data collection and processing methods to allow for robust measurements of metrics sensitive to cerebral Auto-Regulation (AR), cerebral Blood Flow (BF), muscle BF, muscle Oxygen Consumption (OC), etc. Increasing robustness of dynamic measurements should include the use of absolute optical properties measured per subject, which implies the use of Frequency-Domain (FD) or Time-Domain (TD) modalities. Implementation of FD and TD clinically can have a large benefit in increasing robustness and providing quantitative metrics. Work presented in this dissertation showed the potential of the Dual-Slope (DS) technique in limiting the effect of superficial signals NIRS measurements, overall increasing the robustness. Standardization of source-detector arrangements and distances, assumptions made, and processing methodologies will allow for findings from multiple groups to be directly comparable and for building of large data sets.

Recruitment of large population of healthy and clinical subjects is the next step in vali-

dating the methods presented in this dissertation, but it can prove challenging. One limiting factor has been the comfort level of the optical probes, as they typically require force to ensure good contact between the optodes and skin. Applying force to ensure good contact between the tissue and the optodes has been particularly challenging in the NeuroCritical Care Unit (NCCU). An advance in probe design is needed to move studies in the NCCU on those with a traumatic brain injury forward. Commercial implementations of NIRS instruments have designed optical probes, but these do not allow for customization of source and detector positions that can be valuable for research purposes. Requiring the use for physical perturbations during study protocols has proven to be another challenge in subject recruitment. The promising results on spontaneous oscillations in Chapter 5 opens the door for limiting the use of physiological perturbations for the assessment of cerebral AR in the clinical setting on those with a traumatic brain injury.

7.1 The Use of Spontaneous Oscillations

The non-invasive assessment of cerebral AR is largely applicable in patients with traumatic brain injury to prevent secondary injury [38]. Spontaneous oscillations can increase the clinical translatability of the Coherent Hemodynamics Spectroscopy (CHS) method leading to the possibility of real-time continuous monitoring of cerebral AR at the bedside. Spontaneous oscillations allow for long-term continuous monitoring, which can be an invaluable tool in preventing secondary injury. Due to no need for specific perturbations, metrics of cerebral AR can be calculated over periods of hours or days continually. The ability for these non-invasive continuous metrics allows for home monitoring an extended period of time after initial injury or monitoring the progression of healing post injury.

Perturbing Arterial Blood Pressure (ABP) through the use of pneumatic thigh cuffs that oscillate between 0 mmHg to 200 mmHg have been utilized throughout this work (Chapter 4 and Chapter 6). While ABP oscillations via pneumatic thigh cuffs were throughout this

work but there are various protocols for inducing ABP oscillations. These protocols include paced breathing [91, 161], body maneuvers [167, 168], and oscillatory negative body pressure [169]. Inducing changes in ABP with cyclic cuff inflation has been utilized due to its limited need for subject involvement (as in paced breathing), minimization of motion artifacts due to limited subject movement, and simplicity of implementation. Limiting subject involvement is beneficial as protocols such as paced breathing can be subjective and introduce a level of variability intrinsically linked to the subject population. Cyclic cuff inflation decreases this variability as the pressure and timing are controlled automatically and are consistent across subjects, adding robustness to the oscillations.

As mentioned previously, thigh cuff oscillations are not feasible in specific populations and can result in a lengthy protocol when multiple frequencies are desired [89]. Lengthy protocols increase the difficulty of subject recruitment, as it increases the time commitment and time in which the subject must be still. Remaining still can become increasingly difficult in a clinical setting as patients may be uncomfortable or clinical care needs to be performed during the study. Measurements done at the bedside in the hospital are aimed to not interfere with routine clinical care and, as such, are not stopped when care is given. This requires patients to be still for the study while receiving care, which may be difficult depending on the care being provided. One such protocol that was implemented in the NCCU was cyclic inflation and deflation of pneumatic thigh cuffs at 5 frequencys (fs) in the range of 0.05 Hz to 0.14 Hz where each oscillation frequency lasted for a total of 3 min with a 1 min rest between frequencies. The protocol above would last 19 min assuming no initial and end baseline periods. A protocol of this length innately requires a subject to sit without moving and with optical probes that may be uncomfortable for upwards of 20 min. One common issue during these lengthy protocols with multiple oscillation frequencies was keeping the pneumatic thigh cuffs secured as they began to slide down the participant's legs or become unsecured. The use of extra securing straps around the thigh cuffs was implemented successfully, but the abovementioned issues still occur during the protocols. Specifically, these issues are height-

ened at the end oscillation frequencies, as the cuffs become loose due to prolonged inflation and deflation. Participants have also reported that using the cyclically inflated and deflated pneumatic thigh cuffs can be uncomfortable and either ask to stop measurements or decrease inflation pressure. Thus, eliminating them could allow for the availability of more subjects. For these reasons, we have begun to explore the use of spontaneous oscillations in ABP.

Spontaneous oscillations in ABP that drive oscillations in cerebral hemodynamics have been utilized in NIRS [137, 170, 171] and Transcranial Doppler ultrasound (TCD) [172] measurements to assess cerebral AR. A prerequisite of utilizing spontaneous oscillations in ABP and cerebral hemodynamics is studying the coherence between the two parameters so that data when ABP is driving cerebral hemodynamics is used in analysis. Previous work comparing spontaneous and induced oscillations in the Oxy-hemoglobin (O) driven by ABP in measured with different source-detector arrangements [94] showed that spontaneous oscillations had a lower coherence than induced oscillations. In the range of physiologically relevant frequencies for assessing cerebral health (0.01 Hz to 0.1 Hz) [17, 141], the largest coherence between cerebral hemodynamics (namely Oxy-hemoglobin and Deoxy-hemoglobin (D)) and ABP is around 0.1 Hz. The peak at 0.1 Hz was shown in Obrig *et al* (2000) [137] and Kirilina *et al* (2013) [146] on 3 and 13, subject respectively, as well as in the work in Chapter 5 and Fernandez *et al* (2023) [147] on a total of 78 subjects. When evaluating the coherence, it is critical to define a threshold coherence value guided by statistical significance to decide if data should be kept or neglected in analysis. The work in Chapter 5 and Fernandez *et al* (2023) [147] showed that NIRS could measure spontaneous cerebral hemodynamic oscillations in the AR frequency range of 0.1 Hz that show a significant coherence and met defined coherence requirements for about 10 % to 20 % of the measurement time for cerebral hemodynamics and ABP in 78 subjects. The threshold for coherence here was 0.92, while typically reported coherence values are around 0.5 (coherence ranges from 0 to 1) [143]. While the coherence threshold applied in this work had a larger required coherence value it did not account for multiple comparisons, which should be explored.

Future work for implementing spontaneous oscillations with CHS studies should include the validation of recovered parameters utilizing spontaneous oscillations to those obtained with induced oscillations. Use of spontaneous oscillations does not require any physiological perturbations, so adding an extended baseline period to currently used protocols with cyclic cuff inflation is all that is needed to conduct these studies. Work in Chapter 5 utilized a 3 min baseline period and found available statistically significant coherent oscillations between the Oxy-hemoglobin concentration change (ΔO) and the Deoxy-hemoglobin concentration change (ΔD) with ABP for 10 % to 30 % of the time. This amount of coherent data was shown to give results that matched that of induced oscillation protocols [147]. On the other hand, Claassen *et al* (2016) [143] recommends a 5 min baseline period. Determining of the optimal baseline period length should be completed to find a baseline period that offers the largest information content with the lowest variation.

One protocol that would be advantageous to test spontaneous and induced oscillations is one that induces hypercapnia, which is a state of elevated CO_2 concentration that causes vasodilation of arterials and an increase in Cerebral Blood Flow (CBF) and impaired AR. Work utilizing induced oscillations and the processing methods used in Chapter 5 have been applied during hypercapnia [19] and showed the sensitivity of the phase difference between ΔO and ABP as well as ΔD and ABP to hypercapnia. Evaluating if the effect of hypercapnia occurs when utilizing spontaneous oscillations can demonstrate their ability to measure impaired AR. Validation of the sensitivity to spontaneous oscillations to impaired AR has a large application in the NCCU as it would allow for continuous measurements without needing physiological perturbations. The use of spontaneous oscillations also expands the number of fs that can be utilized with CHS for analysis with the hemodynamic model [95] which can provide physiologically relevant parameters that indicate cerebral AR.

7.2 Application of the Dual-Slope to Children During a Cognitive Task

Functional brain measurements using NIRS have seen an increase in their popularity and applications over the past 30 yr [40, 45, 173]. During that time, functional Near-InfraRed Spectroscopy (fNIRS) has been demonstrated in both behavioral and social studies [45] and has been applied to children during different cognitive tasks [174–176]. Studies have shown activation in the pre-frontal cortex during working memory tasks, cognitive shifting, and inhibitory control, as well as abnormal activation in children with developmental disorders [174]. The application of fNIRS to education has been applied for both math and language with an overall more pronounced activation when solving more complex problems or children with less expertise [177]. The portability and non-invasive manner of fNIRS makes it advantageous for studying cognitive development from an education point of view over traditionally used functional Magnetic Resonance Imaging (fMRI).

ScratchJr is a block programming application aimed at teaching young children (typically ages 5 yr to 7 yr) the basics of coding principals and computational thinking [178, 179]. The application introduces the concepts of sequences, loops, and conditionals that can be used to program tasks. ScracthJr is currently the most popular free programming language worldwide and is utilized at schools and home [179]. As this program becomes increasingly popular for the education of young children in school, fNIRS has the potential to be applied to measure brain activation during coding tasks of different difficulty levels. The hypothesis behind utilizing fNIRS during programming with ScracthJr is that increased blood flow (i.e., brain activation) will be linked to more complex tasks, as more challenging tasks increase cognitive strain on the subject. A Coding Stage Assessment (CSA) specific to ScracthJR [179] was utilized to screen participants and choose subjects within a specific range in the assessment. Questions were than chosen so that some were easy (below their CSA score) and some were hard (above their CSA score) to be used to evaluate brain activation at different

cognitive loads.

Preliminary studies utilizing FD-NIRS and ScratchJr have been completed on 6 healthy human adults and 4 first grade children with an ultimate goal of recruiting 50 first grade children at the end of the study. Multiple iterations of the experimental protocol have led to a protocol with four easy questions and four hard questions split into two sessions. Each session contains four alternating easy and hard questions where the subject has a total of 2 min to answer. Immediately after the subject deems they have completed the question, a 30 s rest begins. This finalized protocol limits the rest time, as keeping a child still for an extended period proved difficult. Measurements on children can be increasingly difficult due to their limited attention span, increased movement compared to adults, and their tendency not to listen to given directions. Initial indications from this study validated the selection of easy and hard questions, as subjects answered easy questions quicker than hard questions and had signs of brain activation while answering questions.

The contamination of hemodynamics from the scalp is a continuing issue in fNIRS measurements on both children and adults. Recent work utilizing the DS (specifically Dual Slope phase (DSϕ)) showed a larger activation signal associated with the brain as compared to traditionally used Single-Distance Intensity (SDI) [13] showing its promise for use in cognitive studies. Utilization of the DS during the coding tasks in ScracthJr has the potential to measure brain activation during easy and hard questions with a smaller contribution from scalp hemodynamics. Another advantage of DS is the cancellation of changes in optode coupling [30, 43], which can compensate for motion of the optical probe due to child movement. Future work includes recruiting a larger subject population and carefully analyzing the measured cerebral hemodynamics over the time the question is being answered as different cognitive skills are used to solve each question.

7.3 Implications for Skeletal Muscle Measurements

Measurements of hemodynamics in skeletal muscle have a large application in exercise science, as well as clinically [68]. Non-invasive measurements of BF and OC in skeletal muscle can be incredibly useful in the case of Peripheral Vascular Disease (PVD) which is caused by narrowing of blood vessels that carry blood to the limbs [3, 37, 60, 180]. The availability of hemodynamics that are representative of skeletal muscle can help in disease detection in patients with PVD risk factors along with monitoring disease progression to inform physicians on efficacy of treatments [180]. Limiting the effect of superficial adipose tissue can give a more accurate representation of skeletal muscle dynamics, thus having an impact on the use of NIRS on patients with PVD.

Non-invasive NIRS measurements on skeletal muscle must account for confounding contributions from adipose tissue hemodynamics [100] to measure signals more representative of skeletal muscle. Work presented in Chapter 3 proposed a method for discriminating absorption dynamics in superficial and deep tissue utilizing NIRS measurements with rich temporal and spatial information content without the use of a complex re-construction algorithm. Previous work has shown different sensitivities to different layers (in the z-direction) between data types (Intensity (I) and phase (ϕ)) and source-detector arrangements (Single-Distance (SD) and DS) [92] with the premise of this work to utilize this rich information space. Simulated data from a two-layer medium with different baseline optical properties (the reduced scattering coefficient (μ_s') and absorption coefficient (μ_a)) and absorption coefficient change ($\Delta\mu_a$) in the two layers were compared to experimental data to identify the best matching case. Trends in the data types presented in Chapter 3 differed depending on the specific optical properties chosen, which allows for discrimination and is the basis for the proposed method. This approach is an alternative method to those directly analyzed with a two-layer model.

The use of a two-layer model to directly analyze experimental data has been applied to both skeletal muscle [103, 107, 111] and brain measurements [29, 119, 120]. The study

by Ohmae *et al* (2014) [103] utilized TD-NIRS to develop correction curves generated from using the ratio between partial optical path-length ($\langle \ell \rangle$) in the muscle and total optical path-length ($\langle L \rangle$), while Re *et al* (2016) [107] utilized a fitting procedure and a two-layer medium. Both of these methods used TD-NIRS, which directly measures the $\langle L \rangle$ of a medium. While the methods utilized here for FD-NIRS uses the absolute effective μ_a and μ_s' within the medium to calculate $\langle L \rangle$. It was shown in Chapter 2 Figure 3.7 that utilization of an $\langle L \rangle$ calculated with either the effective homogeneous μ_a and μ_s' or with two-layer μ_a and μ_s' affects the measured $\Delta\mu_a$, as well as the relationship between the data types. This result highlighted the importance of utilizing the same method of calculating $\langle L \rangle$ in simulated and experimental data. It also brings into question previously reported measurements on skeletal muscle that have used an assumed a wavelength and source-detector distance independent Differential Path-length Factor (DPF) [20, 35, 72] taken from the literature. Characterization of the effect using an assumed DPF on the OC and BF has not been done and should be systematically studied as it is commonly used in literature.

Moving forward, the methodology utilized in Chapter 3 can be built upon in two different ways. The first method focuses on the idea of using an expanded data space and the specific relationship between the data types (I and ϕ) and different source-detector arrangements (SD and DS) for the comparison between experimental and simulated data. One possible way to implement this methodology is to minimize the difference between experimental and simulated data for each data type and source-detector arrangement while allowing the two-layer properties (μ_a and μ_s') and $\Delta\mu_a$ in the two layers to vary and converge on one optimal set. The matched properties can then be used to estimate the experimental $\Delta\mu_a$ in the two layers to calculate BF and OC in muscle and adipose tissue.

The second method is a full-fledged two-layer tissue model that focuses on the accurate recovery of μ_a and μ_s' in the two layers calculated by fitting to the two-layer complex Reflectance ($\widetilde{R}$) described in subsection 2.1.2. This method would allow for the calculation of the two-layer $\langle L \rangle$ for both simulation and experimental results over using an assumed

or effective homogeneous $\langle L \rangle$ as done in Chapter 3. Knowledge of the two-layer μ_a and μ_s' can then be used to generate a two-layer matrix of sensitivity to an absorption change ($\boldsymbol{\mathcal{S}}$) with these representative properties. This $\boldsymbol{\mathcal{S}}$ that can then utilized for two voxel image reconstruction to recover the top and bottom layer $\Delta\mu_a$ changes. As in the first method, the reconstructed $\Delta\mu_a$ can be used to calculate BF and OC in muscle and adipose tissue. Implementing both or one of the previously mentioned directions requires developing a new optical probe with more optical sources and detectors than the one utilized in Chapter 3. This work begins with the design of an optical probe with 4 DS/Self-Calibrating (SC) sets with SD ranging from 10 mm to 35 mm. Methodology number two requires a minimum of 2 DS sets to recover the 4 unknowns. The 4 DS sets were chosen as it is the maximum that can be achieved with the current instrumentation and having more available data can potentially improve the robustness of the fit for absolute optical properties.

7.3.1 Influence of Optical Probe Pressure

Placement of the optical probe on tissue is critical as the contact pressure on the tissue affects measured changes [129]. The contact pressure between the optical probe and the tissue is vital for NIRS measurements on skeletal muscle, especially in the case of a Venous Occlusion (VO). An experiment was performed to demonstrate the effect of probe pressure on the measured NIRS signal during a VO and Arterial Occlusion (AO) (Figure 7.1). The protocol for data presented in Figure 7.1 consisted of 3 different scenarios: the probe secured with loose pressure, the probe secured with medium pressure, and the probe secured tightly. Looking at Figure 7.1(a), it can be seen that increasing the probe tightness decreases the magnitude of the measured change, and when the probe is tight, there is no change from the occlusion. The working hypothesis is that a higher pressure causes tissue squeezing, thus preventing blood accumulation. As, in theory, blood does not accumulate during an AO this effect should be limited, and is seen in Figure 7.1(b). The effect is seen in the recovery after the occlusion, where a tight probe has a delayed response which could be due to increase

difficulty for blood accumulation.

To the best of our knowledge, no previous publications have evaluated the impact of optical probe pressure during a VO. Results presented in Figure 7.1(a) show the importance of optical probe pressure and the effect on measured BF values should be studied in detail. BF is typically measured as the slope of the Total hemoglobin and myoglobin concentration change (ΔT) for the first 1 to 2 cardiac cycles after the onset of the occlusion (described in subsection 1.4.1). A series of NIRS measurements taken during a protocol including a VO on different subjects showed a delay in the onset of change due to the VO. This delay was originally thought to be due to contact pressure but the initial study performed did not indicate that contact pressure was the cause. No publication utilizing a VO has specifically discussed the delay in the increase in ΔT after the onset of the VO and a limited number of publications present the time traces of ΔT. One publication that did present the time trace of ΔT during a VO (Casavola *et al* (2000) [56] Figure 3) showed a slight delay between the onset of the pneumatic cuff and ΔT increase due to the occlusion but was not discussed in the article. It is still unclear if this delay has been seen in previously reported VO studies and what the cause of this delay is.

Future work should focus on understanding the effect of contact pressure on measured BF and the cause of a delay in the increase of ΔT after the onset of the occlusion. If there is an effect, caution should be taken in comparing measured values to those reported in the literature. Optimizing contact pressure to minimize the effect on measured hemodynamics should be done via systematic studies utilizing pressure sensors embedded in the optical probe. Studies should be performed utilizing a VO and increasing the contact pressure between the optical probe and tissue. The outcome of this study should be an optimal range of probe pressure that should be consistently utilized. An optical probe with pressure sensors also allows for measurement of the pressure over the course of the VO. As a VO causes an increase in the Blood Volume (BV) after the first few seconds which are indicative of BF, evaluating when the increase in BV beings could help guide the section in time to fit for the

calculation of BF.

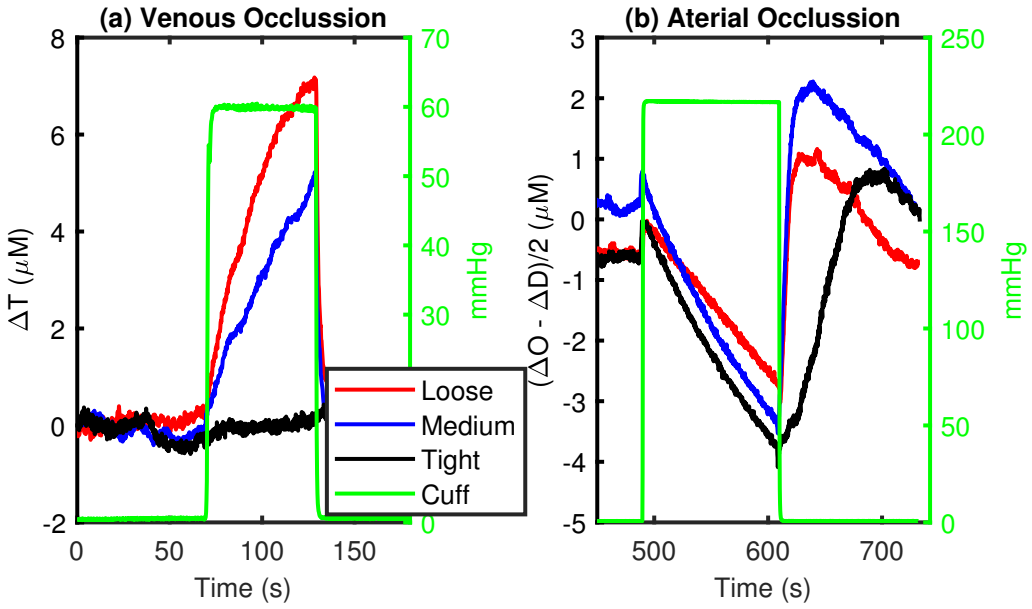

Figure 7.1: Example time trace of (a) the Total hemoglobin and myoglobin concentration change (ΔT) measured with Dual-Slope Intensity (DSI) during a Venous Occlusion (VO) and (b) the difference of the Oxy hemoglobin and myoglobin concentration change (ΔO) and the Deoxy hemoglobin and myoglobin concentration change (ΔD) during an Arterial Occlusion (AO) for three different levels of contact pressure between the optical probe and tissue. In both panels, the time trace in red the measured signal when the probe was placed with loose pressure, the trace in blue is the measured signal when the probe was placed at an average pressure, and black is the measured signal when the probe was placed at a tight pressure. In all cases, the DSI configuration with source-detector distances of 25 mm and 35 mm was utilized to obtain ΔO and ΔD. Hb refers to hemoglobin and Mb refers to myoglobin.

Funding Acknowledgments

Research presented here was supported by National Institutes of Health (NIH) grants R01-NS095334 and R01-EB029414 and the Air Force Office of Scientific Research (AFOSR) Grant FA9550-18-1-0465. The presented NeuroCritical Care Unit (NCCU) study was supported by the Neuroscience and Pain Research Unit at Pfizer Inc. and by the NIH Grant No. R21-EB020347.

References

[1]R. Sharma and S. Sharma, "Physiology, Blood Volume", in *StatPearls* (StatPearls Publishing, Treasure Island (FL), 2023).

[2]J. Shu and G. Santulli, "Update on peripheral artery disease: Epidemiology and evidence-based facts", Atherosclerosis **275**, 379–381 (2018).

[3]A. W. Aday and K. Matsushita, "Epidemiology of Peripheral Artery Disease and Polyvascular Disease", Circulation Research **128**, 1818–1832 (2021).

[4]A. S. Khaku and P. Tadi, "Cerebrovascular Disease", in *StatPearls* (StatPearls Publishing, Treasure Island (FL), 2023).

[5]E. Park, J. D. Bell, and A. J. Baker, "Traumatic brain injury: Can the consequences be stopped?", CMAJ **178**, 1163–1170 (2008).

[6]T. Funane, H. Atsumori, T. Katura, A. N. Obata, H. Sato, Y. Tanikawa, E. Okada, and M. Kiguchi, "Quantitative evaluation of deep and shallow tissue layers' contribution to fNIRS signal using multi-distance optodes and independent component analysis", NeuroImage, Celebrating 20 Years of Functional Near Infrared Spectroscopy (fNIRS) **85**, 150–165 (2014).

[7]P. M. Bloomfield, H. Green, and N. Gant, "Cerebral haemodynamics during simulated driving: Changes in workload are detectable with functional near infrared spectroscopy", PLoS ONE **16**, e0248533 (2021).

[8]A. T. Eggebrecht, S. L. Ferradal, A. Robichaux-Viehoever, M. S. Hassanpour, H. Dehghani, A. Z. Snyder, T. Hershey, and J. P. Culver, "Mapping distributed brain function and networks with diffuse optical tomography", Nature Photonics **8**, 448–454 (2014).

[9]L. Gagnon, M. A. Yücel, M. Dehaes, R. J. Cooper, K. L. Perdue, J. Selb, T. J. Huppert, R. D. Hoge, and D. A. Boas, "Quantification of the cortical contribution to the NIRS signal over the motor cortex using concurrent NIRS-fMRI measurements", NeuroImage **59**, 3933–3940 (2012).

[10]D. K. Joseph, T. J. Huppert, M. A. Franceschini, and D. A. Boas, "Diffuse optical tomography system to image brain activation with improved spatial resolution and validation with functional magnetic resonance imaging", Applied Optics **45**, 8142–8151 (2006).

[11]T. Sato, M. Ito, T. Suto, M. Kameyama, M. Suda, Y. Yamagishi, A. Ohshima, T. Uehara, M. Fukuda, and M. Mikuni, "Time courses of brain activation and their implications for function: A multichannel near-infrared spectroscopy study during finger tapping", Neuroscience Research **58**, 297–304 (2007).

[12]A. T. Eggebrecht, B. R. White, S. L. Ferradal, C. Chen, Y. Zhan, A. Z. Snyder, H. Dehghani, and J. P. Culver, "A quantitative spatial comparison of high-density diffuse optical tomography and fMRI cortical mapping", NeuroImage **61**, 1120–1128 (2012).

[13]G. Blaney, C. Fernandez, A. Sassaroli, and S. Fantini, "Dual-slope imaging of cerebral hemodynamics with frequency-domain near-infrared spectroscopy", Neurophotonics **10**, 013508 (2023).

[14]M. Reinhard, M. Roth, B. Guschlbauer, A. Harloff, J. Timmer, M. Czosnyka, and A. Hetzel, "Dynamic Cerebral Autoregulation in Acute Ischemic Stroke Assessed From Spontaneous Blood Pressure Fluctuations", Stroke **36**, 1684–1689 (2005).

[15]D. Phillip, H. Schytz, H. Iversen, J. Selb, D. Boas, and M. Ashina, "Spontaneous Low Frequency Oscillations in Acute Ischemic Stroke – A Near Infrared Spectroscopy (NIRS) Study", Journal of Neurology & Neurophysiology **5**, 10.4172/2155-9562.1000241 (2014).

[16]M. W.-D. Müller, M. Österreich, A. Müller, and J. Lygeros, "Assessment of the Brain's Macro- and Micro-Circulatory Blood Flow Responses to CO2 via Transfer Function Analysis", Frontiers in Physiology **7**, 162 (2016).

[17]A. V. Andersen, S. A. Simonsen, H. W. Schytz, and H. K. Iversen, "Assessing low-frequency oscillations in cerebrovascular diseases and related conditions with near-infrared spectroscopy: a plausible method for evaluating cerebral autoregulation?", Neurophotonics **5**, 030901 (2018).

[18]M. Reinhard, F. K. Schumacher, S. Rutsch, M. Oeinck, J. Timmer, I. Mader, B. Schelter, C. Weiller, and C. P. Kaller, "Spatial mapping of dynamic cerebral autoregulation by multichannel near-infrared spectroscopy in high-grade carotid artery disease", Journal of Biomedical Optics **19**, 97005 (2014).

[19]T. Pham, C. Fernandez, G. Blaney, K. Tgavalekos, A. Sassaroli, X. Cai, S. Bibu, J. Kornbluth, and S. Fantini, "Noninvasive Optical Measurements of Dynamic Cerebral Autoregulation by Inducing Oscillatory Cerebral Hemodynamics", Frontiers in Neurology **12:745987**, 10.3389/fneur.2021.745987 (2021).

[20]M. C. van Beekvelt, M. S. Borghuis, B. G. van Engelen, R. A. Wevers, and W. N. Colier, "Adipose tissue thickness affects in vivo quantitative near-IR spectroscopy in human skeletal muscle", Clinical Science **101**, 21–28 (2001).

[21]K. Gurley, Y. Shang, and G. Yu, "Noninvasive optical quantification of absolute blood flow, blood oxygenation, and oxygen consumption rate in exercising skeletal muscle", Journal of Biomedical Optics **17**, 075010 (2012).

[22]R. A. De Blasi, M. Cope, C. Elwell, F. Safoue, and M. Ferrari, "Noninvasive measurement of human forearm oxygen consumption by near infrared spectroscopy", European Journal of Applied Physiology and Occupational Physiology **67**, 20–25 (1993).

[23]M. D. Spencer, J. M. Murias, H. P. Lamb, J. M. Kowalchuk, and D. H. Paterson, "Are the parameters of VO2, heart rate and muscle deoxygenation kinetics affected by serial moderate-intensity exercise transitions in a single day?", European Journal of Applied Physiology **111**, 591–600 (2011).

[24]M. C. P. Van Beekvelt, W. N. J. M. Colier, R. A. Wevers, and B. G. M. Van Engelen, "Performance of near-infrared spectroscopy in measuring local O2 consumption and blood flow in skeletal muscle", Journal of Applied Physiology **90**, 511–519 (2001).

[25]T. Sako, T. Hamaoka, H. Higuchi, Y. Kurosawa, and T. Katsumura, "Validity of NIR spectroscopy for quantitatively measuring muscle oxidative metabolic rate in exercise", Journal of Applied Physiology **90**, 338–344 (2001).

[26]V. Cettolo, M. Ferrari, V. Biasini, and V. Quaresima, "Vastus Lateralis O2 Desaturation in Response to Fast and Short Maximal Contraction", Medicine & Science in Sports & Exercise **39**, 1949 (2007).

[27]Q. Zhang, E. N. Brown, and G. E. Strangman, "Adaptive filtering for global interference cancellation and real-time recovery of evoked brain activity: a Monte Carlo simulation study", Journal of Biomedical Optics **12**, 044014 (2007).

[28]L. Gagnon, M. A. Yücel, D. A. Boas, and R. J. Cooper, "Further improvement in reducing superficial contamination in NIRS using double short separation measurements", NeuroImage **85 Pt 1**, 127–135 (2014).

[29]R. Saager and A. Berger, "Measurement of layer-like hemodynamic trends in scalp and cortex: implications for physiological baseline suppression in functional near-infrared spectroscopy", Journal of Biomedical Optics **13**, 034017 (2008).

[30]A. Sassaroli, G. Blaney, and S. Fantini, "Dual-slope method for enhanced depth sensitivity in diffuse optical spectroscopy", Journal of the Optical Society of America. A, Optics, Image Science, and Vision **36**, 1743–1761 (2019).

[31]G. Blaney, A. Sassaroli, T. Pham, C. Fernandez, and S. Fantini, "Phase dual-slopes in frequency-domain near-infrared spectroscopy for enhanced sensitivity to brain tissue: First applications to human subjects", Journal of Biophotonics **13**, e201960018 (2020).

[32]S. Fantini and A. Sassaroli, "Frequency-Domain Techniques for Cerebral and Functional Near-Infrared Spectroscopy", Frontiers in Neuroscience **14** (2020).

[33]P. Sawosz and A. Liebert, "Method to improve the depth sensitivity of diffuse reflectance measurements to absorption changes in optically turbid medium", Biomedical Optics Express **10**, 5031–5041 (2019).

[34]A. Torricelli, D. Contini, A. Pifferi, M. Caffini, R. Re, L. Zucchelli, and L. Spinelli, "Time domain functional NIRS imaging for human brain mapping", NeuroImage, Celebrating 20 Years of Functional Near Infrared Spectroscopy (fNIRS) **85**, 28–50 (2014).

[35]V. M. Niemeijer, J. P. Jansen, T. van Dijk, R. F. Spee, E. J. Meijer, H. M. C. Kemps, and P. F. F. Wijn, "The influence of adipose tissue on spatially resolved near-infrared spectroscopy derived skeletal muscle oxygenation: the extent of the problem", Physiological Measurement **38**, 539 (2017).

[36]D. J. Davies, M. Clancy, D. Lighter, G. M. Balanos, S. J. E. Lucas, H. Dehghani, Z. Su, M. Forcione, and A. Belli, "Frequency-domain vs continuous-wave near-infrared spectroscopy devices: a comparison of clinically viable monitors in controlled hypoxia", Journal of Clinical Monitoring and Computing **31**, 967–974 (2017).

[37]A. M. Malagoni, M. Felisatti, S. Mandini, F. Mascoli, R. Manfredini, N. Basaglia, P. Zamboni, and F. Manfredini, "Resting Muscle Oxygen Consumption by Near-Infrared Spectroscopy in Peripheral Arterial Disease: A Parameter to be Considered in a Clinical Setting?", Angiology **61**, 530–536 (2010).

[38]A. N. Sen, S. P. Gopinath, and C. S. Robertson, "Clinical application of near-infrared spectroscopy in patients with traumatic brain injury: a review of the progress of the field", Neurophotonics **3**, 031409 (2016).

[39]R. Thomas, S. S. Shin, and R. Balu, "Applications of near-infrared spectroscopy in neurocritical care", Neurophotonics **10**, 023522 (2023).

[40]M. A. Rahman, A. B. Siddik, T. K. Ghosh, F. Khanam, and M. Ahmad, "A Narrative Review on Clinical Applications of fNIRS", Journal of Digital Imaging **33**, 1167–1184 (2020).

[41]K. Khaksari, G. Blaney, A. Sassaroli, N. Krishnamurthy, T. Pham, and S. Fantini, "Depth dependence of coherent hemodynamics in the human head", Journal of Biomedical Optics **23**, 121615 (2018).

[42]K. Tgavalekos, T. Pham, N. Krishnamurthy, A. Sassaroli, and S. Fantini, "Frequency-resolved analysis of coherent oscillations of local cerebral blood volume, measured with near-infrared spectroscopy, and systemic arterial pressure in healthy human subjects", PLOS ONE **14**, e0211710 (2019).

[43]D. Hueber, S. Fantini, A. Cerussi, and B. Barbieri, "New optical probe designs for absolute (self-calibrating) NIR tissue hemoglobin measurements", in Optical Tomography and Spectroscopy of Tissue II, Vol. 3597 (1999), pp. 618–631.

[44]S. Fantini, G. Blaney, and A. Sassaroli, "Transformational change in the field of diffuse optics: From going bananas to going nuts", Journal of Innovative Optical Health Sciences **13**, 1930013 (2020).

[45]V. Quaresima and M. Ferrari, "Functional Near-Infrared Spectroscopy (fNIRS) for Assessing Cerebral Cortex Function During Human Behavior in Natural/Social Situations: A Concise Review", Organizational Research Methods **22**, 46–68 (2019).

[46]B. Hallacoglu, A. Sassaroli, S. Fantini, M. Wysocki, E. Guerrero-Berroa, M. S. Beeri, V. Haroutunian, M. Shaul, I. H. Rosenberg, and A. Troen, "Absolute measurement of cerebral optical coefficients, hemoglobin concentration and oxygen saturation in old and young adults with near-infrared spectroscopy", Journal of Biomedical Optics **17**, 081406 (2012).

[47]G. A. Perkins, A. T. Eggebrecht, and H. Dehghani, "Quantitative evaluation of frequency domain measurements in high density diffuse optical tomography", Journal of Biomedical Optics **26** (2021).

[48]M. A. Franceschini, S. Fantini, L. A. Paunescu, J. S. Maier, and E. Gratton, "Influence of a superficial layer in the quantitative spectroscopic study of strongly scattering media", Applied Optics **37**, 7447–7458 (1998).

[49]C. Mansouri, J.-P. L'Huillier, N. H. Kashou, and A. Humeau, "Depth sensitivity analysis of functional near-infrared spectroscopy measurement using three-dimensional Monte Carlo modelling-based magnetic resonance imaging", Lasers in Medical Science **25**, 431–438 (2010).

[50]G. Blaney, P. Curtsmith, A. Sassaroli, C. Fernandez, and S. Fantini, "Broadband absorption spectroscopy of heterogeneous biological tissue", Applied Optics **60**, 7552–7562 (2021).

[51]D. Lintzeri, N. Karimian, U. Blume-Peytavi, and J. Kottner, "Epidermal thickness in healthy humans: a systematic review and meta-analysis", Journal of the European Academy of Dermatology and Venereology **36**, 1191–1200 (2022).

[52]W. R. Frontera and J. Ochala, "Skeletal Muscle: A Brief Review of Structure and Function", Calcified Tissue International **96**, 183–195 (2015).

[53]R. J. Korthuis, *Skeletal Muscle Circulation*, Integrated Systems Physiology: From Molecule to Function to Disease (Morgan & Claypool Life Sciences, San Rafael (CA), 2011).

[54]S. Egginton, "Invited review: activity-induced angiogenesis", Pflügers Archiv - European Journal of Physiology **457**, 963–977 (2009).

[55]G. Liu, F. M. Gabhann, and A. S. Popel, "Effects of Fiber Type and Size on the Heterogeneity of Oxygen Distribution in Exercising Skeletal Muscle", PLOS ONE **7**, e44375 (2012).

[56]C. Casavola, L. A. Paunescu, S. Fantini, and E. Gratton, "Blood flow and oxygen consumption with near-infrared spectroscopy and venous occlusion: spatial maps and the effect of time and pressure of inflation", Journal of Biomedical Optics **5**, 269–276 (2000).

[57]S. W. Coppack, R. M. Fisher, G. F. Gibbons, S. M. Humphreys, M. J. McDonough, J. L. Potts, and K. N. Frayn, "Postprandial substrate deposition in human forearm and adipose tissues in vivo", Clinical Science **79**, 339–348 (1990).

[58]S. P. Mortensen and B. Saltin, "Regulation of the skeletal muscle blood flow in humans", Experimental Physiology **99**, 1552–1558 (2014).

[59]I. Sarelius and U. Pohl, "Control of muscle blood flow during exercise: local factors and integrative mechanisms", Acta Physiologica **199**, 349–365 (2010).

[60]L. A. Paunescu, C. Casavola, M.-A. Franceschini, S. Fantini, L. Winter, J. Kim, D. Wood, and E. Gratton, "Calf muscle blood flow and oxygen consumption measured with near-infrared spectroscopy during venous occlusion", in Optical Tomography and Spectroscopy of Tissue III, Vol. 3597 (July 1999), pp. 317–323.

[61]A. Parkin, P. A. Wiggins, P. J. Robinson, P. Vowden, R. C. Kester, and F. M. Ware, "Use of a gamma camera for measuring limb blood flow in peripheral vascular disease", The British Journal of Surgery **74**, 271–274 (1987).

[62]U. Wolf, M. Wolf, J. H. Choi, M. Levi, D. Choudhury, S. Hull, D. Coussirat, L. A. Paunescu, L. P. Safonova, A. Michalos, W. W. Mantulin, and E. Gratton, "Localized irregularities in hemoglobin flow and oxygenation in calf muscle in patients with peripheral vascular disease detected with near-infrared spectrophotometry", Journal of Vascular Surgery **37**, 1017–1026 (2003).

[63]D. Choudhury, B. Michener, P. Fennelly, and M. Levi, "Near-infrared spectroscopy in the evaluation of lower limb ischemia in hemodialysis patients", Journal for Vascular Ultrasound **23**, 21–23 (1999).

[64]R. Zelis, J. Longhurst, R. J. Capone, and D. T. Mason, "A comparison of regional blood flow and oxygen utilization during dynamic forearm exercise in normal subjects and patients with congestive heart failure", Circulation **50**, 137–143 (1974).

[65]T. Imaizumi, A. Takeshita, N. Nakamura, K. Sakai, Y. Hirooka, S. Suzuki, M. Yoshida, and M. Nakamura, "Effects of captopril on forearm oxygen consumption during dynamic handgrip exercise in patients with congestive heart failure", Japanese Heart Journal **31**, 817–828 (1990).

[66]C. M. Hearon Jr and F. A. Dinenno, "Regulation of skeletal muscle blood flow during exercise in ageing humans", The Journal of Physiology **594**, 2261–2273 (2016).

[67]J. O. Holloszy, K. K. McCully, and J. D. Posner, "The Application of Blood Flow Measurements to the Study of Aging Muscle", The Journals of Gerontology: Series A **50A**, 130–136 (1995).

[68]M. Ferrari, M. Muthalib, and V. Quaresima, "The use of near-infrared spectroscopy in understanding skeletal muscle physiology: recent developments", Philosophical Transactions of the Royal Society A: Mathematical, Physical and Engineering Sciences **369**, 4577–4590 (2011).

[69]M. L. Davis and T. J. Barstow, "Estimated contribution of hemoglobin and myoglobin to near infrared spectroscopy", Respiratory Physiology & Neurobiology **186**, 180–187 (2013).

[70]A. Seiyama, O. Hazeki, and M. Tamura, "Noninvasive Quantitative Analysis of Blood Oxygenation in Rat Skeletal Muscle", The Journal of Biochemistry **103**, 419–424 (1988).

[71]D. J. Marcinek, C. E. Amara, K. Matz, K. E. Conley, and K. A. Schenkman, "Wavelength Shift Analysis: A Simple Method to Determine the Contribution of Hemoglobin and Myoglobin to In Vivo Optical Spectra", Applied Spectroscopy **61**, 665–669 (2007).

[72]T. J. Cross and S. Sabapathy, "The impact of venous occlusion per se on forearm muscle blood flow: implications for the near-infrared spectroscopy venous occlusion technique", Clinical Physiology and Functional Imaging **37**, 293–298 (2017).

[73]T. S. Sigurdsson and L. Lindberg, "Indirect Calorimetry Overestimates Oxygen Consumption in Young Children: Caution is Advised Using Direct Fick Method as a Reference Method in Cardiac Output Comparison Studies", Pediatric Cardiology **41**, 149–154 (2020).

[74]O. J. Hartling, H. Kelbæk, T. Gjørup, B. Schibye, K. Klausen, and J. Trap-Jensen, "Forearm oxygen uptake during maximal forearm dynamic exercise", European Journal of Applied Physiology and Occupational Physiology **58**, 466–470 (1989).

[75]R. E. Wood and I. B. Stewart, "Can venous occlusion plethysmography be used to measure high rates of arterial inflow?", European Journal of Applied Physiology **108**, 239–245 (2010).

[76]S. E. Campbell, R. Adler, and C. M. Sofka, "Ultrasound of Muscle Abnormalities", Ultrasound Quarterly **21**, 87 (2005).

[77]G. Yu, T. F. Floyd, T. Durduran, C. Zhou, J. Wang, J. A. Detre, and A. G. Yodh, "Validation of diffuse correlation spectroscopy for muscle blood flow with concurrent arterial spin labeled perfusion MRI", Optics Express **15**, 1064–1075 (2007).

[78]M. J. Cipolla, "Control of Cerebral Blood Flow", in *The Cerebral Circulation* (Morgan & Claypool Life Sciences, 2009).

[79]S. Fantini, A. Sassaroli, K. T. Tgavalekos, and J. Kornbluth, "Cerebral blood flow and autoregulation: current measurement techniques and prospects for noninvasive optical methods", Neurophotonics **3**, 031411 (2016).

[80]P. Le Roux, "Invasive Neurological and Multimodality Monitoring in the NeuroICU", in *Textbook of Neurointensive Care*, edited by A. J. Layon, A. Gabrielli, and W. A. Friedman (Springer, London, 2013), pp. 127–145.

[81]L. T. Dunn, "Raised Intracranial Pressure", Journal of Neurology, Neurosurgery & Psychiatry **73**, i23–i27 (2002).

[82]D. DeMers and D. Wachs, "Physiology, Mean Arterial Pressure", in *StatPearls* (StatPearls Publishing, Treasure Island (FL), 2023).

[83]N. A. Lassen, "Normal average value of cerebral blood flow in younger adults is 50 ml/100 g/min", Journal of Cerebral Blood Flow and Metabolism: Official Journal of the International Society of Cerebral Blood Flow and Metabolism **5**, 347–349 (1985).

[84]S. L. Dawson, R. B. Panerai, and J. F. Potter, "Serial Changes in Static and Dynamic Cerebral Autoregulation after Acute Ischaemic Stroke", Cerebrovascular Diseases **16**, 69–75 (2003).

[85]R. Aaslid, K. F. Lindegaard, W. Sorteberg, and H. Nornes, "Cerebral autoregulation dynamics in humans", Stroke **20**, 45–52 (1989).

[86]T. Pham, K. Tgavalekos, A. Sassaroli, G. Blaney, and S. Fantini, "Quantitative measurements of cerebral blood flow with near-infrared spectroscopy", Biomedical Optics Express **10**, 2117–2134 (2019).

[87]A. B. Parthasarathy, K. P. Gannon, W. B. Baker, C. G. Favilla, R. Balu, S. E. Kasner, A. G. Yodh, J. A. Detre, and M. T. Mullen, "Dynamic autoregulation of cerebral blood flow measured non-invasively with fast diffuse correlation spectroscopy", Journal of Cerebral Blood Flow and Metabolism: Official Journal of the International Society of Cerebral Blood Flow and Metabolism **38**, 230–240 (2018).

[88]M. Reinhard, M. Roth, T. Müller, B. Guschlbauer, J. Timmer, M. Czosnyka, and A. Hetzel, "Effect of Carotid Endarterectomy or Stenting on Impairment of Dynamic Cerebral Autoregulation", Stroke **35**, 1381–1387 (2004).

[89]A. S. S. Meel-vandenAbeelen, A. H. E. A. vanBeek, C. H. Slump, R. B. Panerai, and J. A. H. R. Claassen, "Transfer function analysis for the assessment of cerebral autoregulation using spontaneous oscillations in blood pressure and cerebral blood flow", Medical Engineering & Physics, Special Issue on Cerebral Autoregulation: Measurement and Modelling **36**, 563–575 (2014).

[90]V. B. Semenyutin, G. A. Asaturyan, A. A. Nikiforova, V. A. Aliev, G. K. Panuntsev, V. B. Iblyaminov, A. V. Savello, and A. Patzak, "Predictive Value of Dynamic Cerebral Autoregulation Assessment in Surgical Management of Patients with High-Grade Carotid Artery Stenosis", Frontiers in Physiology **8** (2017).

[91]J. M. Kainerstorfer, A. Sassaroli, K. T. Tgavalekos, and S. Fantini, "Cerebral Autoregulation in the Microvasculature Measured with Near-Infrared Spectroscopy", Journal of Cerebral Blood Flow & Metabolism **35**, 959–966 (2015).

[92]T. Pham, G. Blaney, A. Sassaroli, C. Fernandez, and S. Fantini, "Sensitivity of frequency-domain optical measurements to brain hemodynamics: simulations and human study of cerebral blood flow during hypercapnia", Biomedical Optics Express **12**, 766–789 (2021).

[93]K. T. Tgavalekos, A. Sassaroli, X. Cai, J. Kornbluth, and S. Fantini, "Coherent hemodynamics spectroscopy: initial applications in the neurocritical care unit", in Optical Tomography and Spectroscopy of Tissue XII, Vol. 10059 (Feb. 2017), pp. 138–143.

[94]A. Sassaroli, X. Zang, K. T. Tgavalekos, and S. Fantini, "Induced and spontaneous hemodynamic oscillations in cerebral and extracerebral tissue for coherent hemodynamics spectroscopy", in Optical Tomography and Spectroscopy of Tissue XII, Vol. 10059 (Feb. 2017), pp. 138–145.

[95]S. Fantini, "Dynamic model for the tissue concentration and oxygen saturation of hemoglobin in relation to blood volume, flow velocity, and oxygen consumption: Implications for functional neuroimaging and coherent hemodynamics spectroscopy (CHS)", NeuroImage, Celebrating 20 Years of Functional Near Infrared Spectroscopy (fNIRS) **85**, 202–221 (2014).

[96]I. J. Bigio and S. Fantini, *Quantitative Biomedical Optics: Theory, Methods, and Applications* (Cambridge: Cambridge University Press, Jan. 2016).

[97]A. Liemert and A. Kienle, "Light diffusion in a turbid cylinder. II. Layered case", Optics Express **18**, 9266–9279 (2010).

[98]G. Blaney, R. Donaldson, S. Mushtak, H. Nguyen, L. Vignale, C. Fernandez, T. Pham, A. Sassaroli, and S. Fantini, "Dual-Slope Diffuse Reflectance Instrument for Calibration-Free Broadband Spectroscopy", Applied sciences **11**, 1757 (2021).

[99]G. Blaney, A. Sassaroli, and S. Fantini, "Design of a source-detector array for dual-slope diffuse optical imaging", The Review of Scientific Instruments **91**, 093702 (2020).

[100]T. J. Barstow, "Understanding near infrared spectroscopy and its application to skeletal muscle research", Journal of Applied Physiology **126**, 1360–1376 (2019).

[101]F. Harel, N. Olamaei, Q. Ngo, J. Dupuis, and P. Khairy, "Arterial flow measurements during reactive hyperemia using NIRS", Physiological Measurement **29**, 1033 (2008).

[102]N. Olamaei, J. Dupuis, Q. Ngo, V. Finnerty, T.-T. V. Thang, S. Authier, P. Khairy, and F. Harel, "Characterization and reproducibility of forearm arterial flow during reactive hyperemia", Physiological Measurement **31**, 763 (2010).

[103]E. Ohmae, S. Nishio, M. Oda, H. Suzuki, T. Suzuki, K. Ohashi, S. Koga, Y. Yamashita, and H. Watanabe, "Sensitivity correction for the influence of the fat layer on muscle oxygenation and estimation of fat thickness by time-resolved spectroscopy", Journal of Biomedical Optics **19**, 067005 (2014).

[104]V. Quaresima, M. Ferrari, M. A. Franceschini, M. L. Hoimes, and S. Fantini, "Spatial distribution of vastus lateralis blood flow and oxyhemoglobin saturation measured at the end of isometric quadriceps contraction by multichannel near-infrared spectroscopy", Journal of Biomedical Optics **9**, 413–420 (2004).

[105]L. F. Ferreira, D. M. Hueber, and T. J. Barstow, "Effects of assuming constant optical scattering on measurements of muscle oxygenation by near-infrared spectroscopy during exercise", Journal of Applied Physiology **102**, 358–367 (2007).

[106]J. C. Craig, R. M. Broxterman, S. L. Wilcox, C. Chen, and T. J. Barstow, "Effect of adipose tissue thickness, muscle site, and sex on near-infrared spectroscopy derived total-[hemoglobin + myoglobin]", Journal of Applied Physiology (2017).

[107]R. Re, D. Contini, L. Zucchelli, A. Torricelli, and L. Spinelli, "Effect of a thin superficial layer on the estimate of hemodynamic changes in a two-layer medium by time domain NIRS", Biomedical Optics Express **7**, 264–278 (2016).

[108]G. Blaney, A. Sassaroli, T. Pham, C. Fernandez, and S. Fantini, "Towards functional dual-slope imaging: methods to design, evaluate, and construct a source-detector array", in Optical Tomography and Spectroscopy of Tissue XIV, Vol. 11639 (Mar. 2021), pp. 122–127.

[109]S. Jones, S. T. Chiesa, N. Chaturvedi, and A. D. Hughes, "Recent developments in near-infrared spectroscopy (NIRS) for the assessment of local skeletal muscle microvascular function and capacity to utilise oxygen", Artery Research **16**, 25–33 (2016).

[110]L. M. K. Chin, J. M. Kowalchuk, T. J. Barstow, N. Kondo, T. Amano, T. Shiojiri, and S. Koga, "The relationship between muscle deoxygenation and activation in different muscles of the quadriceps during cycle ramp exercise", Journal of Applied Physiology **111**, 1259–1265 (2011).

[111]G. Blaney, M. Bottoni, A. Sassaroli, C. Fernandez, and S. Fantini, "Broadband diffuse optical spectroscopy of two-layered scattering media containing oxyhemoglobin, deoxyhemoglobin, water, and lipids", Journal of innovative optical health sciences **15**, 2250020 (2022).

[112]V. Perekatova, A. Kostyuk, M. Kirillin, E. Sergeeva, D. Kurakina, O. Shemagina, A. Orlova, A. Khilov, and I. Turchin, "VIS-NIR Diffuse Reflectance Spectroscopy System with Self-Calibrating Fiber-Optic Probe: Study of Perturbation Resistance", Diagnostics **13**, 457 (2023).

[113]M.-A. Franceschini, S. Fantini, A. E. Cerussi, B. B. Barbieri, B. Chance, and E. Gratton, "Quantitative spectroscopic determination of hemoglobin concentration and saturation in a turbid medium: analysis of the effect of water absorption", Journal of Biomedical Optics **2**, 147–153 (1997).

[114]I. Pirovano, S. Porcelli, R. Re, L. Spinelli, D. Contini, M. Marzorati, and A. Torricelli, "Effect of adipose tissue thickness and tissue optical properties on the differential path-length factor estimation for NIRS studies on human skeletal muscle", Biomedical Optics Express **12**, 571–587 (2021).

[115]U. Wolf, M. Wolf, J. H. Choi, L. A. Paunescu, A. Michalos, and E. Gratton, "Regional differences of hemodynamics and oxygenation in the human calf muscle detected with near-infrared spectrophotometry", Journal of vascular and interventional radiology: JVIR **18**, 1094–1101 (2007).

[116]S. L. Jacques, "Optical properties of biological tissues: a review", Physics in Medicine & Biology **58**, R37 (2013).

[117]A. N. Bashkatov, E. A. Genina, and V. V. Tuchin, "Optical properties of skin, subcutaneous, and muscle tissues: a review", Journal of Innovative Optical Health Sciences **04**, 9–38 (2011).

[118]M. Niwayama, L. Lin, J. Shao, N. Kudo, and K. Yamamoto, "Quantitative measurement of muscle hemoglobin oxygenation using near-infrared spectroscopy with correction for the influence of a subcutaneous fat layer", Review of Scientific Instruments **71**, 4571–4575 (2000).

[119]B. Hallacoglu, A. Sassaroli, and S. Fantini, "Optical Characterization of Two-Layered Turbid Media for Non-Invasive, Absolute Oximetry in Cerebral and Extracerebral Tissue", PLOS ONE **8**, e64095 (2013).

[120]L. Gagnon, C. Gauthier, R. D. Hoge, F. Lesage, J. Selb, and D. A. Boas, "Double-layer estimation of intra- and extracerebral hemoglobin concentration with a time-resolved system", Journal of Biomedical Optics **13**, 054019 (2008).

[121]J. D. Veesa and H. Dehghani, "Signal regression in frequency-domain diffuse optical tomography to remove superficial signal contamination", Neurophotonics **8**, 015013 (2021).

[122]G. Blaney, A. Sassaroli, C. Fernandez, M. Bottoni, and S. Fantini, "Functional brain mapping with dual-slope frequency-domain near-infrared spectroscopy", in Neural Imaging and Sensing 2022, Vol. 11946 (Mar. 2022), p. 1194602.

[123]M. Reinhard, E. Wehrle-Wieland, D. Grabiak, M. Roth, B. Guschlbauer, J. Timmer, C. Weiller, and A. Hetzel, "Oscillatory cerebral hemodynamics—the macro- vs. microvascular level", Journal of the Neurological Sciences **250**, 103–109 (2006).

[124]S. Prahl, *Tabulated Molar Extinction Coefficient for Hemoglobin in Water*, https://omlc.org/spectra/hemoglobin/summary.html, 1998.

[125]G. Blaney, A. Sassaroli, and S. Fantini, "Dual-slope imaging in highly scattering media with frequency-domain near-infrared spectroscopy", Optics Letters **45**, 4464 (2020).

[126]C. Fernandez, G. Blaney, A. Sassaroli, T. Das, and S. Fantini, "Mapping of coherent cerebral hemodynamics with dual-slope imaging", in Optical Tomography and Spectroscopy of Tissue XV, edited by S. Fantini and P. Taroni (Mar. 2023), p. 33.

[127]G. Blaney, A. Sassaroli, T. Pham, N. Krishnamurthy, and S. Fantini, "Multi-Distance Frequency-Domain Optical Measurements of Coherent Cerebral Hemodynamics", Photonics **6**, 83 (2019).

[128]S. N. Krieger, M. N. Streicher, R. Trampel, and R. Turner, "Cerebral blood volume changes during brain activation", Journal of Cerebral Blood Flow & Metabolism **32**, 1618–1631 (2012).

[129]R. C. Mesquita, S. S. Schenkel, D. L. Minkoff, X. Lu, C. G. Favilla, P. M. Vora, D. R. Busch, M. Chandra, J. H. Greenberg, J. A. Detre, and A. G. Yodh, "Influence of probe pressure on the diffuse correlation spectroscopy blood flow signal: extra-cerebral contributions", Biomedical Optics Express **4**, 978–994 (2013).

[130]S. Thulung, K. Ranabhat, S. Bishokarma, and D. N. Gongal, "Morphometric Measurement of Cranial Vault Thickness: A Tertiary Hospital Based Study", JNMA: Journal of the Nepal Medical Association **57**, 29–32 (2019).

[131]M. Ş. Ekşi, M. Güdük, and M. I. Usseli, "Frontal Bone is Thicker in Women and Frontal Sinus is Larger in Men: A Morphometric Analysis", The Journal of Craniofacial Surgery **32**, 1683–1684 (2021).

[132]M. Calisan, M. F. Talu, D. Y. Pimenov, and K. Giasin, "Skull Thickness Calculation Using Thermal Analysis and Finite Elements", Applied Sciences **11**, 10483 (2021).

[133]D. A. Boas, A. M. Dale, and M. A. Franceschini, "Diffuse optical imaging of brain activation: approaches to optimizing image sensitivity, resolution, and accuracy", NeuroImage **23 Suppl 1**, S275–288 (2004).

[134]K.-S. Hong and M. A. Yaqub, "Application of functional near-infrared spectroscopy in the healthcare industry: A review", Journal of Innovative Optical Health Sciences **12**, 1930012 (2019).

[135]J. E. Mayhew, S. Askew, Y. Zheng, J. Porrill, G. W. Westby, P. Redgrave, D. M. Rector, and R. M. Harper, "Cerebral vasomotion: a 0.1-Hz oscillation in reflected light imaging of neural activity", NeuroImage **4**, 183–193 (1996).

[136]T. Huppert, R. Hoge, S. Diamond, M. Franceschini, and D. Boas, "A temporal comparison of BOLD, ASL, and NIRS hemodynamic responses to motor stimuli in adult humans", NeuroImage **29**, 368–382 (2006).

[137]H. Obrig, M. Neufang, R. Wenzel, M. Kohl, J. Steinbrink, K. Einhäupl, and A. Villringer, "Spontaneous Low Frequency Oscillations of Cerebral Hemodynamics and Metabolism in Human Adults", NeuroImage **12**, 623–639 (2000).

[138]I. Tachtsidis, M. Tisdall, D. T. Delpy, M. Smith, and C. E. Elwell, "Measurement of Cerebral Tissue Oxygenation in Young Healthy Volunteers During Acetazolamide Provocation: A Transcranial Doppler and Near-Infrared Spectroscopy Investigation", in Oxygen Transport to Tissue XXIX, edited by K. A. Kang, D. K. Harrison, and D. F. Bruley, Advances In Experimental Medicine And Biology (2008), pp. 389–396.

[139]R. Zhang, J. H. Zuckerman, and B. D. Levine, "Spontaneous fluctuations in cerebral blood flow: insights from extended-duration recordings in humans", American Journal of Physiology-Heart and Circulatory Physiology **278**, H1848–H1855 (2000).

[140]C. Julien, "The enigma of Mayer waves: Facts and models", Cardiovascular Research **70**, 12–21 (2006).

[141]A. Sassaroli, M. Pierro, P. R. Bergethon, and S. Fantini, "Low-Frequency Spontaneous Oscillations of Cerebral Hemodynamics Investigated With Near-Infrared Spectroscopy: A Review", IEEE Journal of Selected Topics in Quantum Electronics **18**, 1478–1492 (2012).

[142]R. B. Panerai, P. Brassard, J. S. Burma, P. Castro, J. A. Claassen, J. J. vanLieshout, J. Liu, S. J. Lucas, J. S. Minhas, G. D. Mitsis, R. C. Nogueira, S. Ogoh, S. J. Payne, C. A. Rickards, A. D. Robertson, G. D. Rodrigues, J. D. Smirl, and D. M. Simpson, "Transfer function analysis of dynamic cerebral autoregulation: A CARNet white paper 2022 update", Journal of Cerebral Blood Flow & Metabolism **43**, 3–25 (2023).

[143]J. A. Claassen, A. S. Meel-van den Abeelen, D. M. Simpson, and R. B. Panerai, "Transfer function analysis of dynamic cerebral autoregulation: A white paper from the International Cerebral Autoregulation Research Network", Journal of Cerebral Blood Flow & Metabolism **36**, 665–680 (2016).

[144]C. E. Elwell, R. Springett, E. Hillman, and D. T. Delpy, "Oscillations in cerebral haemodynamics. Implications for functional activation studies", Advances in Experimental Medicine and Biology **471**, 57–65 (1999).

[145]T. B. Kuo, C.-M. Chern, C. C. Yang, H.-Y. Hsu, W.-J. Wong, W.-Y. Sheng, and H.-H. Hu, "Mechanisms Underlying Phase Lag between Systemic Arterial Blood Pressure and Cerebral Blood Flow Velocity", Cerebrovascular Diseases **16**, 402–409 (2003).

[146]E. Kirilina, N. Yu, A. Jelzow, H. Wabnitz, A. Jacobs, and I. Tachtsidis, "Identifying and quantifying main components of physiological noise in functional near infrared spectroscopy on the prefrontal cortex", Frontiers in Human Nueroscience **7** (2013).

[147]C. Fernandez, T. Das, G. Blaney, Z. Haga, T. McWilliams, J. Mertens, A. Sassaroli, and S. Fantini, "Coherent Spontaneous Hemodynamics in the Human Brain", IEEE Open Journal of Engineering in Medicine and Biology **4**, 102–108 (2023).

[148]T. McWilliams, N. Ward, B. Mehler, and B. Reimer, "Assessing Driving Simulator Validity: A Comparison of Multi-Modal Smartphone Interactions across Simulated and Field Environments", Transportation Research Record **2672**, 164–171 (2018).

[149]C. Jeleazcov, L. Krajinovic, T. Münster, T. Birkholz, R. Fried, J. Schüttler, and J. Fechner, "Precision and accuracy of a new device (CNAP™) for continuous non-invasive arterial pressure monitoring: assessment during general anaesthesia", BJA: British Journal of Anaesthesia **105**, 264–272 (2010).

[150]G. Blaney, A. Sassaroli, and S. Fantini, "Algorithm for Determination of Thresholds of Significant Coherence in Time-Frequency Analysis", Biomedical Signal Processing and Control **56**, 101704 (2020).

[151]A. Sassaroli, K. Tgavalekos, and S. Fantini, "The meaning of "coherent" and its quantification in coherent hemodynamics spectroscopy", Journal of Innovative Optical Health Sciences **11**, 1850036 (2018).

[152]T. Katura, N. Tanaka, A. Obata, H. Sato, and A. Maki, "Quantitative evaluation of interrelations between spontaneous low-frequency oscillations in cerebral hemodynamics and systemic cardiovascular dynamics", NeuroImage **31**, 1592–1600 (2006).

[153]M. L. Pierro, A. Sassaroli, P. R. Bergethon, B. L. Ehrenberg, and S. Fantini, "Phase-amplitude investigation of spontaneous low-frequency oscillations of cerebral hemodynamics with near-infrared spectroscopy: A sleep study in human subjects", NeuroImage **63**, 1571–1584 (2012).

[154]G. Xu, M. Zhang, Y. Wang, Z. Liu, C. Huo, Z. Li, and M. Huo, "Functional connectivity analysis of distracted drivers based on the wavelet phase coherence of functional near-infrared spectroscopy signals", PLOS ONE **12**, e0188329 (2017).

[155]C. Zweifel, G. Castellani, M. Czosnyka, E. Carrera, K. M. Brady, P. J. Kirkpatrick, J. D. Pickard, and P. Smielewski, "Continuous Assessment of Cerebral Autoregulation With Near-Infrared Spectroscopy in Adults After Subarachnoid Hemorrhage", Stroke **41**, 1963–1968 (2010).

[156]L. Rangel-Castilla, J. Gasco, H. J. W. Nauta, D. O. Okonkwo, and C. S. Robertson, "Cerebral pressure autoregulation in traumatic brain injury", Neurosurgical Focus **25**, E7 (2008).

[157]J. Donnelly, K. P. Budohoski, P. Smielewski, and M. Czosnyka, "Regulation of the cerebral circulation: bedside assessment and clinical implications", Critical Care **20**, 129 (2016).

[158]K. P. Budohoski, M. Czosnyka, P. Smielewski, M. Kasprowicz, A. Helmy, D. Bulters, J. D. Pickard, and P. J. Kirkpatrick, "Impairment of Cerebral Autoregulation Predicts Delayed Cerebral Ischemia After Subarachnoid Hemorrhage", Stroke **43**, 3230–3237 (2012).

[159]K. Nakagawa, J. M. Serrador, S. L. LaRose, and F. A. Sorond, "Dynamic cerebral autoregulation after intracerebral hemorrhage: A case-control study", BMC Neurology **11**, 108 (2011).

[160]R. B. Panerai, V. Hudson, L. Fan, P. Mahony, P. M. Yeoman, T. Hope, and D. H. Evans, "Assessment of dynamic cerebral autoregulation based on spontaneous fluctuations in arterial blood pressure and intracranial pressure", Physiological Measurement **23**, 59–72 (2001).

[161]R. R. Diehl, D. Linden, D. Lücke, and P. Berlit, "Phase relationship between cerebral blood flow velocity and blood pressure. A clinical test of autoregulation", Stroke **26**, 1801–1804 (1995).

[162]M. M. Placek, P. Wachel, D. R. Iskander, P. Smielewski, A. Uryga, A. Mielczarek, T. A. Szczepański, and M. Kasprowicz, "Applying time-frequency analysis to assess cerebral autoregulation during hypercapnia", PLOS ONE **12**, e0181851 (2017).

[163]E. Sorrentino, K. P. Budohoski, M. Kasprowicz, P. Smielewski, B. Matta, J. D. Pickard, and M. Czosnyka, "Critical thresholds for transcranial Doppler indices of cerebral autoregulation in traumatic brain injury", Neurocritical Care **14**, 188–193 (2011).

[164]R. V. Immink, G. A. van Montfrans, J. Stam, J. M. Karemaker, M. Diamant, and J. J. van Lieshout, "Dynamic cerebral autoregulation in acute lacunar and middle cerebral artery territory ischemic stroke", Stroke **36**, 2595–2600 (2005).

[165]P. J. D. Andrews and G. Citerio, "Intracranial pressure", Intensive Care Medicine **30**, 1730–1733 (2004).

[166]W. M. Armstead, "Cerebral Blood Flow Autoregulation and Dysautoregulation", Anesthesiology clinics **34**, 465–477 (2016).

[167]J. A. H. R. Claassen, B. D. Levine, and R. Zhang, "Dynamic cerebral autoregulation during repeated squat-stand maneuvers", Journal of Applied Physiology **106**, 153–160 (2009).

[168]R. L. Hughson, M. R. Edwards, D. D. O'Leary, and J. K. Shoemaker, "Critical Analysis of Cerebrovascular Autoregulation During Repeated Head-Up Tilt", Stroke **32**, 2403–2408 (2001).

[169]A. A. Birch, G. Neil-Dwyer, and A. J. Murrills, "The repeatability of cerebral autoregulation assessment using sinusoidal lower body negative pressure", Physiological Measurement **23**, 73 (2001).

[170]A. B. Rowley, S. J. Payne, I. Tachtsidis, M. J. Ebden, J. P. Whiteley, D. J. Gavaghan, L. Tarassenko, M. Smith, C. E. Elwell, and D. T. Delpy, "Synchronization between arterial blood pressure and cerebral oxyhaemoglobin concentration investigated by wavelet cross-correlation", Physiological Measurement **28**, 161 (2006).

[171]F. Tian, T. Tarumi, H. Liu, R. Zhang, and L. Chalak, "Wavelet coherence analysis of dynamic cerebral autoregulation in neonatal hypoxic–ischemic encephalopathy", NeuroImage : Clinical **11**, 124–132 (2016).

[172]P. Lanka, A. Segala, A. Farina, S. K. V. Sekar, E. Nisoli, A. Valerio, P. Taroni, R. Cubeddu, and A. Pifferi, "Non-invasive investigation of adipose tissue by time domain diffuse optical spectroscopy", Biomedical Optics Express **11**, 2779–2793 (2020).

[173]D. A. Boas, C. E. Elwell, M. Ferrari, and G. Taga, "Twenty years of functional near-infrared spectroscopy: introduction for the special issue", NeuroImage, Celebrating 20 Years of Functional Near Infrared Spectroscopy (fNIRS) **85**, 1–5 (2014).

[174]Y. Moriguchi and K. Hiraki, "Prefrontal cortex and executive function in young children: a review of NIRS studies", Frontiers in Human Neuroscience **7** (2013).

[175]S. Chakravarti, S. Srivastava, and A. J. C. Mittnacht, "Near Infrared Spectroscopy (NIRS) in Children", Seminars in Cardiothoracic and Vascular Anesthesia **12**, 70–79 (2008).

[176]Y. Yu, K. Zhang, L. Zhang, H. Zong, L. Meng, and R. Han, "Cerebral near-infrared spectroscopy (NIRS) for perioperative monitoring of brain oxygenation in children and adults", Cochrane Database of Systematic Reviews, `10.1002/14651858.CD010947.pub2` (2018).

[177]M. Soltanlou, M. A. Sitnikova, H.-C. Nuerk, and T. Dresler, "Applications of Functional Near-Infrared Spectroscopy (fNIRS) in Studying Cognitive Development: The Case of Mathematics and Language", Frontiers in Psychology **9** (2018).

[178]P. Stamatios, "Can Preschoolers Learn Computational Thinking and Coding Skills with ScratchJr? A Systematic Literature Review", International Journal of Educational Reform, 10567879221076077 (2022).

[179]L. E. de Ruiter and M. U. Bers, "The Coding Stages Assessment: development and validation of an instrument for assessing young children's proficiency in the ScratchJr programming language", Computer Science Education **32**, 388–417 (2022).

[180]S. Joseph, B. Munshi, R. Agarini, R. C. H. Kwok, D. J. Green, and S. Jansen, "Near infrared spectroscopy in peripheral artery disease and the diabetic foot: A systematic review", Diabetes/Metabolism Research and Reviews **38**, e3571 (2022).